Hydrogen embrittlement of twinning-induced plasticity (TWIP) steel in a viewpoint of practical issues

アバス, モハマディ

https://doi.org/10.15017/2534451

出版情報：Kyushu University, 2019, 博士（工学）, 課程博士
バージョン：
権利関係：

Hydrogen embrittlement of twinning-induced plasticity (TWIP) steel in a viewpoint of practical issues

A dissertation submitted to the faculty of engineering

Graduate school, Kyushu University, Japan

For the degree of doctor of philosophy

Presented by

ABBAS MOHAMMADI

July 2019

Index

List of Abbreviations

HEDE	-	Hydrogen-enhanced decohesion
HELP	-	Hydrogen-enhanced localized plasticity
TEM	-	Transmission electron microscopy
SFE	-	Stacking-fault energy
AIDE	-	Adsorption-induced dislocation emission
HESIV	-	Hydrogen-enhanced strain-induced vacancies
TWIP	-	Twinning-induced plasticity
DP	-	Dual phase
TRIP	-	Transformation-induced plasticity
HDF	-	Hydrogen-delayed fracture
EBSD	-	Electron backscatter diffraction
RD	-	Reference direction
IPF	-	Inverse pole figure
IQ	-	Image quality
ND	-	Normal direction
TD	-	Transverse direction
SEM	-	Scanning electron microscope
1DH	-	One drill hole
3DH	-	Three drill hole

Nomenclature

K	-	Stress intensity factor
R-curve	-	Resistance curve
G	-	Energy release rate
L	-	Initial ligament length
l	-	Local net ligament length
F	-	Applied load
t	-	Thickness
CTOD	-	Crack tip opening displacement
D_H	-	Hydrogen diffusion
σ_f^*	-	Local fracture stress
D_H^*	-	Local hydrogen diffusion

CHAPTER 1. General introduction

1.1 Research background

1.1.1 Hydrogen in steels

Hydrogen embrittlement or degradation of mechanical properties by hydrogen is a latent problem for structural materials. Toughness drops and unpredictable failure may occur. High strength steels are even more susceptible to hydrogen embrittlement [1]. This confirms the importance of a detailed study of the behavior of hydrogen in steels to predict the potential fracture.

Hydrogen embrittlement was first documented by Johnson [2], who reported that the hydrogen causes a reduction in ductility and fracture stress of iron. Since then, it has been shown that the phenomenon is not restricted to steels but occurs in many materials such Ni [3], Al [4], Ti [5], Zr [6], Ta [7], Nb [8], V [9], W [10] and Mo [11] although the individual mechanisms may not be identical.

1.1.2 Theoretical approaches

Although intense scientific effort has been devoted to understanding different aspects of hydrogen embrittlement, there is still no consensus on the mechanisms causing the behavior, nor any general theory that can describe the many effects of hydrogen on metal flow and fracture. We know that hydrogen can interact with (i) dislocations to change the overall plastic flow behavior, (ii) crack tips to change the local deformation (enhancing or suppressing cleavage relative to dislocation emission), (iii) grain boundaries to enhance intergranular failure, (iv) interfaces to enhance interfacial decohesion, and/or (v) other defects such as precipitates, vacancies, and solutes. Any combination of these phenomena may occur in a given material, but how these process/es actually lead to hydrogen embrittlement is unclear. The experimental studies not only provide some insight into the

problem of the hydrogen embrittlement but also give motivations and evidences for new theories explaining them.

Numerous mechanisms have been proposed to account for the hydrogen embrittlement. Hereby, we discuss some of the most likely mechanisms of hydrogen embrittlement in steel, which is a non-hydride forming material, outlined below.

1.1.2.1 Hydrogen-Enhanced Decohesion (HEDE)

The decohesion theory, proposed by Troiano [12] and developed by Oriani et al. [13, 14], is based on the idea that hydrogen accumulated within the lattice reduces the interatomic cohesive forces. The reduction of interatomic cohesive forces results from the increased interatomic distance. Oriani and Josephic [13] postulated that the highly elastically-stressed region at the crack front lowered sufficiently the chemical potential of dissolved hydrogen, which attained a concentration several orders of magnitude larger than in normal lattice sites and lowered the cohesive energy. Cracks propagated when the local crack tip tensile stress exceeded the atomic cohesive energy. This fracture initiated at a distance ahead of the crack tip where the tensile stress was a maximum.

The HEDE mechanism is supported by the facts that (i) large concentration of hydrogen should accumulate at crack tips where there are high stresses, and (ii) atomistic simulations reveal that hydrogen can reduce atomic cohesion [15]. The HEDE mechanism considers that there is a critical concentration of hydrogen which causes brittle fracture. HEDE could also cause intergranular fracture, in which a high concentration of hydrogen accumulates at grain boundaries and thus reaches the critical concentration for brittle fracture.

1.1.2.2 Hydrogen-Enhanced Localized Plasticity (HELP)

This mechanism, first formulated by Beachem [16], proposes that hydrogen enhances dislocation motion so that the localized plastic deformation is large enough to cause subcritical crack growth with macroscopically brittle characteristics. The presence of hydrogen in solid solution increases dislocation mobility and creates localized high deformation regions. The increase of dislocation mobility is attributed to the reduction in the interactions between dislocations or between dislocations and other obstacles. The dislocations thus move closer to each other and to obstacles, forming more compact pile-ups and less ductile zones. These dislocation pile-up zones are surrounded by high deformation regions, and the applied stress is concentrated on these zones. Failure occurs when the tensile stress in these zones is higher than the ultimate tensile strength of the material. This fracture process leads to cracking by microvoid coalescence along preferred crystallographic glide planes [17, 18]. Robertson [19] conducted deformation studies in a hydrogen environment in situ observation by means of transmission electron microscopy (TEM) with an environmental cell to elucidate the mechanisms of hydrogen embrittlement. The HELP mechanism was supported by observations revealing increased number of dislocations in a pile-up, and decreased stacking-fault energy (SFE), as well as the increased crack propagation rate caused by solute hydrogen.

1.1.2.3 Adsorption-induced dislocation emission (AIDE)

The AIDE mechanism was developed by Lynch [20, 21]. This mechanism involves both dislocation nucleation and subsequent movement away from the crack tip. The nucleation of dislocations is facilitated by the adsorbed hydrogen at the surface of the crack tip. During the nucleation, the adsorbed hydrogen weakens the interatomic bond, facilitating the simultaneous formation of a dislocation core and a surface step by the breaking and

reforming of interatomic bonds. Once the nucleation is accomplished, dislocations can readily move away from the crack tip under the applied stress, contributing to the crack growth.

In the AIDE mechanism, in addition to dislocation emission, crack growth involves the nucleation and growth of microvoids at the crack tip. The nucleation and growth of voids occurs because the stresses for dislocation emission are so high that some dislocation activity occurs ahead of the crack. Although the void formation can contribute to the crack growth, the crack growth primarily occurs by the dislocation emission from crack tips.

1.1.2.4 Hydrogen-Enhanced Strain-Induced Vacancies (HESIV)

The HESIV mechanism proposes the primary function of hydrogen in degradation to elevate the strain-induced nucleation and accumulation of vacancies, thus promoting easy formation and linking of microvoids for the fracture process [22]. High dislocation movement can create high density of strain-induced vacancies [23], suggesting vacancy accumulation as a mechanism of the microvoid formation observed at the front region of the crack tip in iron [24]. Furthermore, the hydrogen affects during the plastic deformation on the elevation of vacancies deformation [25].

1.1.3 Effect of strain rate on hydrogen embrittlement

The embrittlement mechanisms discussed above require the presence of sufficient levels of hydrogen at specific locations. Thus, the embrittlement is limited by the capacity of the hydrogen atoms to move through the metallic lattice by interstitial diffusion. As assisted by dislocation transport, diffusion of hydrogen can be accelerated [26]. Toribio [27] has examined the embrittlement process in steels at different strain rates. He observed that the deleterious effect of hydrogen generally decreased with increasing strain rate. Same results

can be observed in Koyama et al. research [28] on high strength twinning induced plasticity (TWIP) steel. Hydrogen embrittlement is substantially more pronounced at low strain rate as shown in Fig. 1.1.

1.1.4 Hydrogen embrittlement in TWIP steels

1.1.4.1 TWIP steels

High-manganese TWIP steels are currently promising candidates for applications in the automotive industry due to their exceptional combination of strength and elongation, as shown in Fig. 1.2 [29, 30]. The metallurgical development of the relevant Fe-Mn-C system began with the work of Hadfield [31]. The austenite remains stable during deformation and some of the plastic deformation occurs by twinning, which is said to enhance elongation.

The high ductility of TWIP steel is obtained as a result of its high work hardening rate [32]. However, the associated mechanism is still a matter of debate. Some authors attribute the hardening to dynamic strain aging mechanism for those alloys containing an appreciable amount of solute C, typically more than 0.5 wt% [33, 34]. The interaction between C-Mn bonds and mobile dislocations may cause the strain aging and lead to serrated flow curves [35]. Mechanical twinning can also improve the strain hardening. This is so called the TWIP is considered to results from a dynamical Hall-Petch effect [36-39]. It is argued that the mechanical twins that contain a huge density of sessile dislocations resulting from the mechanism of twin nucleation and growth [39] play the role of planar obstacles for the dislocation glide.

1.1.4.2 Effect of stacking fault energy (SFE) on deformation mechanism

During austenite plastic deformation, the following three mechanisms could occur: martensite transformation [40], twinning [41] and dislocation glide [42]. The SFE is a critical

factor that determines which transformation occurs. The SFE depends on the temperature and the chemical composition of the TWIP steel, in particular concentrations of manganese, Al and silicon. The effect of stacking fault energy on the deformation mechanism [43] is that twinning occurs when the SFE is within the range of 18-50 mJ/m^2. If the SFE is lower, the martensite transformation is more likely. If the SFE is higher, dislocation glide is the only possible mechanism[44] However, different ranges have been reported for the value of stacking fault energy for mechanical twinning, such as 18–45 mJ/m^2 [45], 20–40 mJ/m^2 [46] and 12–35 mJ/m^2 [37]. These differences result from the difficulty in experimentally determining the value of stacking fault energy [46].

It has been reported that hydrogen under cathodic charging conditions during austenite plastic deformation reduces their stacking fault energy [47, 48]. The following mechanism can be promoted by this effect: ε-martensitic transformation [49, 50] and deformation twinning [51, 52].

1.1.4.3 Hydrogen embrittlement susceptibility

TWIP steel, as a class of fcc austenite high-Mn steels, show higher resistance to hydrogen embrittlement when compare to the low carbon steel, martensitic steels, dual phase (DP) steels and transformation-induced plasticity (TRIP) steels due to the severe suppression dislocation/hydrogen interactions. The research results are not consistent with regard to hydrogen-delayed fracture (HDF). There are reports that the TWIP steel is prone to HDF after forming, attributed to hydrogen embrittlement [53, 54]. There are also reports stating that some grades of TWIP steels are immune to HDF [53, 55]. Investigations concerning mechanical degradation after introducing hydrogen are also not consistent. Some researchers have observed negligible mechanical degradation using tensile tests with hydrogen pre-charged specimens [55-58]. Similarly, So et al.[55] found there was little difference of the

mechanical properties of Fe–18Mn–1.5Al–0.6C TWIP steel charged with different hydrogen contents and those without hydrogen charging. Similarly, Ronevich et al. [57, 58] studied the influence on TWIP steels of different hydrogen contents introduced by cathodic charging the steels at the same current density for different durations before the tensile tests. The tensile properties, including yield strength, ultimate tensile strength, strain to failure and strain hardening behavior, of the TWIP steels without hydrogen, and with different hydrogen contents, were essentially the same. It was concluded that the TWIP steels in their studies were not affected by hydrogen, attributed to the low hydrogen diffusion coefficient in austenite, introducing basically no hydrogen into the bulk steel, and leading to the steels unaffected by hydrogen. Suh [59] critically reviewed hydrogen induced fracture in TWIP steels and concluded that because of the low diffusion coefficient of hydrogen in austenite, there was limited penetration of hydrogen into the bulk of the steels, resulting in the little change of the mechanical properties of TWIP steels.

In contrast, Koyama et al. [60-62] found a significant decrease of mechanical properties, caused by the presence of hydrogen, of the Fe–18Mn–0.6C and Fe–18Mn–1.2C TWIP steels. Tensile tests measured the change of mechanical properties. The specimens were cathodically charged in a 3% NaCl aqueous solution containing 3 g/L NH4SCN at current density of 10 A/m^2 during the tensile tests to introduce hydrogen. Hydrogen charged Fe–18Mn–0.6C TWIP steels revealed [61] values of average total elongation and ultimate tensile strength of 32% and 1010 MPa, respectively, compared with 70% and 1200 MPa without hydrogen. For Fe–18Mn–1.2C TWIP steel [62], there was a similar reduction of elongation and ultimate tensile strength by hydrogen, which was about a 20% reduction of ultimate tensile strength, and about 40% reduced elongation from about 80% to 42%.

1.1.4.4 Effects of Al on hydrogen uptake and embrittlement behavior

Al influences the SFE, which is a relevant parameter for determining the deformation mechanism in austenitic steels, and the deformation mechanism in TWIP steels, resulting in a change of resistance of TWIP steels to hydrogen embrittlement. Al additions to such alloys are known to enhance the resistance to static failure; it is speculated that Al promotes more homogeneous deformation via its influence on the increase of the stacking fault energy [63, 64]. Alloying with Al has been shown to lead to a reduction of residual stress in Fe–18Mn–0.6C wt%, and this could contribute to an increased resistance to hydrogen embrittlement [65]. The formation of an alumina layer on the surface of the steel during hydrogen charging of a Fe–19Mn–0.6C–2Al wt% steel may hinder hydrogen absorption on the surface [54].

Ryu et al. [66] investigated the effect of Al on hydrogen-induced embrittlement in TWIP steels. The addition of Al reduced the loss in both elongation and ultimate tensile strength. The fracture surface had regions near the surface of brittle features that were both intergranular and transgranular, and those in the center were ductile with dimples. The depth of the brittle zones increased with the increasing hydrogen charging current density, but was reduced by the addition of Al, consistent with the results that the mechanical properties of TWIP steel with Al were less sensitive to hydrogen. This effect of Al was attributed to the fact that Al could increase the stacking fault energy of austenite, reducing the possibility of mechanical twinning and suppressing the transformation of ε-martensite during deformation, both of which would contribute to the hydrogen trapping and promote transgranular fracture, and thus lead to a lower susceptibility of the steel to hydrogen embrittlement.

Consistent results showing that the hydrogen embrittlement susceptibility decreased with increasing Al content was also provided by Koyama et al. [67]. Moreover, strengthening by strain aging can improve the resistance to hydrogen embrittlement. Al addition contributed to the suppression of static strain aging under loading, and the increased Al content and strain

rate led to the suppression of dynamic strain aging during pre-deformation. Since dynamic and static strain aging influenced the hydrogen embrittlement, the increased Al content could affect the susceptibility to hydrogen embrittlement. Figures 1.3 and 1.4 show the high hydrogen embrittlement resistance by presence of Al in Fe-22Mn-0.6C [68] .

1.1.4.5 Effects of alloying elements Mn, Si in high-Mn steels

Most recent works on hydrogen embrittlement in high-Mn austenitic steels have been carried out for typical TWIP steel compositions such as Fe-Mn-C or Fe-Mn-Al-C systems. However, it is also interesting how other alloying elements affect hydrogen embrittlement susceptibility in high-Mn austenitic steels. In fact, in addition to the Al effect, the influencing effects of Mn [69] , Si [70], Cu [71], and P [71] in solid solution states have been investigated systematically also.

The Mn effect was examined by using binary Fe-Mn austenitic alloys [69]. As is well known, Mn increases the stability of the austenite phase, which decreases hydrogen embrittlement susceptibility since both, the trend towards twin and towards martensite formation are reduced. However, when austenite is fully stable, excess Mn assists in the intergranular cracking probably because of a reduction in the cohesive energy of grain boundaries [72, 73].

Fig. 1.5 shows the effect of Si on the hydrogen embrittlement susceptibility in an Fe-18Mn-0.6C TWIP steel. The addition of 1.6%Si increases the hydrogen embrittlement susceptibility as revealed when comparing Fig. 1.5a and b [70]. Further addition of Si results in a considerable amount of deformation-induced ε-martensite, which causes distinct hydrogen-induced deterioration of the elongation to fracture pertaining to the occurrence of brittle fracture as shown in Fig. 1.5c.

1.1.4.6 Effects of grain refinement

Grain size is an important parameter influencing hydrogen embrittlement susceptibility of steels. Grain refinement helps in reducing susceptibility to hydrogen embrittlement in two possible ways. Grain boundaries can act as permanent traps for hydrogen [41]. Therefore, by increasing the grain boundary area per unit volume it is feasible to trap more hydrogen. This will help in decreasing hydrogen mobility in the bulk matrix, especially the movement of hydrogen towards potential crack initiation sites. As a result, the resistance of the material to hydrogen embrittlement will improve drastically.

A promising way to increase yield strength while maintaining austenite stability is grain refinement [74-77]. In general, hydrogen embrittlement susceptibility increases with increasing strength [78-80]. By contrast, the grain refinement methodology does not deteriorate resistance to hydrogen-related failure [80-85]. Thus, the effects of grain size on the deformation mechanisms and work hardening rates in TWIP steels have been intensively investigated [75, 86-88]. In fact, grain refinement enables the simultaneous improvement of the yield strength and the resistance to hydrogen-related failure. The reasons for the reduction in hydrogen embrittlement susceptibility are related to the local hydrogen content [83-85, 89, 90], local stress concentration [61, 67], and deformation twinning behavior [61, 67, 91]. In terms of the hydrogen content, grain-refined TWIP steel also shows a decrease in strength with increasing hydrogen content, but the loss of strength is significantly less than that of coarse-grained TWIP steels [83]. This can be attributed to the fact that the decreasing grain size reduces the local hydrogen content at grain boundaries where hydrogen-assisted cracking occurs preferentially. According to previous studies [75, 92], the local stress concentration at grain boundaries in a fine-grained specimen is much lower than that in a coarse-grained one due to the decrease in the number of piled-up dislocations. This in turn reduces the accumulated local hydrogen content at the grain boundaries of the fine-grained

specimen, which is a possible rationale for the improvement in the resistance to hydrogen embrittlement upon grain refinement [82, 83]. Certainly, the decrease in the local stress concentration at grain boundaries contributes to the decrease in hydrogen embrittlement susceptibility even without a reduction in the local hydrogen content. In addition, deformation twinning is suppressed by grain refinement [41, 93]. The interaction between twins and grain boundaries can lead to the growth of twins, e.g. [8]. As these act as crack initiation sites and propagation paths, the suppression of deformation twinning should also decrease the hydrogen susceptibility of TWIP steels [61, 83].

However, the tensile strength increases with decreasing grain size and the grain refinement also suppresses hydrogen-induced degradation of the tensile mechanical properties. Fig. 1.6 shows an example of the grain size dependence of the tensile behavior of specimens with and without hydrogen charging [94]. In summary, the positive effect of grain refinement can be explained in terms of three factors. First, the grain refinement suppresses deformation twinning [82, 95, 96] . Second, it reduces the diffusible hydrogen content per grain boundary area [75, 83]. Third, the frequency of local stress concentration spots at grain boundaries decreases with decreasing grain size, which may also affect the local hydrogen content at grain boundaries [75].

1.1.4.7 Bimodal-grained TWIP steel

In general, the ultra-fine grained steels with homogenized grain size distribution exhibit high strength and desired but not high ductility at room temperature. The latter is attributed to the lack of optimized work hardening behavior during plastic deformation [97, 98]. The development of bimodal grain size distribution, which simultaneously consists of coarse and fine grains mixture, was introduced as a key concept to improve the strength and formability of the ferrous and non-ferrous alloys [99, 100]. Bimodal grain structures, owing to the high

work hardening capacity of coarser grains along with the strengthening ability of finer ones, exhibit superior combination of strength and ductility [101]. For example, pure copper with a bimodal grain structure and fcc structure like TWIP steels has a 400 MPa tensile strength with over 60% elongation, which is a much higher ductility/strength balance than that of homogeneously grain-refined copper [98]. The bimodal grain structure enhances the work hardening capability because of plastic strain inhomogeneity that causes a high accumulation rate of dislocations [98]. The enhanced work hardening delays the onset of necking, thus increasing the uniform elongation [98, 102-105]. In the same context, a fully austenitic TWIP steel with a bimodal grain structure has been reported to feature a superior ductility/strength balance. For instance, a TWIP steel with the bimodal grain structure demonstrated 600 MPa 0.2% proof strength, 800 MPa tensile strength, and 35% elastic engineering strain [106].

Despite this structure has an exceptional mechanical condition, however, so far, the role of bimodal grain distribution on hydrogen embrittlement of TWIP steel is not investigated in previous research.

1.1.5 Fracture behavior

1.1.5.1 Ductile and brittle failure

Most metals at room temperature fail in a ductile fashion, preceded by extensive plastic deformation and associated energy dissipation (toughness), in contrast with brittle fracture (Fig. 1.7), which occurs without noticeable permanent deformations. Notch blunting, necking and cup-cone failure under tension are also characteristic phenomena of ductile fracture [17]. Crack propagation occurs in a stable manner, i.e. with crack growth resistance during crack propagation, and extensive plastic deformation [107]. A ductile behavior in failure is preferred over a brittle response in most engineering applications. For example, in

civil or naval engineering, ductile failure can prevent the catastrophic failure of a bridge or a ship. In metal forming processes, e.g. deep drawing, ductile materials may undergo very large deformation without breaking.

Microscopically, ductile failure is caused by the initiation, growth and coalescence of voids. Initiation occurs at inclusions [108] and void growth is promoted by positive hydrostatic stress states [109, 110]. During ductile failure two general modes of void growth can be identified [110]. The first mode (depicted schematically in Fig. 1.8a) is driven by hydrostatic tensile stress, due to which the nucleated microvoids expand more or less spherically [111]. This may lead to a significant increase of the void volume fraction. When the void spacing becomes critical individual microvoids will coalesce and form larger voids or microcracks [112, 113].

The second mode (Fig. 1.8b) develops in regions of intense shearing. This shearing causes the nucleated microvoids and the matrix material around them to extend in the direction of the major principal strain [114], whereas perpendicular to this direction, i.e. in the direction of the minor principal strain, hardly any elongation is present. Consequently, no significant increase of the void volume fraction can be observed, in contrast with the previously discussed spherical void growth mechanism. The local strength reduction by the presence of the elongated microvoids may lead to the development of shear bands, i.e. localized zones of intense plastic shearing. Finally, in this case coalescence is triggered by instabilities in the ligaments between neighboring voids within the shear bands rather than due to impingement by growing microvoids [113]. Therefore, coalescence of voids can be due to the a ‘void sheeting mechanism’ within the ligaments joining adjacent voids or by internal necking of these ligaments as explained above (Fig. 1.8). Crack advancement occurs by the continuous joining of voids to the main crack.

The two main factors that lead to the ductile failure are plastic strain and hydrostatic stress. Depending on the type of loading, their relative importance varies. Under tension loading, both plastic strain and hydrostatic stress play an important role. In the case of shear loading, failure is caused by plastic straining and the relative volume occupied by voids remains limited.

However, void nucleation, growth and coalescence play a prominent role as an initiation and propagation mechanism hydrogen-assisted cracking. Koyama et al. [115] represented that the grain boundary cracking in high Mn steel resulted from micro-void formation and coalescence along the grain boundaries. The slip localization enhanced by hydrogen uptake [116] induces micro-void formations and ductile failure along the grain boundaries by association HELP mechanism [117, 118]. In addition, quasi-cleavage fracture surface occurred through the coalescence of microvoids/cracks[119, 120] has been reported to arise from twin boundary cracking in hydrogen-assisted cracking of TWIP steels [66, 121].

1.1.5.2. Intrinsic versus extrinsic toughening

Traditionally, toughness has been thought of as the ability of a material to dissipate deformation energy without propagation of a crack [122]. In fracture mechanics terms, however, the initiation and subsequent extension of a crack can be considered, specifically in terms of the ‘‘crack-driving force’’ (e.g., K, G, or J) opposed by the resistance of the microstructure.

Toughness can be enhanced by increasing the microstructural resistance [123, 124], such as by changing the nature, distribution and/or interface properties of second-phase particles to suppress damage in the form of microcracking or microvoid formation ahead of the crack tip; this is termed intrinsic toughening and is the principal means by which ductile materials, e.g., metallic materials, derive their toughness. However, this approach is largely ineffective

with brittle materials such as ceramics [125], which invariably must rely on extrinsic toughening. Extrinsic toughening involves microstructural mechanisms that act primarily behind the crack tip to effectively reduce the crack-driving force actually experienced at the crack tip; this is termed crack-tip shielding and can occur by such mechanisms as crack bridging, in situ phase transformations and plastic wake [126, 127]. Indeed, fracture is the result of a mutual competition of intrinsic (damage) mechanisms ahead of the crack tip that promote cracking and extrinsic (shielding) mechanisms mainly behind the tip trying to impede it (Fig. 1.9) [128]. Intrinsic toughening mechanisms are an inherent property of the material, and thus are active irrespective of crack size and geometry; they affect primarily the initiation but also the growth of a crack. In metallic materials, intrinsic damage mechanisms typically involve processes which create microcracks or voids, e.g., by dislocation pile-ups or interface decohesion, in the highly stressed region ahead of the tip, leading to classical failure by cleavage, intergranular cracking or microvoid coalescence [126]. Extrinsic mechanisms, conversely, act in the crack wake and are thus dependent on crack size (and to some degree specimen geometry). Consequently, they result in crack-size dependent fracture behavior, a principal manifestation of which is resistance-curve (R-curve) toughness behavior where the crack driving force to sustain cracking increases with crack extension. Where extrinsic shielding mechanisms are active, rising *R*-curve toughness behavior and small-crack effects are to be expected. Extrinsic mechanisms affect only the crack growth toughness; they have little effect on crack initiation.

1.1.5.3 R-curve

Generally, the fracture behavior relates to the micro-mechanism of fracture, and is usually described as being ductile or brittle. Brittle fracture behavior results in the development of rapid and unstable crack extension (1.10a). Macroscopically, a test specimen demonstrating

this mode of fracture has a unique and well-defined point of crack initiation corresponds to the certain critical fracture toughness, corresponding to a sudden drop in load, characterizing fracture failure, and provides a measurement of a point value of fracture toughness. Due to crack extension by micro ductile void growth and coalescence which tends to absorb more energy, ductile fracture behavior results in slow and stable crack extension (Fig.10.b). This macro mode of fracture has a continuous process of ductile tearing rather than a point fracture, and requires an R-curve to be measured for characterizing ductile fracture. The R-curve behavior can cause some uncertainty as to where to specify the fracture point since crack extension can occur under increasing load conditions due to material strain hardening. The entire R-curve can be used to describe the ductile fracture. However, many methods that use fracture toughness for structural integrity assessment require a single-point value of toughness. A typical point value of ductile fracture toughness is usually defined near the onset of stable crack tearing and deduced from the R-curve near the transition from initial crack blunting to crack tearing which is usually characterized by a distinct change in slope of the R-curve. This result is referred to as fracture initiation toughness.

While hydrogen has a considerable effect of crack initiation and propagation, subsequently has a strong effect on R-curve behavior. Many studies were carried out experimentally and numerically to explain the effect of hydrogen on the resistance of the materials [129-133]. Results indicated that hydrogen has a considerable effect of fracture resistance due to the acceleration of crack growth process and a reduction of fracture toughness and the resistance curves decreased as the hydrogen content was increased. Figure 1.11 shows the hydrogen effect on the initiation toughness and the tearing resistance of the Zircaloy-4 alloy. The fracture resistance is reduced by increasing hydrogen content [134].

1.2 Purpose of this study

Generally, practical problems in structures are related to two parts of material microstructure and structure geometry. The motivation of this research is based on these two practical issues in the presence of hydrogen to understand the mechanisms of crack initiation and propagation and related factors of these mechanisms.

Practical consideration for light-weight manufacturing requires the material with high strength and reasonable ductility. The exceptional combination of these two mechanical parameters provides high quality and low cost for industries particularly in automotive and aerospace industries. Furthermore, there is an interest in numerous application where hydrogen embrittlement may occur, such as use of hydrogen gas as an energy carrier for both transportation and energy sectors. However, material microstructures play an important role to resist the hydrogen embrittlement. On the other hand, most structure members always contain the geometric discontinuities, such as notch or crack-like defects from the manufacturing and machining as well as servicing processes. The main difficulty in designing against fracture in materials particularly in high-strength steels is that the presence of notches or cracks can modify the local stresses at the crack or notch tip. This stress concentration makes hydrogen more aggressive as a hydrogen embrittlement agent.

Regarding as mentioned concepts, I study on the practical material which has been received attention from the automotive industry, namely: TWIP steel to underlie the mechanisms of hydrogen-assisted crack initiation and propagation in the applicable geometries such as notch and crack-like defects under electrochemical hydrogen charging. One of the important issue that should be considered in the crack propagation is hydrogen kinetic. This mechanism is also studied to the viewpoints of local and global strain rates by introducing different precrack lengths and various applied strain rates, respectively.

1.3 Thesis outline

The thesis consists of six chapters. All chapters are arranged in order to achieve the main theme and objectives of the research work as explained briefly as a purpose of this study. The dissertation is organized as follow:

Chapter 1 describes a general introduction of this work. A newly-developed high-strength steel called TWIP steel shows an exceptional combination of strength and elongation. Unlike general high-strength steels such as low carbon steels, marteistic steels and dual-phase steels, TWIP steels present high resistance to hydrogen embrittlement. Therefore, what has launched TWIP steel into the limelight of practical steel in a design of light-weight structures particularly automotive industries and hydrogen-based applications is a focus on the extraordinary balance between strength and elongation and also high resistance against hydrogen embrittlement.

Chapter 2 illustrates the mechanisms of hydrogen-assisted crack initiation and propagation in the one type of interesting microstructure of TWIP steel, namely, bimodal-grained TWIP steel. In case of smooth specimen, the crack initiation and propagation mechanisms of equi-axed TWIP steel have been studied under hydrogen environment, but the practical one contains a bit peculiar microstructure, i.e., bimodal-grained has not been fully understood. However, no systematic work has been reported on the effects of the bimodal grain size distribution on hydrogen embrittlement in TWIP steel. Hydrogen is introduced to the smooth specimen by electrochemical charging under slow strain rate tensile test. Results indicated that crack initiation sites showed transgranular and intergranulr cracking. In addition, the observed fracture surface exhibited quasi-cleavage fracture features combination with ductile delamination cracking. In this chapter, we confirmed that the bimodal grain size distribution of TWIP steel plays a major role in hydrogen-assisted cracking and the evolution of delamination-related damage.

Chapter 3 illustrates the behavior of the hydrogen-assisted crack growth of pre-strained twinning-induced plasticity (TWIP) steel with an artificial defect (micro-drill hole/s) as an artificial crack initiation site. Hydrogen was introduced to the specimens by electrochemical hydrogen charging during the slow strain rate tensile test. The observed fracture surface exhibited quasi-cleavage fracture features. The quasi-cleavage crack propagation was caused by repetition of crack initiation near a crack tip and subsequent coalescence. The crack initiation near the crack tip occurs after crack-tip plastic deformation. An effect of the pre-strain facilitates the plasticity-driven crack initiation. An early stage of the plasticity-driven crack growth was sensitive to crack length and remote stress, accordingly, the crack growth rate in the early stage increased with increasing initial defect size. On one hand, in a late stage of the crack growth, the crack propagation rate did not show simple trend against the crack length, which is perhaps due to stress field around the crack tip that depends on initial defect size. In this chapter, we confirmed that the structure strength of very ductile, slightly hydrogen susceptible steels, i.e. TWIP steels is mainly determined by the stable crack propagation properties which is not influenced by the specific feature of the bimodal microstructure.

Chapter 4 focuses on the effect of the different precrack length introduced by fatigue on the hydrogen-assisted cracking in the uniform-grained TWIP steel. Hydrogen was introduced to the specimens by electrochemical hydrogen charging during the slow strain rate of 10^{-4} s^{-1} under tension. The use of precracked in slow strain rate testing has important advantages, the main one being the localization of the hydrogen and stress in the vicinity of the crack tip.

Different crack lengths can induce different local strain rates in front of the crack tip. The results showed that there is a critical precrack length which hydrogen does not have any effect larger than that. There is, however, an important interpretation of results that the local strain rate at the crack tip, and not the externally applied strain rate, is the variable that controls the hydrogen-assisted cracking in the cracked specimens and should be considered as an effective variable even in the slow strain rate tensile test.

Chapter 5 describes the effect of very slow strain rate of 10^{-5} s^{-1} in precracked TWIP steel specimens. The reduction in strain rate did not have any influence in uncharged specimens. By contrast, the susceptibility of hydrogen embrittlement increased dramatically by reducing the strain rate in the cracked specimens. Particularly, specimens which have not shown any effect of hydrogen on mechanical properties in the chapter 4 showed sensitivity to hydrogen embrittlement at lower strain rate.

Chapter 6 summarized the results and proposed the outlook.

1.4 List of appended papers during Ph.D. period: include publications

[1]. Abbas Mohammadi, Motomichi Koyama, Gregory Gerstein, Hans Jurgen Maier, Hiroshi Noguchi. *Hydrogen-assisted failure in a bimodal twinning-induced plasticity steel: Delamination events and damage evolution.* International Journal of Hydrogen Energy 2018, 43: 2492-2502.

1.5 Refrences

[1] M. Louthan Jr, G. Caskey Jr, J. Donovan, D. Rawl Jr, Hydrogen embrittlement of metals, Materials Science and Engineering, 10 (1972) 357-368.

[2] W.H. Johnson, II. On some remarkable changes produced in iron and steel by the action of hydrogen and acids, Proceedings of the Royal Society of London, 23 (1875) 168-179.

[3] R. Latanision, H. Opperhauser, The intergranular embrittlement of nickel by hydrogen: the effect of grain boundary segregation, Metallurgical Transactions, 5 (1974) 483-492.

[4] R. Gest, A. Troiano, Stress corrosion and hydrogen embrittlement in an aluminum alloy, Corrosion, 30 (1974) 274-279.

[5] H.G. Nelson, D.P. Williams, J.E. Stein, Environmental hydrogen embrittlement of an α-β titanium alloy: effect of microstructure, Metallurgical and Materials Transactions B, 3 (1972) 473-479.

[6] F. Yunchang, D. Koss, The influence of multiaxial states of stress on the hydrogen embrittlement of zirconium alloy sheet, Metallurgical Transactions A, 16 (1985) 675-681.

[7] R.E. Buxbaum, A.B. Kinney, Hydrogen transport through tubular membranes of palladium-coated tantalum and niobium, Industrial & Engineering Chemistry Research, 35 (1996) 530-537.

[8] H. Yukawa, T. Nambu, Y. Matsumoto, N. Watanabe, G. Zhang, M. Morinaga, Alloy design of Nb-based hydrogen permeable membrane with strong resistance to hydrogen embrittlement, Materials transactions, 49 (2008) 2202-2207.

[9] T. Muroga, T. Nagasaka, K. Abe, V. Chernov, H. Matsui, D. Smith, Z.-Y. Xu, S. Zinkle, Vanadium alloys–overview and recent results, Journal of Nuclear Materials, 307 (2002) 547-554.

[10] C. Ma, J. Sheng, N. Brandon, C. Zhang, G. Li, Preparation of tungsten carbide-supported nano platinum catalyst and its electrocatalytic activity for hydrogen evolution,

International Journal of Hydrogen Energy, 32 (2007) 2824-2829.

[11] R. Dayal, N. Parvathavarthini, Hydrogen embrittlement in power plant steels, Sadhana, 28 (2003) 431-451.

[12] A.R. Troiano, The role of hydrogen and other interstitials in the mechanical behavior of metals, trans. ASM, 52 (1960) 54-80.

[13] R. Oriani, P. Josephic, Equilibrium aspects of hydrogen-induced cracking of steels, Acta metallurgica, 22 (1974) 1065-1074.

[14] R.A. Oriani, The diffusion and trapping of hydrogen in steel, Acta metallurgica, 18 (1970) 147-157.

[15] R. Oriani, Whitney award lecture—1987: hydrogen—the versatile embrittler, Corrosion, 43 (1987) 390-397.

[16] C. Beachem, A new model for hydrogen-assisted cracking (hydrogen "embrittlement"), Metallurgical and Materials Transactions B, 3 (1972) 441-455.

[17] D.P. Abraham, C.J. Altstetter, Hydrogen-enhanced localization of plasticity in an austenitic stainless steel, Metallurgical and Materials transactions A, 26 (1995) 2859-2871.

[18] Y. Liang, D. Ahn, P. Sofronis, R. Dodds Jr, D. Bammann, Effect of hydrogen trapping on void growth and coalescence in metals and alloys, Mechanics of Materials, 40 (2008) 115-132.

[19] I. Robertson, The effect of hydrogen on dislocation dynamics, Engineering Fracture Mechanics, 64 (1999) 649-673.

[20] S. Lynch, Environmentally assisted cracking: overview of evidence for an adsorption-induced localised-slip process, Acta Metallurgica, 36 (1988) 2639-2661.

[21] S. Lynch, Hydrogen embrittlement (HE) phenomena and mechanisms, in: Stress Corrosion Cracking, Elsevier, 2011, pp. 90-130.

[22] M. Nagumo, Hydrogen related failure of steels–a new aspect, Materials Science and

Technology, 20 (2004) 940-950.

[23] A. Cuitino, M. Ortiz, Ductile fracture by vacancy condensation in fcc single crystals, Acta materialia, 44 (1996) 427-436.

[24] R. Gardner, H. Wilsdorf, Ductile fracture initiation in pure α-Fe: Part II. Microscopic observations of an initiation mechanism, Metallurgical Transactions A, 11 (1980) 659-669.

[25] K. Takai, H. Shoda, H. Suzuki, M. Nagumo, Lattice defects dominating hydrogen-related failure of metals, Acta Materialia, 56 (2008) 5158-5167.

[26] J. Tien, A.W. Thompson, I. Bernstein, R.J. Richards, Hydrogen transport by dislocations, Metallurgical Transactions A, 7 (1976) 821-829.

[27] J. Toribio, The role of crack tip strain rate in hydrogen assisted cracking, Corrosion Science, 39 (1997) 1687-1697.

[28] B. Bal, M. Koyama, G. Gerstein, H. Maier, K. Tsuzaki, Effect of strain rate on hydrogen embrittlement susceptibility of twinning-induced plasticity steel pre-charged with high-pressure hydrogen gas, international journal of hydrogen energy, 41 (2016) 15362-15372.

[29] J. Zhao, Z. Jiang, Thermomechanical processing of advanced high strength steels, Progress in Materials Science, 94 (2018) 174-242.

[30] B. De Cooman, L. Chen, H.S. Kim, Y. Estrin, S. Kim, H. Voswinckel, State-of-the-science of high manganese TWIP steels for automotive applications, in: Microstructure and Texture in Steels, Springer, 2009, pp. 165-183.

[31] R.A. Hadfield, Science, (1888) 284-286.

[32] S. Asgari, E. El-Danaf, S.R. Kalidindi, R.D. Doherty, Strain hardening regimes and microstructural evolution during large strain compression of low stacking fault energy fcc alloys that form deformation twins, Metallurgical and Materials Transactions A, 28 (1997) 1781-1795.

[33] P. Adler, G. Olson, W. Owen, Strain hardening of Hadfield manganese steel, Metallurgical and Materials Transactions A, 17 (1986) 1725-1737.

[34] T. Shun, C. Wan, J. Byrne, A study of work hardening in austenitic Fe□ Mn□ C and Fe□ Mn□ Al□ C alloys, Acta metallurgica et materialia, 40 (1992) 3407-3412.

[35] J.-K. Kim, L. Chen, H.-S. Kim, S.-K. Kim, Y. Estrin, B. De Cooman, On the tensile behavior of high-manganese twinning-induced plasticity steel, Metallurgical and Materials Transactions A, 40 (2009) 3147.

[36] L. Remy, Kinetics of fcc deformation twinning and its relationship to stress-strain behaviour, Acta Metallurgica, 26 (1978) 443-451.

[37] S. Allain, J.-P. Chateau, O. Bouaziz, S. Migot, N. Guelton, Correlations between the calculated stacking fault energy and the plasticity mechanisms in Fe–Mn–C alloys, Materials Science and Engineering: A, 387 (2004) 158-162.

[38] O. Bouaziz, S. Allain, C. Scott, Effect of grain and twin boundaries on the hardening mechanisms of twinning-induced plasticity steels, Scripta Materialia, 58 (2008) 484-487.

[39] H. Idrissi, K. Renard, D. Schryvers, P. Jacques, On the relationship between the twin internal structure and the work-hardening rate of TWIP steels, Scripta Materialia, 63 (2010) 961-964.

[40] R. Stringfellow, D. Parks, G. Olson, A constitutive model for transformation plasticity accompanying strain-induced martensitic transformations in metastable austenitic steels, Acta Metallurgica et Materialia, 40 (1992) 1703-1716.

[41] R. Ueji, N. Tsuchida, D. Terada, N. Tsuji, Y. Tanaka, A. Takemura, K. Kunishige, Tensile properties and twinning behavior of high manganese austenitic steel with fine-grained structure, Scripta Materialia, 59 (2008) 963-966.

[42] K.-T. Park, K.G. Jin, S.H. Han, S.W. Hwang, K. Choi, C.S. Lee, Stacking fault energy and plastic deformation of fully austenitic high manganese steels: Effect of Al addition,

Materials Science and Engineering: A, 527 (2010) 3651-3661.

[43] L. Remy, A. Pineau, Twinning and strain-induced FCC→ HCP transformation in the Fe□ Mn□ Cr□ C system, Materials Science and engineering, 28 (1977) 99-107.

[44] B. De Cooman, O. Kwon, K.-G. Chin, State-of-the-knowledge on TWIP steel, Materials Science and Technology, 28 (2012) 513-527.

[45] S. Curtze, V.-T. Kuokkala, Dependence of tensile deformation behavior of TWIP steels on stacking fault energy, temperature and strain rate, Acta materialia, 58 (2010) 5129-5141.

[46] Y.-K. Lee, Microstructural evolution during plastic deformation of twinning-induced plasticity steels, Scripta Materialia, 66 (2012) 1002-1006.

[47] M.B. Whiteman, A.R. Troiano, The Influence of Hydrogen on the Stacking Fault Energy of an Austenitic Stainless Steel, physica status solidi (b), 7 (1964) K109-K110.

[48] A.E. Pontini, J.D. Hermida, X-ray diffraction measurement of the stacking fault energy reduction induced by hydrogen in an AISI 304 steel, Scripta Materialia, 37 (1997) 1831-1837.

[49] P. Rozenak, D. Eliezer, Phase changes related to hydrogen-induced cracking in austenitic stainless steel, Acta Metallurgica, 35 (1987) 2329-2340.

[50] N. Narita, C.J. Altstetter, H.K. Birnbaum, HYDROGEN-RELATED PHASE TRANSFORMATIONS IN AUSTENITIC STAINLESS STEELS, Metallurgical transactions. A, Physical metallurgy and materials science, 13 A (1982) 1355-1365.

[51] J.M. Rigsbee, R.B. Benson Jun, A TEM investigation of hydrogen-induced deformation twinning and associated martensitic phases in 304-type stainless steel, Journal of Materials Science, 12 (1977) 406-409.

[52] E.G. Astafurova, G.G. Zakharova, H.J. Maier, Hydrogen-induced twinning in 〈0 0 1〉 Hadfield steel single crystals, Scripta Materialia, 63 (2010) 1189-1192.

[53] K.-G. Chin, C.-Y. Kang, S.Y. Shin, S. Hong, S. Lee, H.S. Kim, K.-h. Kim, N.J. Kim,

Effects of Al addition on deformation and fracture mechanisms in two high manganese TWIP steels, Materials Science and Engineering: A, 528 (2011) 2922-2928.

[54] I.-J. Park, K.-H. Jeong, J.-G. Jung, C.S. Lee, Y.-K. Lee, The mechanism of enhanced resistance to the hydrogen delayed fracture in Al-added Fe–18Mn–0.6 C twinning-induced plasticity steels, international journal of hydrogen energy, 37 (2012) 9925-9932.

[55] K.H. So, J.S. Kim, Y.S. Chun, K.-T. Park, Y.-K. Lee, C.S. Lee, Hydrogen delayed fracture properties and internal hydrogen behavior of a Fe–18Mn–1.5 Al–0.6 C TWIP steel, ISIJ international, 49 (2009) 1952-1959.

[56] J.-K. Jung, O.-Y. Lee, Y.-K. Park, D.-E. Kim, K.-G. Jin, Hydrogen embrittlement behavior of high Mn TRIP/TWIP steels, Korean Journal of Materials Research, 18 (2008) 394-399.

[57] J. Ronevich, S. Kim, J. Speer, D. Matlock, Hydrogen effects on cathodically charged twinning-induced plasticity steel, Scripta Materialia, 66 (2012) 956-959.

[58] J. Ronevich, B. De Cooman, J. Speer, E. De Moor, D. Matlock, Hydrogen effects in prestrained transformation induced plasticity steel, Metallurgical and Materials Transactions A, 43 (2012) 2293-2301.

[59] D.-W. Suh, Critical assessment 2: hydrogen induced fracture in austenitic, high-manganese TWIP steel, Materials Science and Technology, 30 (2014) 1131-1134.

[60] M. Koyama, E. Akiyama, K. Tsuzaki, Hydrogen embrittlement in a Fe–Mn–C ternary twinning-induced plasticity steel, Corrosion Science, 54 (2012) 1-4.

[61] M. Koyama, E. Akiyama, K. Tsuzaki, Effect of hydrogen content on the embrittlement in a Fe–Mn–C twinning-induced plasticity steel, Corrosion Science, 59 (2012) 277-281.

[62] M. Koyama, E. Akiyama, T. Sawaguchi, D. Raabe, K. Tsuzaki, Hydrogen-induced cracking at grain and twin boundaries in an Fe–Mn–C austenitic steel, Scripta Materialia, 66 (2012) 459-462.

[63] A. Dumay, J.-P. Chateau, S. Allain, S. Migot, O. Bouaziz, Influence of addition elements on the stacking-fault energy and mechanical properties of an austenitic Fe–Mn–C steel, Materials Science and Engineering: A, 483 (2008) 184-187.

[64] J. Kim, S.-J. Lee, B.C. De Cooman, Effect of Al on the stacking fault energy of Fe–18Mn–0.6 C twinning-induced plasticity, Scripta Materialia, 65 (2011) 363-366.

[65] Y.S. Chun, K.-T. Park, C.S. Lee, Delayed static failure of twinning-induced plasticity steels, Scripta materialia, 66 (2012) 960-965.

[66] J.H. Ryu, S.K. Kim, C.S. Lee, D.-W. Suh, H. Bhadeshia, Effect of aluminium on hydrogen-induced fracture behaviour in austenitic Fe–Mn–C steel, Proc. R. Soc. A, 469 (2013) 20120458.

[67] M. Koyama, E. Akiyama, K. Tsuzaki, D. Raabe, Hydrogen-assisted failure in a twinning-induced plasticity steel studied under in situ hydrogen charging by electron channeling contrast imaging, Acta Materialia, 61 (2013) 4607-4618.

[68] M. Koyama, E. Akiyama, Y.-K. Lee, D. Raabe, K. Tsuzaki, Overview of hydrogen embrittlement in high-Mn steels, international journal of hydrogen energy, 42 (2017) 12706-12723.

[69] M. Koyama, S. Okazaki, T. Sawaguchi, K. Tsuzaki, Hydrogen Embrittlement Susceptibility of Fe-Mn Binary Alloys with High Mn Content: Effects of Stable and Metastable ε-Martensite, and Mn Concentration, Metallurgical and Materials Transactions A: Physical Metallurgy and Materials Science, 47 (2016) 2656-2673.

[70] S.M. Lee, I.J. Park, J.G. Jung, Y.K. Lee, The effect of Si on hydrogen embrittlement of Fe-18Mn-0.6C-xSi twinning-induced plasticity steels, Acta Materialia, 103 (2016) 264-272.

[71] T. Dieudonné, L. Marchetti, M. Wery, J. Chêne, C. Allely, P. Cugy, C.P. Scott, Role of copper and aluminum additions on the hydrogen embrittlement susceptibility of austenitic

Fe-Mn-C TWIP steels, Corrosion Science, 82 (2014) 218-226.

[72] D. Raabe, M. Herbig, S. Sandlöbes, Y. Li, D. Tytko, M. Kuzmina, D. Ponge, P.P. Choi, Grain boundary segregation engineering in metallic alloys: A pathway to the design of interfaces, Current Opinion in Solid State and Materials Science, 18 (2014) 253-261.

[73] M. Kuzmina, D. Ponge, D. Raabe, Grain boundary segregation engineering and austenite reversion turn embrittlement into toughness: Example of a 9 wt.% medium Mn steel, Acta Materialia, 86 (2015) 182-192.

[74] R. Saha, R. Ueji, N. Tsuji, Fully recrystallized nanostructure fabricated without severe plastic deformation in high-Mn austenitic steel, Scripta Materialia, 68 (2013) 813-816.

[75] Y. Bai, Y. Momotani, M.C. Chen, A. Shibata, N. Tsuji, Effect of grain refinement on hydrogen embrittlement behaviors of high-Mn TWIP steel, Materials Science and Engineering: A, 651 (2016) 935-944.

[76] M. Calcagnotto, D. Ponge, D. Raabe, Effect of grain refinement to 1μm on strength and toughness of dual-phase steels, Materials Science and Engineering: A, 527 (2010) 7832-7840.

[77] T.G. Langdon, Twenty-five years of ultrafine-grained materials: Achieving exceptional properties through grain refinement, Acta Materialia, 61 (2013) 7035-7059.

[78] M. Wang, E. Akiyama, K. Tsuzaki, Effect of hydrogen on the fracture behavior of high strength steel during slow strain rate test, Corrosion Science, 49 (2007) 4081-4097.

[79] D. Hardie, E.A. Charles, A.H. Lopez, Hydrogen embrittlement of high strength pipeline steels, Corrosion Science, 48 (2006) 4378-4385.

[80] Y. Nie, Y. Kimura, T. Inoue, F. Yin, E. Akiyama, K. Tsuzaki, Hydrogen Embrittlement of a 1500-MPa Tensile Strength Level Steel with an Ultrafine Elongated Grain Structure, Metallurgical and Materials Transactions A, 43 (2012) 1670-1687.

[81] Y. Kimura, Y. Sakai, T. Hara, A. Belyakov, K. Tsuzaki, Hydrogen induced delayed

fracture of ultrafine grained 0.6% O steel with dispersed oxide particles, Scripta Materialia, 49 (2003) 1111-1116.

[82] I.-J. Park, S.-m. Lee, H.-h. Jeon, Y.-K. Lee, The advantage of grain refinement in the hydrogen embrittlement of Fe–18Mn–0.6C twinning-induced plasticity steel, Corrosion Science, 93 (2015) 63-69.

[83] N. Zan, H. Ding, X. Guo, Z. Tang, W. Bleck, Effects of grain size on hydrogen embrittlement in a Fe-22Mn-0.6C TWIP steel, International Journal of Hydrogen Energy, 40 (2015) 10687-10696.

[84] K. Takasawa, R. Ikeda, N. Ishikawa, R. Ishigaki, Effects of grain size and dislocation density on the susceptibility to high-pressure hydrogen environment embrittlement of high-strength low-alloy steels, International Journal of Hydrogen Energy, 37 (2012) 2669-2675.

[85] A. Oudriss, J. Creus, J. Bouhattate, E. Conforto, C. Berziou, C. Savall, X. Feaugas, Grain size and grain-boundary effects on diffusion and trapping of hydrogen in pure nickel, Acta Materialia, 60 (2012) 6814-6828.

[86] S. Allain, J.P. Chateau, O. Bouaziz, A physical model of the twinning-induced plasticity effect in a high manganese austenitic steel, Materials Science and Engineering: A, 387–389 (2004) 143-147.

[87] A. Saeed-Akbari, L. Mosecker, A. Schwedt, W. Bleck, Characterization and Prediction of Flow Behavior in High-Manganese Twinning Induced Plasticity Steels: Part I. Mechanism Maps and Work-Hardening Behavior, Metallurgical and Materials Transactions A, 43 (2012) 1688-1704.

[88] I. Gutierrez-Urrutia, S. Zaefferer, D. Raabe, The effect of grain size and grain orientation on deformation twinning in a Fe–22 wt.% Mn–0.6 wt.% C TWIP steel, Materials Science and Engineering: A, 527 (2010) 3552-3560.

[89] K. Takasawa, Y. Wada, R. Ishigaki, R. Kayano, Effects of Grain Size on Hydrogen

Environment Embrittlement of High Strength Low Alloy Steel in 45 MPa Gaseous Hydrogen, MATERIALS TRANSACTIONS, 51 (2010) 347-353.

[90] A. Oudriss, J. Creus, J. Bouhattate, C. Savall, B. Peraudeau, X. Feaugas, The diffusion and trapping of hydrogen along the grain boundaries in polycrystalline nickel, Scripta Materialia, 66 (2012) 37-40.

[91] M. Koyama, E. Akiyama, K. Tsuzaki, Hydrogen-induced delayed fracture of a Fe–22Mn–0.6C steel pre-strained at different strain rates, Scripta Materialia, 66 (2012) 947-950.

[92] E. Akiyama, S. Matsuoka, Hydrogen Visualization in Steels Using Ag Decoration Method, Materials transactions, 56 (2015) 793-797.

[93] O. Bouaziz, S. Allain, C.P. Scott, P. Cugy, D. Barbier, High manganese austenitic twinning induced plasticity steels: A review of the microstructure properties relationships, Current Opinion in Solid State and Materials Science, 15 (2011) 141-168.

[94] Y. Bai, Y. Momotani, M.C. Chen, A. Shibata, N. Tsuji, Effect of grain refinement on hydrogen embrittlement behaviors of high-Mn TWIP steel, Materials Science and Engineering A, 651 (2016) 935-944.

[95] N. Zan, H. Ding, X. Guo, Z. Tang, W. Bleck, Effects of grain size on hydrogen embrittlement in a Fe-22Mn-0.6 C TWIP steel, International Journal of Hydrogen Energy, 40 (2015) 10687-10696.

[96] I. Gutierrez-Urrutia, D. Raabe, Grain size effect on strain hardening in twinning-induced plasticity steels, Scripta Materialia, 66 (2012) 992-996.

[97] S. Patra, S.M. Hasan, N. Narasaiah, D. Chakrabarti, Effect of bimodal distribution in ferrite grain sizes on the tensile properties of low-carbon steels, Materials Science and Engineering A, 538 (2012) 145-155.

[98] Y. Wang, M. Chen, F. Zhou, E. Ma, High tensile ductility in a nanostructured metal,

Nature, 419 (2002) 912-915.

[99] J. Gil Sevillano, J. Aldazabal, Ductilization of nanocrystalline materials for structural applications, Scripta Materialia, 51 (2004) 795-800.

[100] M.C. Zhao, F. Yin, T. Hanamura, K. Nagai, A. Atrens, Relationship between yield strength and grain size for a bimodal structural ultrafine-grained ferrite/cementite steel, Scripta Materialia, 57 (2007) 857-860.

[101] H. Qiu, R. Ito, K. Hiraoka, Role of grain size on the strength and ductile-brittle transition temperature in the dual-sized ferrite region of the heat-affected zone of ultra-fine grained steel, Materials Science and Engineering A, 435-436 (2006) 648-652.

[102] H. Qiu, R. Ito, K. Hiraoka, Role of grain size on the strength and ductile–brittle transition temperature in the dual-sized ferrite region of the heat-affected zone of ultra-fine grained steel, Materials Science and Engineering: A, 435-436 (2006) 648-652.

[103] G.J. Fan, H. Choo, P.K. Liaw, E.J. Lavernia, Plastic deformation and fracture of ultrafine-grained Al–Mg alloys with a bimodal grain size distribution, Acta Materialia, 54 (2006) 1759-1766.

[104] H. Jin, D.J. Lloyd, Effect of a duplex grain size on the tensile ductility of an ultra-fine grained Al–Mg alloy, AA5754, produced by asymmetric rolling and annealing, Scripta Materialia, 50 (2004) 1319-1323.

[105] B.O. Han, E.J. Lavernia, Z. Lee, S. Nutt, D. Witkin, Deformation behavior of bimodal nanostructured 5083 Al alloys, Metallurgical and Materials Transactions A, 36 (2005) 957-965.

[106] G. Dini, A. Najafizadeh, R. Ueji, S.M. Monir-Vaghefi, Improved tensile properties of partially recrystallized submicron grained TWIP steel, Materials Letters, 64 (2010) 15.

[107] J.R. Rice, The localization of plastic deformation, (1976).

[108] X.-P. Xu, A. Needleman, Void nucleation by inclusion debonding in a crystal matrix,

Modelling and Simulation in Materials Science and Engineering, 1 (1993) 111.

[109] A.L. Gurson, Continuum theory of ductile rupture by void nucleation and growth: Part I—Yield criteria and flow rules for porous ductile media, Journal of engineering materials and technology, 99 (1977) 2-15.

[110] V. Orsini, M. Zikry, Void growth and interaction in crystalline materials, International Journal of Plasticity, 17 (2001) 1393-1417.

[111] D. Teirlinck, F. Zok, J. Embury, M. Ashby, Fracture mechanism maps in stress space, Acta Metallurgica, 36 (1988) 1213-1228.

[112] G. Falkinger, P. Simon, An Investication of Modeling Approaches for Material Instability of Aluminum Sheet Metal using the GISSMO-Model, in: 10th European LS-DYNA Conference, 2015.

[113] P. Magnusen, E. Dubensky, D. Koss, The effect of void arrays on void linking during ductile fracture, Acta Metallurgica, 36 (1988) 1503-1509.

[114] B. Dodd, A. Atkins, Flow localization in shear deformation of void-containing and void-free solids, Acta Metallurgica, 31 (1983) 9-15.

[115] M. Koyama, H. Springer, S.V. Merzlikin, K. Tsuzaki, E. Akiyama, D. Raabe, Hydrogen embrittlement associated with strain localization in a precipitation-hardened Fe–Mn–Al–C light weight austenitic steel, international journal of hydrogen energy, 39 (2014) 4634-4646.

[116] C. San Marchi, B. Somerday, X. Tang, G. Schiroky, Effects of alloy composition and strain hardening on tensile fracture of hydrogen-precharged type 316 stainless steels, International Journal of Hydrogen Energy, 33 (2008) 889-904.

[117] J. Von Pezold, L. Lymperakis, J. Neugebeauer, Hydrogen-enhanced local plasticity at dilute bulk H concentrations: The role of H-H interactions and the formation of local hydrides, Acta Materialia, 59 (2011) 2969-2980.

[118] I.M. Robertson, P. Sofronis, A. Nagao, M. Martin, S. Wang, D. Gross, K. Nygren, Hydrogen embrittlement understood, Metallurgical and Materials Transactions A, 46 (2015) 2323-2341.

[119] I.M. Robertson, P. Sofronis, A. Nagao, M.L. Martin, S. Wang, D.W. Gross, K.E. Nygren, Hydrogen Embrittlement Understood, Metallurgical and Materials Transactions A, 46 (2015) 2323-2341.

[120] M.L. Martin, J.A. Fenske, G.S. Liu, P. Sofronis, I.M. Robertson, On the formation and nature of quasi-cleavage fracture surfaces in hydrogen embrittled steels, Acta Materialia, 59 (2011) 1601-1606.

[121] M. Koyama, E. Akiyama, T. Sawaguchi, D. Raabe, K. Tsuzaki, Hydrogen-induced cracking at grain and twin boundaries in an Fe-Mn-C austenitic steel, Scripta Materialia, 66 (2012) 459-462.

[122] M.E. Launey, P.-Y. Chen, J. McKittrick, R. Ritchie, Mechanistic aspects of the fracture toughness of elk antler bone, Acta biomaterialia, 6 (2010) 1505-1514.

[123] S. Tavares, J. Pardal, L. Lima, I. Bastos, A. Nascimento, J. De Souza, Characterization of microstructure, chemical composition, corrosion resistance and toughness of a multipass weld joint of superduplex stainless steel UNS S32750, Materials Characterization, 58 (2007) 610-616.

[124] D. Dumont, A. Deschamps, Y. Brechet, On the relationship between microstructure, strength and toughness in AA7050 aluminum alloy, Materials Science and Engineering: A, 356 (2003) 326-336.

[125] A.G. Evans, Perspective on the development of high-toughness ceramics, Journal of the American Ceramic society, 73 (1990) 187-206.

[126] R.O. Ritchie, Mechanisms of fatigue-crack propagation in ductile and brittle solids, International journal of Fracture, 100 (1999) 55-83.

[127] C.-S. Chen, P.A. Wawrzynek, A.R. Ingraffea, Elastic-plastic crack growth simulation and residual strength prediction of thin plates with single and multiple cracks, in: Fatigue and Fracture Mechanics: 29th Volume, ASTM International, 1999.

[128] M.E. Launey, R.O. Ritchie, On the fracture toughness of advanced materials, Advanced Materials, 21 (2009) 2103-2110.

[129] Y. Deng, A. Barnoush, Hydrogen embrittlement revealed via novel in situ fracture experiments using notched micro-cantilever specimens, Acta Materialia, 142 (2018) 236-247.

[130] G. Bertolino, G. Meyer, J.P. Ipina, In situ crack growth observation and fracture toughness measurement of hydrogen charged Zircaloy-4, Journal of nuclear materials, 322 (2003) 57-65.

[131] D. Ahn, P. Sofronis, R. Dodds, Modeling of hydrogen-assisted ductile crack propagation in metals and alloys, International Journal of Fracture, 145 (2007) 135-157.

[132] B.P. Somerday, M. Dadfarnia, D.K. Balch, K.A. Nibur, C.H. Cadden, P. Sofronis, Hydrogen-Assisted Crack Propagation in Austenitic Stainless Steel Fusion Welds, Metallurgical and Materials Transactions A, 40 (2009) 2350-2362.

[133] R. Falkenberg, W. Brocks, W. Dietzel, I. Scheider, Modelling the effect of hydrogen on ductile tearing resistance of steels: Dedicated to Professor Dr. Hermann Riedel on the occasion of his 65th birthday, International Journal of Materials Research, 101 (2010) 989-996.

[134] G. Bertolino, G. Meyer, J. Perez Ipiña, Degradation of the mechanical properties of Zircaloy-4 due to hydrogen embrittlement, Journal of Alloys and Compounds, 330-332 (2002) 408-413.

[135] Y.S. Chun, K.T. Park, C.S. Lee, Delayed static failure of twinning-induced plasticity steels, Scripta Materialia, 66 (2012) 960-965.

1.6 Figures

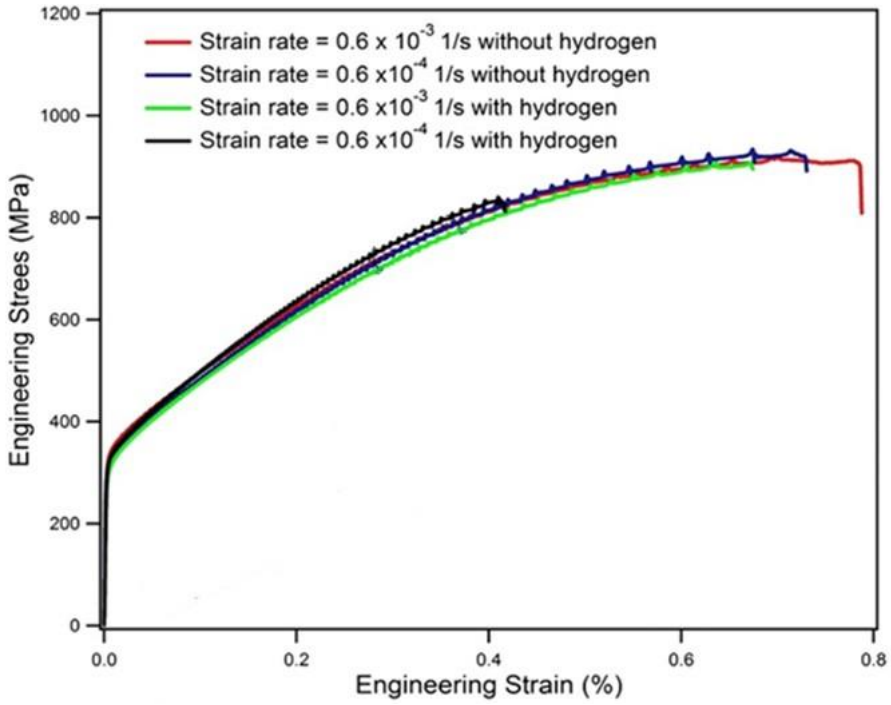

Figure 1.1. Tensile behavior of the Fe-23Mn-0.5C TWIP steels with and without hydrogen charging at different strain rates [28].

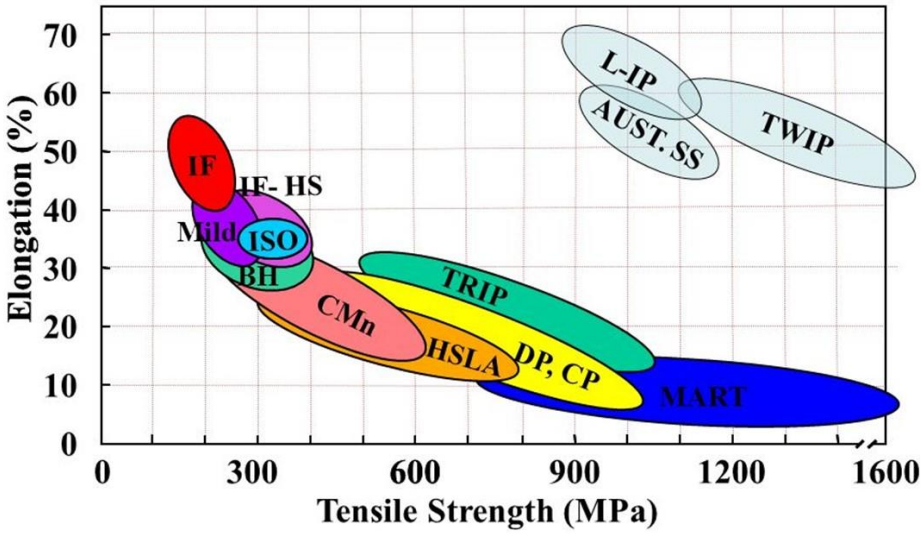

Figure 1.2. Superior combination of strength and elongation of TWIP steels compare to other materials [29].

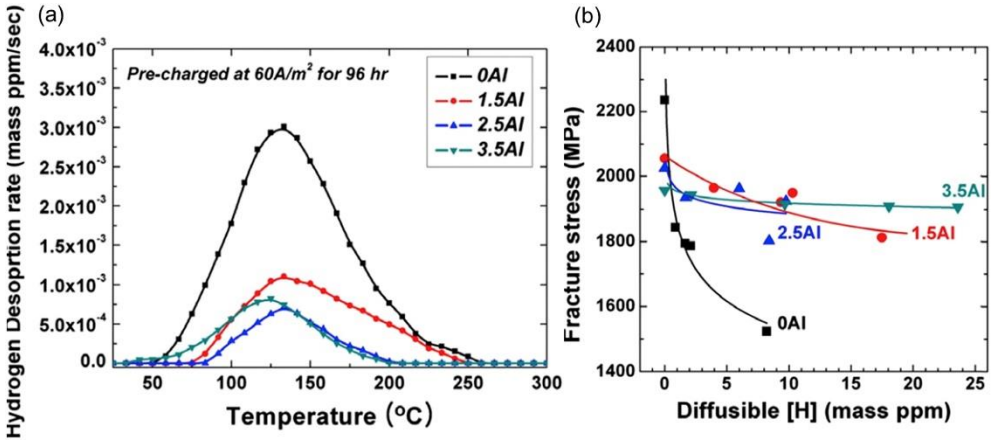

Figure 1.3. (a) TDA profiles with different Al contents in Fe-18Mn-xAl TWIP steels at an identical hydrogen charging condition. (b) Fracture strength of notched specimens plotted against diffusible hydrogen content obtained from Fig. 1.3a . Alloy compositions are given in weight % [135].

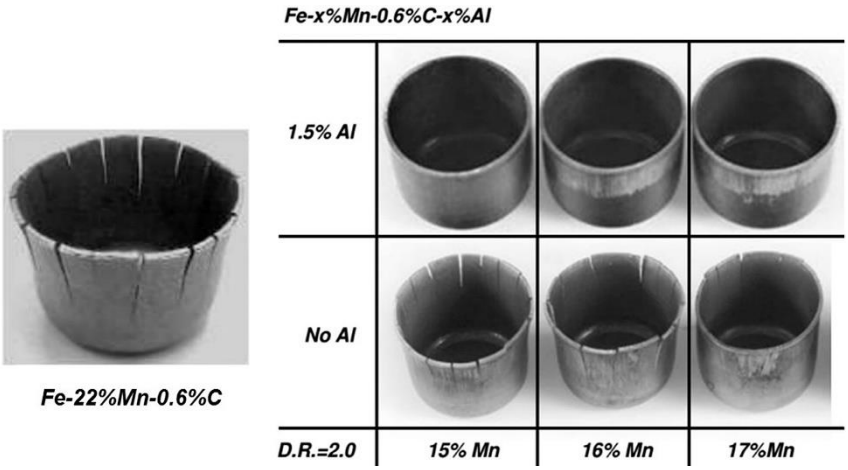

Figure 1.4. Hydrogen-induced delayed fracture in Al-free TWIP steel and its suppression by the addition of Al. D.R.: drawing ratio. % refers to weight % [68].

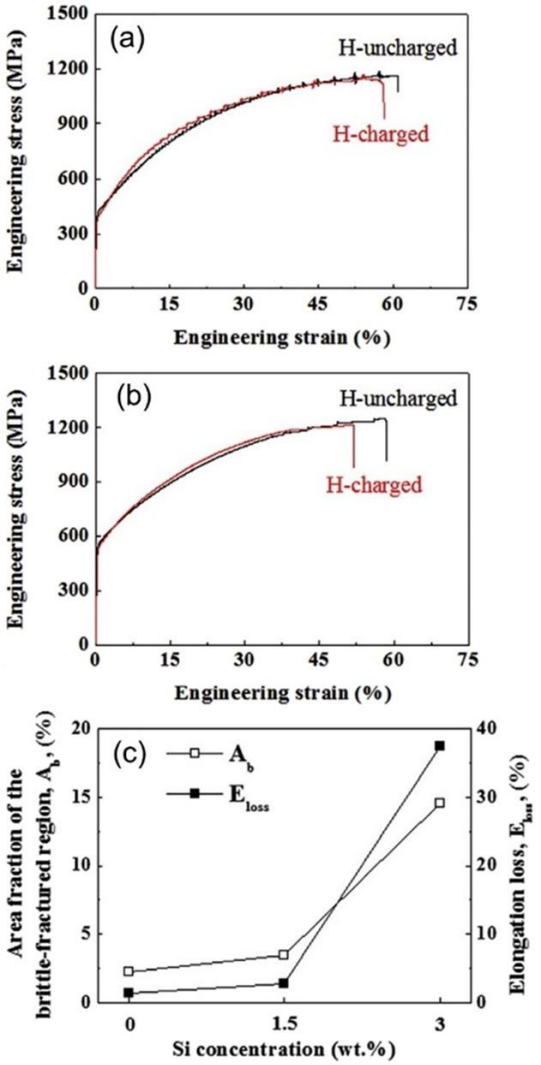

Fig. 1.5. Effect of Si on hydrogen embrittlement susceptibility in (a) Fe- 8Mn-0.6C and (b) Fe-18Mn-0.6C-1.6Si steels pre-hydrogen-charged at a current density of 50 A/m^2 in a 3% NaCl + 0.3% NH_4SCN aqueous solution. (c) Si concentration dependence of area fraction of the brittle-fracture region and elongation loss. The initial strain rate is 4.8×10^{-5} s^{-1}. Alloy compositions are given in weight % [70].

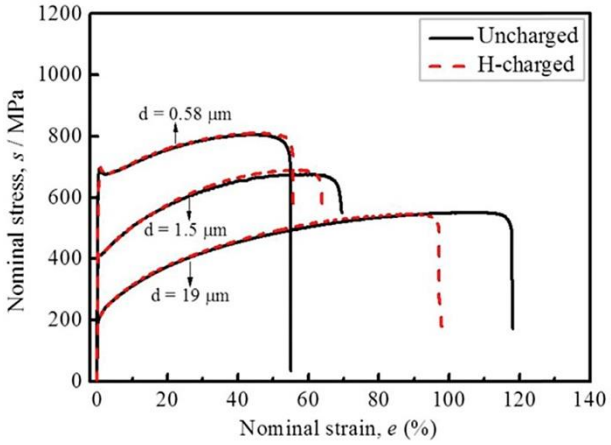

Fig. 1.6. Impact of grain refinement on hydrogen embrittlement in an Fe-31Mn-3Al-3Si TWIP steel hydrogen-pre-charged at 100 A/m^2 in a 3% NaCl aqueous solution containing 3 g/L of NH_4SCN. The initial strain rate is 8.3×10^{-6} s^{-1}. Alloy composition is given in weight %[94].

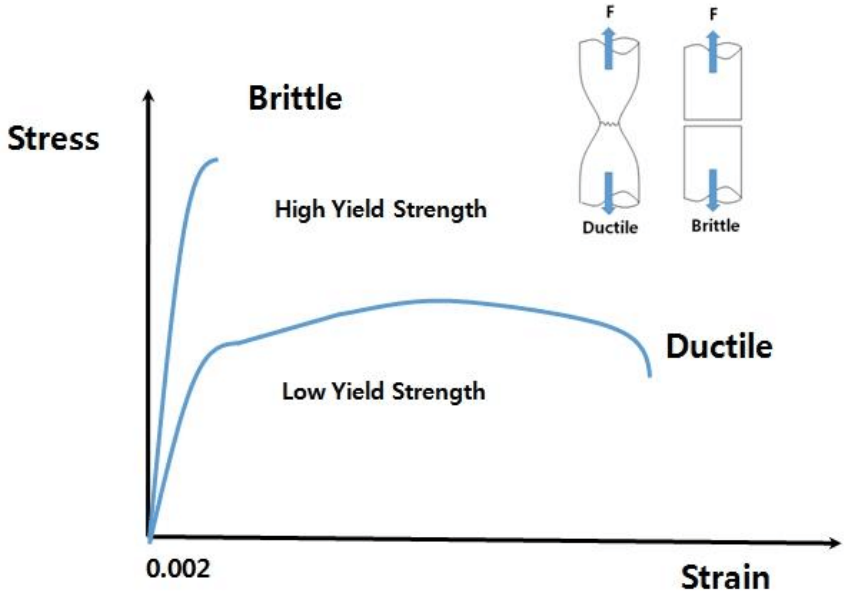

Fig. 1.7. Ductile versus brittle failure. Ductile failure is accompanied by extensive plastic deformation and energy absorption (toughness) before fracture.

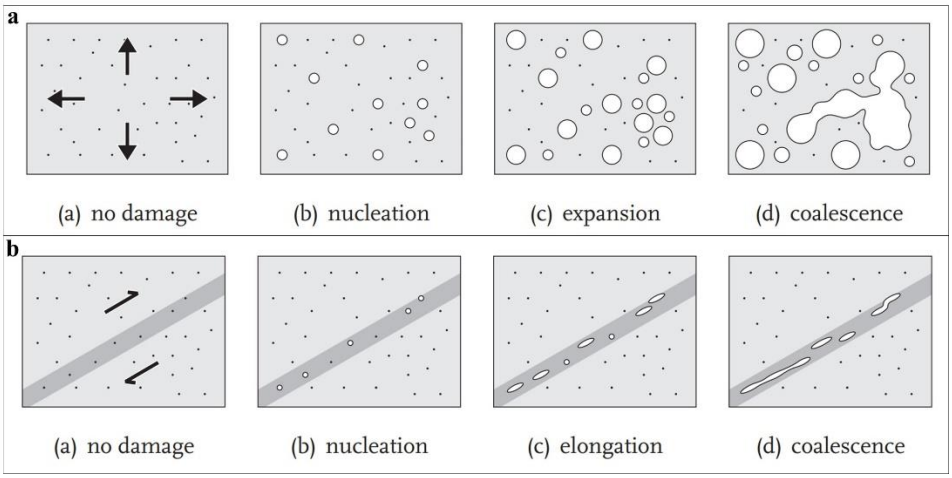

Figure 1.8. Schematic description of failure mechanism at (a) void growth and coalescence under hydrostatic tension, (b) void-sheeting under shear [112].

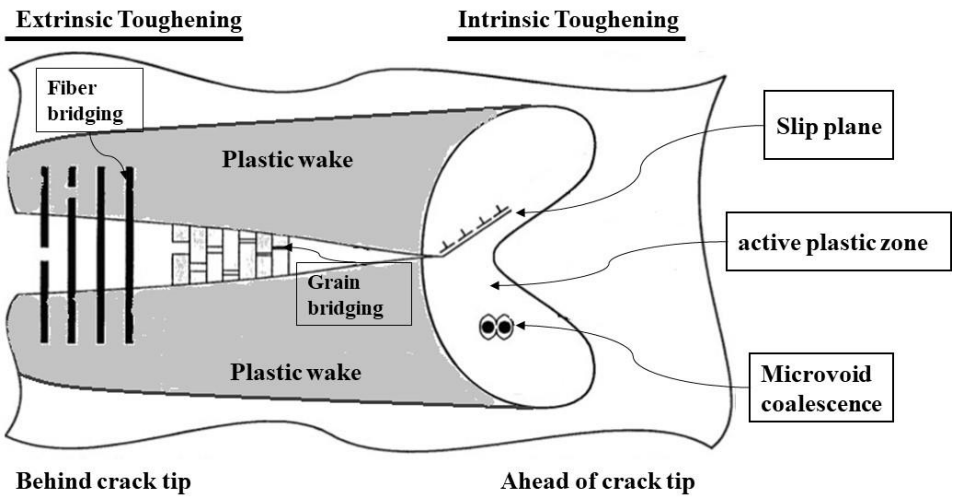

Figure 1.9. Schematic illustration of mutual competition between intrinsic mechanisms of damage/crack advance and extrinsic mechanisms of crack-tip shielding involved in crack growth [127, 128].

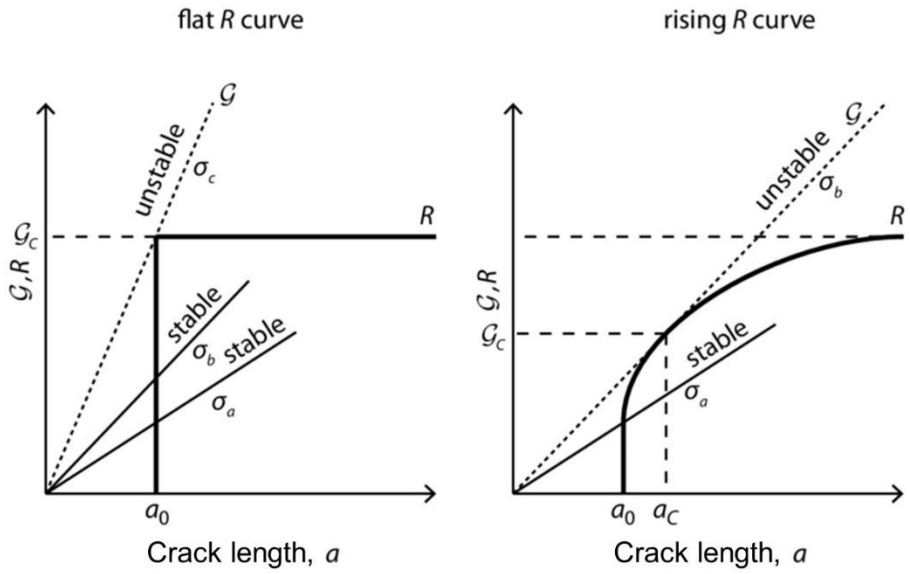

Figure 1.10: Schematic plots of a flat and a rising R curve for a fracture of the length a_0. Thick lines denote R, which is the length-dependent resistance of a fracture to propagation in terms of fracture energy G. Thin lines denote the available fracture energy in relation to the fracture length a at distinct load levels $\sigma_a < \sigma_b < \sigma_c$. G_C is the fracture energy at which unstable fracture propagation takes place and a_C is the corresponding fracture length [126].

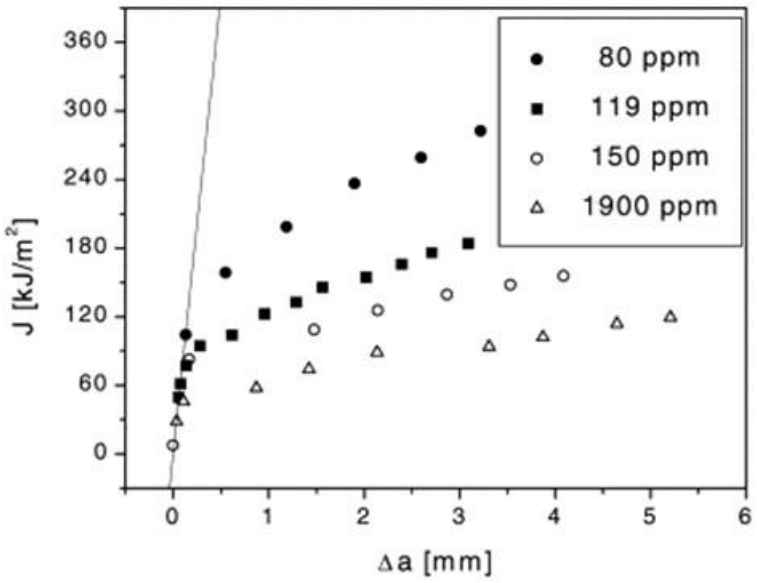

Fig. 1.11. J-R curve of Zircaloy-4 alloy for different hydrogen content at 293 K [134].

CHAPTER 2. Hydrogen-Assisted Failure in a Bimodal-grained TWIP Steel: Delamination Events and Damage Evolution

2.1 Introduction

Recently, high Mn-C twinning-induced plasticity (TWIP) austenitic steels have received increasing attention as potential next-generation high-strength materials for various loading conditions including operation at cryogenic temperatures [1-3], under cyclic loading [4-7], under high velocity loading [8-10], and in a hydrogen environment [11-14]. In particular, the close-packed structure of austenite has been expected to play an advantageous role in the resistance to hydrogen embrittlement owing to the low diffusivity [15-17]. A problem in austenitic steels is the low yield strength compared with the high strength of ferritic/martensitic steels. Therefore, steel researchers have attempted to increase the yield strength of austenitic TWIP steels.

A promising way to increase yield strength while maintaining austenite stability is grain refinement [18-21]. In general, hydrogen embrittlement susceptibility increases with increasing strength [22-24]. By contrast, the grain refinement methodology does not deteriorate resistance to hydrogen-related failure [24-29]. Thus, the effects of grain size on the deformation mechanisms and work hardening rates in TWIP steels have been intensively investigated [19, 30-32]. In fact, grain refinement enables the simultaneous improvement of the yield strength and the resistance to hydrogen-related failure. The reasons for the reduction in hydrogen embrittlement susceptibility are related to the local hydrogen content [27-29, 33, 34], local stress concentration [16, 35], and deformation twinning behavior [16, 35, 36]. In terms of the hydrogen content, grain-refined TWIP steel also shows a decrease in strength with increasing hydrogen content, but the loss of strength is significantly less than that of coarse-grained TWIP steels [27]. This can be attributed to the fact that the decreasing

grain size reduces the local hydrogen content at grain boundaries where hydrogen-assisted cracking occurs preferentially. According to previous studies [19, 37], the local stress concentration at grain boundaries in a fine-grained specimen is much lower than that in a coarse-grained one due to the decrease in the number of piled-up dislocations. This in turn reduces the accumulated local hydrogen content at the grain boundaries of the fine-grained specimen, which is a possible rationale for the improvement in the resistance to hydrogen embrittlement upon grain refinement [26, 27]. Certainly, the decrease in the local stress concentration at grain boundaries contributes to the decrease in hydrogen embrittlement susceptibility even without a reduction in the local hydrogen content. In addition, deformation twinning is suppressed by grain refinement [38, 39]. The interaction between twins and grain boundaries can lead to the growth of twins. As these act as crack initiation sites and propagation paths, the suppression of deformation twinning should also decrease the hydrogen susceptibility of TWIP steels [27, 35].

A fine/coarse bimodal grain distribution can drastically increase not only the yield and tensile strengths but also the ductility [40-46]. For example, pure copper with a bimodal grain structure and FCC structure like TWIP steels has a 400 MPa tensile strength with over 60% elongation, which is a much higher ductility/strength balance than that of homogeneously grain-refined copper [42]. The bimodal grain structure enhances the work hardening capability because of plastic strain inhomogeneity that causes a high accumulation rate of dislocations [42]. The enhanced work hardening delays the onset of necking, thus increasing the uniform elongation [42-44, 47, 48]. In the same context, a fully austenitic TWIP steel with a bimodal grain structure has been reported to feature a superior ductility/strength balance. For instance, a TWIP steel with the bimodal grain structure demonstrated 600 MPa 0.2% proof strength, 800 MPa tensile strength, and 35% elastic engineering strain [49].

However, no systematic work has been reported on the effects of the bimodal grain size distribution on hydrogen embrittlement in TWIP steel. In this paper, we report a microstructural analysis of hydrogen embrittlement in such a material to understand the mechanisms of crack initiation and propagation under hydrogen charging.

2.2 Experimental procedure

2.2.1 Material

In the present study a Fe-15Mn-2.5Al-2.5Si-0.7C (wt.%) fully austenitic TWIP steel with a bimodal grain structure that had been produced by warm rolling was used. As shown in Fig. 2.1 the as-received TWIP steel featured a bimodal microstructure with partial recrystallization. The micrograph in Fig. 2.1a was obtained by mechanical polishing with colloidal silica and chemical etching with a solution of 3% nital (nitric acid in ethanol), followed by cleaning with ethanol. In Fig. 2.1b the microstructure of the as-received condition characterized by electron backscatter diffraction (EBSD). The rolling-direction (RD)-inverse pole figure (IPF) map shows that the TWIP steel featured a bimodal grain size microstructure. Figures also demonstrates that the as-received steel has fine grains along coarse grain boundaries. The initial microstructure does not contain deformation twins. The corresponding grain distribution plotted in terms of the area fraction using EBSD indicated the grain size can be classified into two groups by the presence of two-separate peaks: fine grain size around 10 μm and coarse grain size around 100 μm, as shown in Fig. 2.2. The average grain size, including coarse and fine grains, is 25 μm.

From the steel plates tensile specimen with gauge dimensions of 4 mm in width, 0.4 mm in thickness and 10 mm in length were cut by electrical discharge machining. Next, the thickness of the specimens was reduced by mechanical grinding. The resulting specimen

geometry is shown in Fig. 2.3a. Finally, the surface of the specimens was mechanically polished to a mirror finish.

2.2.2 Tensile tests and microstructure characterization

Tensile tests were conducted with and without hydrogen charging at an initial strain rate of 10^{-5} s^{-1}. A test was carried out for each experimental condition. Hydrogen was introduced to the specimen during the tensile tests by electrochemical charging in a 3% NaCl aqueous solution containing 3 g L^{-1} of NH_4SCN at a current density of 30 A m^{-2}. With this approach, hydrogen could enter the specimen deeply via hydrogen-decorated dislocation motion. The solution was continually added to fully cover the gauge part of the specimen during the tensile tests. A platinum wire was used as the counter-electrode. A schematic and image of the experimental setup for in-situ hydrogen charged specimen are shown in Figs. 2.4a and 2.4b, respectively.

The fracture surface was observed by scanning electron microscopy (SEM) at an accelerating voltage of 15 kV. In addition, the SEM was used for secondary electron imaging and electron backscatter diffraction (EBSD) measurements of the hydrogen-charged specimen. The microstructure observations were carried out from two directions: (1) toward the specimen surface (Fig. 2.3b) and (2) toward a cut cross-section (Fig. 2.3c). For the microstructural characterization on the cross section, the fractured specimen was cut by a low-speed saw perpendicular to the fracture surface and parallel to the tensile axes. The EBSD measurements were conducted on the mechanically polished surface at an acceleration voltage of 20 kV with a beam step size of 70 nm. Figures 2.5a and 2.5b show the image of SEM and EBSD instruments, respectively, at the center of advanced instrumental analysis, Kyushu university employed in this research.

2.3 Results

2.3.1 Hydrogen effects on the mechanical response

Figure 2.6 shows engineering stress-engineering strain curves of the tensile tests of uncharged and hydrogen-charged specimens. Similar to other TWIP steels [13, 19, 50, 51], the present bimodal TWIP steel demonstrated a significant deterioration in the total elongation and ultimate tensile strength from 42% to 15% and from 910 to 720 MPa, respectively. Surface cracks formed, and, subsequently, failure occurred rapidly in the hydrogen-charged specimen.

2.3.2 Hydrogen-assisted cracking

Figure 2.7 exhibits surface of uncharged and hydrogen-charged specimens after failure. As shown in Figs. 2.7a and 2.7b, no significant defects were observed on the surface of the uncharged specimen. By contrast, a considerable number of sub-cracks was observed everywhere on the surface of the hydrogen-charged specimen after fracture, as shown in Figs. 2.7c and 2.7d. Most of these cracks were aligned approximately perpendicular to the tensile axis, similar to previous reports [16, 52]. The microstructural features of the sub-cracks were then characterized to understand the crack initiation mechanism in the bimodal microstructure through EBSD measurements.

The initial focus was on the crack initiation behavior of the hydrogen-charged specimen. Figure 2.8 shows an SEM image and the corresponding rolling direction (RD)-inverse pole figure (IPF) map around a transgranular sub-crack. The sub-crack had initiated in different sites within the interior of a coarse grain. Note that the deformation twins form along different twin planes, as shown in Fig. 2.8b. The transgranular crack is zigzagged (as indicated by the yellow arrows), which is related to the formation of the primary and secondary deformation twins. Furthermore, it can be observed that one crack initiation event

is associated with the deformation twins. It has been reported that twin-related cracking stems from twin–twin interactions [15, 53]. Figure 2.9 shows another example of the crack formation in a hydrogen-charged specimen in an RD-IPF map recorded around a crack formed along the grain boundaries between coarse and fine grains. It turned out that this type of cracking mode is the dominant one for the bimodal TWIP steel charged with hydrogen.

Next, hydrogen-assisted crack growth behavior was analyzed. Figure 2.10 shows an example of crack propagation through several grains. Here, both transgranular and intergranular crack growth appears in this single long crack, as indicated by the yellow and red arrows, respectively. Notably, the transgranular crack tends to grow into coarse grains. In contrast, the intergranular crack tends to propagate along grain boundaries between fine grains or between fine and coarse grains.

Figure 2.11 shows a set of SEM images recorded from a fractured hydrogen-charged specimen. Figure 2.11a simultaneously indicates the fracture surface and cross-sectional image. Numerous voids are observed using secondary electron contrast (Fig. 2.11a and b). It is evident in the cross section that the voids are aligned preferentially along the tensile direction (Fig. 2.11b). As shown in the RD-IPF map (Fig. 2.11c), groups of voids exist at both grain boundaries and grain interiors, as indicated by the white and red dashed rectangles, respectively. The voids are present in all the plastically deformed regions on the cross section, and are particularly dense near the fracture surface. However, lattice distortion distribution, which is mainly attributed to the presence of geometrically necessary dislocations, shows a significant plastic deformation near the twin and grain boundaries as depicted by the Kernel average misorientation (KAM) as shown in Fig. 2.11d.

Figure 2.12a reveals the microstructure of the cross section that had been chemically etched, where spherical and long micro-voids can be seen on the etched cross section. The void morphology shown in Fig. 2.12b indicates that the long micro-void resulted from the

coalescence of the spherical micro-voids. Note again that the void coalescence occurred parallel to the tensile axis.

2.3.3 Fractographic analysis

Figure 2.13 displays the fracture surface of an uncharged specimen. Figure 2.13b shows that the fracture surface is covered with fine dimples and partially includes coarse dimples. Next to the specimen surface, a shear lip is observed, which appeared when the final failure occurred. As seen in Fig. 2.13c, the dominant feature of the fracture surface is the presence of fine dimples.

By contrast, Figure 2.14 demonstrates that brittle features appear on the fracture surface of a hydrogen-charged specimen. The brittle feature is a result of quasi-cleavage fracture, as indicated by the magnified image in Fig. 2.14c. The quasi-cleavage fracture region contains many step-like ridges. Quasi-cleavage is a commonly observed feature in hydrogen-induced fracture of high-Mn austenitic steels [53]. In addition, delamination cracks, as indicated by the white arrows in Fig. 2.14d, can be noted.

2.4 Discussion

The hydrogen embrittlement susceptibility depends on the strength level, hydrogen content and local microstructure. From the microstructural viewpoint, the phase/grain size distribution, crystallographic orientation, segregation and local elastic misfit near the grain boundary, etc. have been reported to affect the hydrogen-assisted cracking/propagation and associated hydrogen-induced property degradation.

2.4.1 Characteristics of the hydrogen-induced changes in crack path

The key features of hydrogen-assisted cracking are (1) microstructural crack initiation/propagation along the grain and twin boundaries and (2) delamination crack growth. Similar to previous studies, grain and twin boundary cracking was frequently observed, as this is a common feature of hydrogen embrittlement of TWIP steels. Specifically, grain and twin boundary cracking have been reported to stem from micro-stress concentration at the twin–twin intersections and at boundaries, where dislocation movement and twin growth impinge [15, 16]. The plastic strain localization assists hydrogen segregation and the associated cracking. In the present case, the twin–twin intersection/interception caused hydrogen-assisted crack initiation and growth, as shown in Fig. 2.8b.

It should be noted that deformation-twinning activity depends on the grain size. Specifically, grain refinement suppresses deformation twinning [15, 27]. Therefore, in the bimodal TWIP steel used in this study, the fine grain region mostly showed intergranular cracking (Fig. 2.9), and the coarse grain region showed transgranular cracking along the twin boundaries (Fig. 2.8). Therefore, the crack growth progressed via both intergranular and transgranular propagation (Fig. 2.10). Interestingly, the intergranular crack growth occurred preferentially along the grain boundaries between the fine and coarse grains, as shown in Fig. 2.9.

The crack growth that resulted in delamination stems from the void coalescence that formed along the tensile direction, as illustrated in Figs. 2.11 and 2.12. In general, micro-void formation requires plastic deformation; in other words, dislocation motion and subsequent dislocation accumulation are dominant. Since atomic hydrogen locally affects dislocation mobility, dislocation accumulation at a critical microstructural feature can occur more easily in hydrogen-charged steels. For instance, dislocation–twin interactions reduce

the coherency of twin boundaries, which induces steps at the atomic scale that act as hydrogen trap sites. Hydrogen accumulation at these steps causes micro-voids or cracks [53]. Another example is the interaction between hydrogen-localized slip and grain boundaries. The interaction causes elastic misfit and lattice defect accumulation, which induces micro-voids along the grain boundaries. In most cases of hydrogen-assisted void formation, local stress and plastic strain localization play a key role in the damage evolution mechanism. In this context, the relationship between grain size distribution and the stress/strain distribution needs to be discussed to understand the underlying mechanism of the crack-induced delamination growth.

A case in point is the effect of grain refinement on micro-stress concentration. It has been reported that the micro-stress concentration associated with dislocation pileup at grain boundaries in fine-grained specimens is much lower than that in coarse-grained ones[19]. Therefore, when micro-void growth occurred in the grain interior, it was mainly observed in the coarse grains, as shown in Fig. 2.11c. On the other hand, when micro-void growth occurred along grain boundaries, the grain boundaries between the fine and coarse grains acted as the preferential sites (Fig. 2.11c), which is similar to the observation of crack initiation shown in Fig. 2.9. This fact can be explained by the elastic misfit and associated plastic strain evolution in the vicinity of the grain boundaries between the fine and coarse grains.

2.4.2 Growth mechanism of hydrogen-assisted delamination cracks

In this section, the mechanism of void growth along the fine and coarse grains will be discussed along with the crack initiation issue to answer the question: Why did the void growth occur along the longitudinal direction (tensile direction) in the hydrogen-charged

specimens (Fig. 2.12). In particular, an important aspect in this context is the ductile behavior related to the growth of delamination cracks.

The proposed delamination crack growth process is shown schematically in Fig. 2.15. First, it is assumed that hydrogen assists the formation of micro-voids via dislocation-twin interaction or slip localization-grain boundary interaction as discussed in the previous section. As mentioned above, the micro-voids grow in the interior of the coarse grains and along the grain boundaries between the fine and coarse grains. This type of a hydrogen-related ductile failure mechanism causing nano- and micro-void formation has already been reported for high-Mn austenitic steels [11]. Dislocation slip localization is enhanced by hydrogen-enhanced localized plasticity (HELP) [54-58] (i.e. local material softening arising from hydrogen-enhanced dislocation mobility [58]), which promotes damage evolution along the slip planes or grain boundaries and other microstructural interfaces where dislocations impinge. In fact, it has been reported that based on the HELP mechanism the nucleation of nano-voids occurs as a result of the interactions between hydrogen and dislocations in the localized slip regions. The hydrogen-dislocation interaction occurs particularly at a low strain rate such as 10^{-5} s^{-1} selected for this study, because of their competitive motion. Furthermore, the hydrogen-decorated dislocation motion may assist segregation of hydrogen atoms at a given microstructural site, which accelerates hydrogen-assisted damage evolution. As a result, the coalescence of these voids, thus, can invoke crack initiation and propagation [59].

In the present study the most characteristic feature associated with hydrogen-assisted damage evolution is the micro-void growth along the tensile direction. This can be correlated with the bimodal grain distribution. Three factors can be identified that cause the micro-void growth along the tensile direction in the steel with the bimodal grain microstructure. Firstly, the fine grains have a higher strength than the coarse ones, which causes a difference in strain

along the direction perpendicular to the tensile direction. In other words, coarse grains with a lower strength tend to show a higher plastic elongation compared to the fine grains, which causes stress along the direction perpendicular to the tensile direction. To accommodate the stress along the vertical direction, crack or plastic strain evolves in the vicinity of the grain boundaries between fine and coarse grains aligned along the tensile direction. In particular, the HELP effect enhances the effect of the plastic strain localization for stress accommodation, which preferentially causes micro-voids to form in the vicinity of the boundary and align in the tensile direction (Fig. 2.15a). Secondly, the micro-voids are elongated along the tensile direction because stress triaxiality is high at side tips of the micro-voids (Fig. 2.15b).Thirdly, even in the tensile direction, the elongated defect has a mechanical driving force to propagate along the longitudinal direction [60]. Furthermore, the coalescence process may be assisted by hydrogen-enhanced decohesion [61]. Therefore, the micro-voids can coalesce along the tensile direction (Figs. 2.12 and 2.15c). As a result, growth/coalescence of hydrogen-assisted micro-voids results in the tensile direction in the hydrogen-charged specimen, as observed experimentally (Fig. 2.12). Subsequently, the micro-voids that had coalesced along the tensile direction are linked via the propagation of the main crack from the specimen surface (Fig. 2.15d). The linkage process of the delaminated voids would accelerate the propagation of the main crack. Consequently, final failure occurs, resulting in the fracture surface revealing the feature of the delamination crack growth (Figs. 2.14d and 2.15e).

In summary, the bimodal grain-structured TWIP steel showed a similar failure behavior compared to that reported for hydrogen-assisted crack growth in TWIP steels with homogenous grain sizes. The characteristic difference is the occurrence of a delamination-type crack growth mode. In this study, a possible mechanism for this type of hydrogen-induced damage and its contribution to overall crack growth is presented. A key point of this

fracture mode is the evolution of ductile damage along the grain boundaries between the fine and coarse grains, as discussed above.

2.5 Conclusions

Hydrogen embrittlement of a high-Mn fully austenitic TWIP steel with a bimodal grain size distribution was examined by tensile testing with in-situ electrochemical hydrogen charging. The occurrence of embrittlement in the bimodal grains can be explained by two main factors. Firstly, crack initiation/propagation along the grain and twin boundaries and second, delamination crack growth.

The micro-stress concentration and plastic strain localization at the twin–twin intersection/interception caused hydrogen assisted crack initiation and growth. Furthermore, deformation twinning played an important role in the intergranular and transgranular cracking. Intergranular cracks tended to grow along the grain boundaries between the fine and coarse grains, while, the transgranular cracks tended to propagate into the coarse grains.

The delamination observed on the fracture surface of the hydrogen-charged specimen was caused by void coalescence that nucleated along the tensile axes. The coalesced micro-voids elongated at the grain boundaries between the fine and coarse grains due to the elastic misfit and in the grain interior of the coarse grains because of the associated localization of stresses and strains. The increased susceptibility in the direction of void coalescence, i.e. along the tensile direction, can be explained by three main factors. Firstly, the difference in plastic strain localization in the coarse and fine grains; secondly, the presence of stress triaxiality at the side tips of the micro-voids; and, thirdly, the defect elongation propagation in the longitudinal direction.

2.6 References

[1] Sasaki T, Watanabe K, Nohara K, Ono Y, Kondo N, Sato S. Physical and Mechanical Properties of High Manganese Non-magnetic Steel and Its Application to Various Products for Commercial Use. Transactions of the Iron and Steel Institute of Japan. 1982;22:1010-20.

[2] Koyama M, Lee T, Lee CS, Tsuzaki K. Grain refinement effect on cryogenic tensile ductility in a Fe–Mn–C twinning-induced plasticity steel. Materials & Design. 2013;49:234-41.

[3] Koyama M, Sawaguchi T, Lee T, Lee CS, Tsuzaki K. Work hardening associated with ε-martensitic transformation, deformation twinning and dynamic strain aging in Fe–17Mn–0.6C and Fe–17Mn–0.8C TWIP steels. Materials Science and Engineering: A. 2011;528:7310-6.

[4] Glage A, Weigelt C, Räthel J, Biermann H. Fatigue behaviour of hot pressed austenitic TWIP steel and TWIP steel/Mg-PSZ composite materials. International Journal of Fatigue. 2014;65:9-17.

[5] Saleh AA, Pereloma EV, Clausen B, Brown DW, Tomé CN, Gazder AA. On the evolution and modelling of lattice strains during the cyclic loading of TWIP steel. Acta Materialia. 2013;61:5247-62.

[6] Lambers HG, Rüsing CJ, Niendorf T, Geissler D, Freudenberger J, Maier HJ. On the low-cycle fatigue response of pre-strained austenitic Fe61Mn24Ni6.5Cr8.5 alloy showing TWIP effect. International Journal of Fatigue. 2012;40:51-60.

[7] Habib K, Koyama M, Noguchi H. Impact of Mn–C couples on fatigue crack growth in austenitic steels: Is the attractive atomic interaction negative or positive? International Journal of Fatigue. 2017;99:1-12.

[8] Bal B, Gumus B, Gerstein G, Canadinc D, Maier HJ. On the micro-deformation mechanisms active in high-manganese austenitic steels under impact loading. Materials Science and Engineering: A. 2015;632:29-34.

[9] Gumus B, Bal B, Gerstein G, Canadinc D, Maier HJ, Guner F, et al. Twinning activities in high-Mn austenitic steels under high-velocity compressive loading. Materials Science and Engineering: A. 2015;648:104-12.

[10] Gumus B, Bal B, Gerstein G, Canadinc D, Maier HJ. Twinning activity in high-manganese austenitic steels under high velocity loading. Materials Science and Technology. 2016;32:463-5.

[11] Koyama M, Springer H, Merzlikin SV, Tsuzaki K, Akiyama E, Raabe D. Hydrogen embrittlement associated with strain localization in a precipitation-hardened Fe–Mn–Al–C light weight austenitic steel. International Journal of Hydrogen Energy. 2014;39:4634-46.

[12] Raabe D, Springer H, Gutierrez-Urrutia I, Roters F, Bausch M, Seol JB, et al. Alloy Design, Combinatorial Synthesis, and Microstructure–Property Relations for Low-Density Fe-Mn-Al-C Austenitic Steels. JOM. 2014;66:1845-56.

[13] Dieudonné T, Marchetti L, Wery M, Chêne J, Allely C, Cugy P, et al. Role of copper and aluminum additions on the hydrogen embrittlement susceptibility of austenitic Fe–Mn–C TWIP steels. Corrosion Science. 2014;82:218-26.

[14] De Cooman B, Chin K-g, Kim J. High Mn TWIP steels for automotive applications. New trends and developments in automotive system engineering: IntechOpen; 2011.

[15] Koyama M, Akiyama E, Lee Y-K, Raabe D, Tsuzaki K. Overview of hydrogen embrittlement in high-Mn steels. international journal of hydrogen energy. 2017;42:12706-23.

[16] Koyama M, Akiyama E, Tsuzaki K, Raabe D. Hydrogen-assisted failure in a twinning-induced plasticity steel studied under in situ hydrogen charging by electron channeling contrast imaging. Acta Materialia. 2013;61:4607-18.

[17] Yamabe J, Takakuwa O, Matsunaga H, Itoga H, Matsuoka S. Hydrogen diffusivity and tensile-ductility loss of solution-treated austenitic stainless steels with external and internal hydrogen. International Journal of Hydrogen Energy. 2017;42:13289-99.

[18] Saha R, Ueji R, Tsuji N. Fully recrystallized nanostructure fabricated without severe plastic deformation in high-Mn austenitic steel. Scripta Materialia. 2013;68:813-6.

[19] Bai Y, Momotani Y, Chen MC, Shibata A, Tsuji N. Effect of grain refinement on hydrogen embrittlement behaviors of high-Mn TWIP steel. Materials Science and Engineering: A. 2016;651:935-44.

[20] Calcagnotto M, Ponge D, Raabe D. Effect of grain refinement to 1μm on strength and toughness of dual-phase steels. Materials Science and Engineering: A. 2010;527:7832-40.

[21] Langdon TG. Twenty-five years of ultrafine-grained materials: Achieving exceptional properties through grain refinement. Acta Materialia. 2013;61:7035-59.

[22] Wang M, Akiyama E, Tsuzaki K. Effect of hydrogen on the fracture behavior of high strength steel during slow strain rate test. Corrosion Science. 2007;49:4081-97.

[23] Hardie D, Charles EA, Lopez AH. Hydrogen embrittlement of high strength pipeline steels. Corrosion Science. 2006;48:4378-85.

[24] Nie Y, Kimura Y, Inoue T, Yin F, Akiyama E, Tsuzaki K. Hydrogen Embrittlement of a 1500-MPa Tensile Strength Level Steel with an Ultrafine Elongated Grain Structure. Metallurgical and Materials Transactions A. 2012;43:1670-87.

[25] Kimura Y, Sakai Y, Hara T, Belyakov A, Tsuzaki K. Hydrogen induced delayed fracture of ultrafine grained 0.6% O steel with dispersed oxide particles. Scripta Materialia. 2003;49:1111-6.

[26] Park I-J, Lee S-m, Jeon H-h, Lee Y-K. The advantage of grain refinement in the hydrogen embrittlement of Fe–18Mn–0.6C twinning-induced plasticity steel. Corrosion Science. 2015;93:63-9.

[27] Zan N, Ding H, Guo X, Tang Z, Bleck W. Effects of grain size on hydrogen embrittlement in a Fe-22Mn-0.6C TWIP steel. International Journal of Hydrogen Energy. 2015;40:10687-96.

[28] Takasawa K, Ikeda R, Ishikawa N, Ishigaki R. Effects of grain size and dislocation density on the susceptibility to high-pressure hydrogen environment embrittlement of high-strength low-alloy steels. International Journal of Hydrogen Energy. 2012;37:2669-75.

[29] Oudriss A, Creus J, Bouhattate J, Conforto E, Berziou C, Savall C, et al. Grain size and grain-boundary effects on diffusion and trapping of hydrogen in pure nickel. Acta Materialia. 2012;60:6814-28.

[30] Allain S, Chateau JP, Bouaziz O. A physical model of the twinning-induced plasticity effect in a high manganese austenitic steel. Materials Science and Engineering: A. 2004;387–389:143-7.

[31] Saeed-Akbari A, Mosecker L, Schwedt A, Bleck W. Characterization and Prediction of Flow Behavior in High-Manganese Twinning Induced Plasticity Steels: Part I. Mechanism Maps and Work-Hardening Behavior. Metallurgical and Materials Transactions A. 2012;43:1688-704.

[32] Gutierrez-Urrutia I, Zaefferer S, Raabe D. The effect of grain size and grain orientation on deformation twinning in a Fe–22 wt.% Mn–0.6 wt.% C TWIP steel. Materials Science and Engineering: A. 2010;527:3552-60.

[33] Takasawa K, Wada Y, Ishigaki R, Kayano R. Effects of Grain Size on Hydrogen Environment Embrittlement of High Strength Low Alloy Steel in 45 MPa Gaseous Hydrogen. MATERIALS TRANSACTIONS. 2010;51:347-53.

[34] Oudriss A, Creus J, Bouhattate J, Savall C, Peraudeau B, Feaugas X. The diffusion and trapping of hydrogen along the grain boundaries in polycrystalline nickel. Scripta Materialia. 2012;66:37-40.

[35] Koyama M, Akiyama E, Sawaguchi T, Raabe D, Tsuzaki K. Hydrogen-induced cracking at grain and twin boundaries in an Fe–Mn–C austenitic steel. Scripta Materialia. 2012;66:459-62.

[36] Koyama M, Akiyama E, Tsuzaki K. Hydrogen-induced delayed fracture of a Fe–22Mn–0.6C steel pre-strained at different strain rates. Scripta Materialia. 2012;66:947-50.

[37] Akiyama E, Matsuoka S. Hydrogen Visualization in Steels Using Ag Decoration Method. Materials transactions. 2015;56:793-7.

[38] Ueji R, Tsuchida N, Terada D, Tsuji N, Tanaka Y, Takemura A, et al. Tensile properties and twinning behavior of high manganese austenitic steel with fine-grained structure. Scripta Materialia. 2008;59:963-6.

[39] Bouaziz O, Allain S, Scott CP, Cugy P, Barbier D. High manganese austenitic twinning induced plasticity steels: A review of the microstructure properties relationships. Current Opinion in Solid State and Materials Science. 2011;15:141-68.

[40] Oh-ishi K, Zhang HW, Ohkubo T, Hono K. Microstructure characterization of bulk nanocrystalline Fe–0.8C alloy produced by mechanical milling and spark plasma sintering. Materials Science and Engineering: A. 2007;456:20-7.

[41] Sitarama Raju K, Subramanya Sarma V, Kauffmann A, Hegedűs Z, Gubicza J, Peterlechner M, et al. High strength and ductile ultrafine-grained Cu–Ag alloy through bimodal grain size, dislocation density and solute distribution. Acta Materialia. 2013;61:228-38.

[42] Wang Y, Chen M, Zhou F, Ma E. High tensile ductility in a nanostructured metal. Nature. 2002;419:912-5.

[43] Fan GJ, Choo H, Liaw PK, Lavernia EJ. Plastic deformation and fracture of ultrafine-grained Al–Mg alloys with a bimodal grain size distribution. Acta Materialia. 2006;54:1759-66.

[44] Qiu H, Ito R, Hiraoka K. Role of grain size on the strength and ductile–brittle transition temperature in the dual-sized ferrite region of the heat-affected zone of ultra-fine grained steel. Materials Science and Engineering: A. 2006;435-436:648-52.

[45] Edalati K, Furuta T, Daio T, Kuramoto S, Horita Z. High strength and high uniform ductility in a severely deformed iron alloy by lattice softening and multimodal-structure formation. Materials Research Letters. 2015;3:197-202.

[46] Sabzi HE, Zarei Hanzaki A, Abedi HR, Soltani R, Mateo A, Roa JJ. The effects of bimodal grain size distributions on the work hardening behavior of a TRansformation-TWinning induced plasticity steel. Materials Science and Engineering: A. 2016;678:23-32.

[47] Jin H, Lloyd DJ. Effect of a duplex grain size on the tensile ductility of an ultra-fine grained Al–Mg alloy, AA5754, produced by asymmetric rolling and annealing. Scripta Materialia. 2004;50:1319-23.

[48] Han BO, Lavernia EJ, Lee Z, Nutt S, Witkin D. Deformation behavior of bimodal nanostructured 5083 Al alloys. Metallurgical and Materials Transactions A. 2005;36:957-65.

[49] Dini G, Najafizadeh A, Ueji R, Monir-Vaghefi S. Tensile deformation behavior of high manganese austenitic steel: The role of grain size. Materials & Design. 2010;31:3395-402.

[50] Koyama M, Akiyama E, Tsuzaki K. Hydrogen embrittlement in a Fe–Mn–C ternary twinning-induced plasticity steel. Corrosion Science. 2012;54:1-4.

[51] Koyama M, Akiyama E, Tsuzaki K. Hydrogen embrittlement in Al-added twinning-induced plasticity steels evaluated by tensile tests during hydrogen charging. ISIJ international. 2012;52:2283-7.

[52] Liu Q, Irwanto B, Atrens A. Influence of hydrogen on the mechanical properties of some medium-strength Ni–Cr–Mo steels. Materials Science and Engineering: A. 2014;617:200-10.

[53] Bal B, Koyama M, Gerstein G, Maier H, Tsuzaki K. Effect of strain rate on hydrogen embrittlement susceptibility of twinning-induced plasticity steel pre-charged with high-pressure hydrogen gas. international journal of hydrogen energy. 2016;41:15362-72.

[54] Wang S, Hashimoto N, Wang Y, Ohnuki S. Activation volume and density of mobile dislocations in hydrogen-charged iron. Acta Materialia. 2013;61:4734-42.

[55] Barnoush A, Vehoff H. Recent developments in the study of hydrogen embrittlement: Hydrogen effect on dislocation nucleation. Acta Materialia. 2010;58:5274-85.

[56] Sofronis P, Liang Y, Aravas N. Hydrogen induced shear localization of the plastic flow in metals and alloys. European Journal of Mechanics - A/Solids. 2001;20:857-72.

[57] von Pezold J, Lymperakis L, Neugebeauer J. Hydrogen-enhanced local plasticity at dilute bulk H concentrations: The role of H–H interactions and the formation of local hydrides. Acta Materialia. 2011;59:2969-80.

[58] Birnbaum HK, Sofronis P. Hydrogen-enhanced localized plasticity—a mechanism for hydrogen-related fracture. Materials Science and Engineering: A. 1994;176:191-202.

[59] Neeraj T, Srinivasan R, Li J. Hydrogen embrittlement of ferritic steels: Observations on deformation microstructure, nanoscale dimples and failure by nanovoiding. Acta Materialia. 2012;60:5160-71.

[60] Sasaki D, Koyama M, Noguchi H. Factors affecting hydrogen-assisted cracking in a commercial tempered martensitic steel: Mn segregation, MnS, and the stress state around abnormal cracks. Materials Science and Engineering: A. 2015;640:72-81.

[61] Koyama M, Tasan CC, Akiyama E, Tsuzaki K, Raabe D. Hydrogen-assisted decohesion and localized plasticity in dual-phase steel. Acta Materialia. 2014;70:174-87.

2.7 Figures

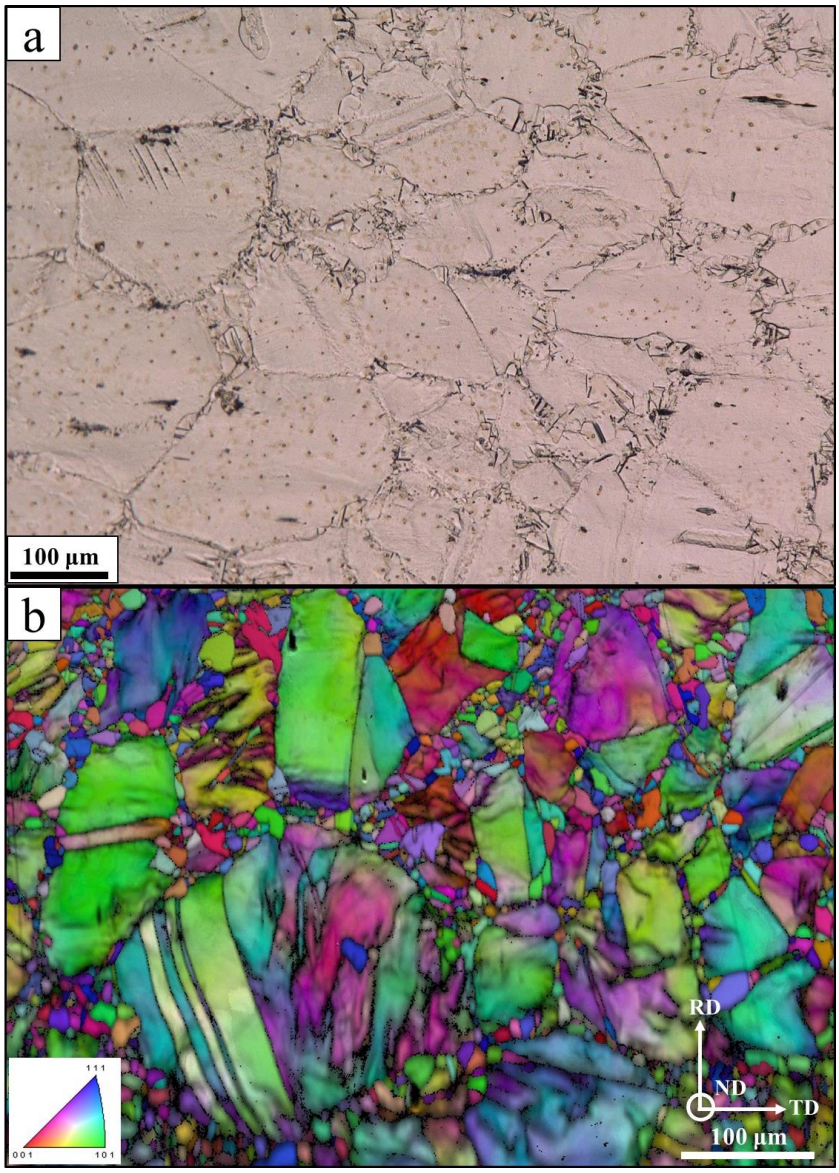

Fig. 2.1. (a) Optical of the etched specimen (b) RD-IPF, of micrograph of the initial microstructure showing the bimodal microstructure featuring fine grains along the boundaries of the coarse ones.

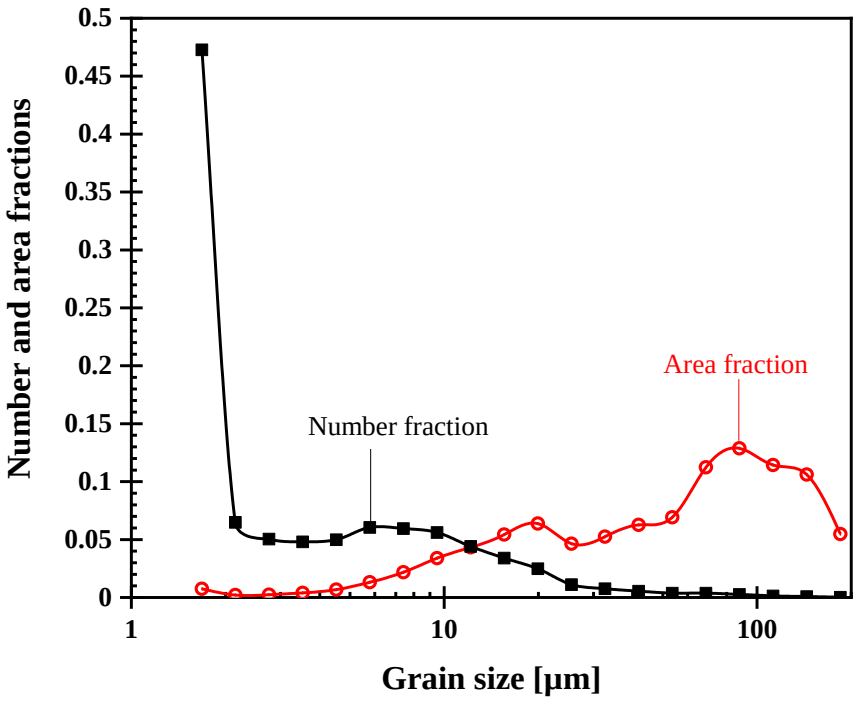

Fig. 2.2. Fig. 2.2 The grain size distribution of fine and coarse grains.

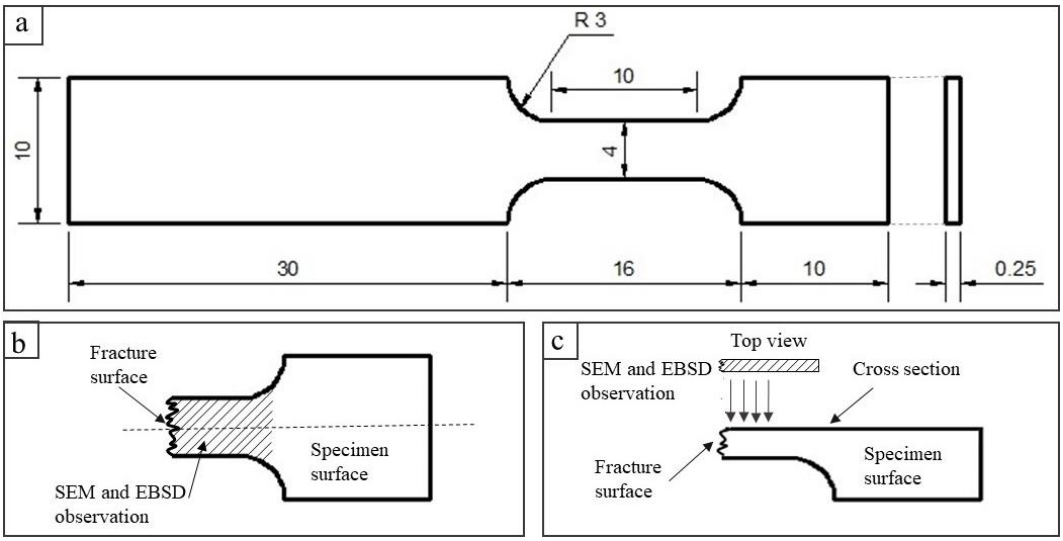

Fig. 2.3. (a) Geometry of the tensile specimens; (b) and (c) areas analyzed by scanning electron microscopy and electron backscatter diffraction observation.

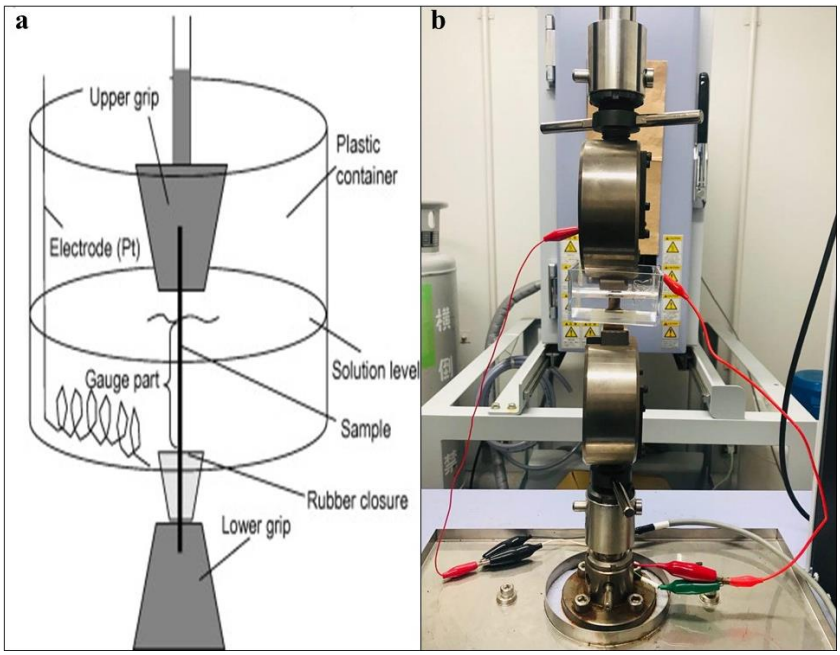

Fig. 2.4. (a) schematic [50] and (b) image of installation of tools into a cell for hydrogen-charged experiments.

\

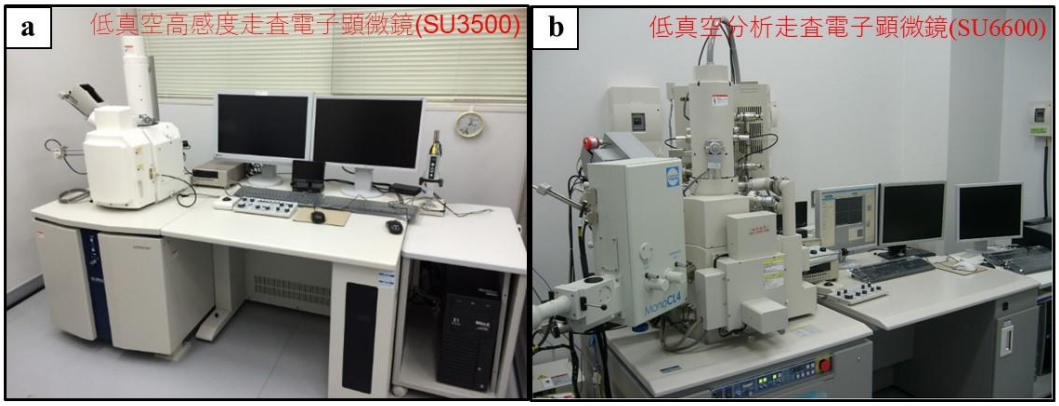

Fig. 2.5. Image of (a) SEM and (b) EBSD instruments at center of advanced instrumental analysis, Kyushu university employed in this research.

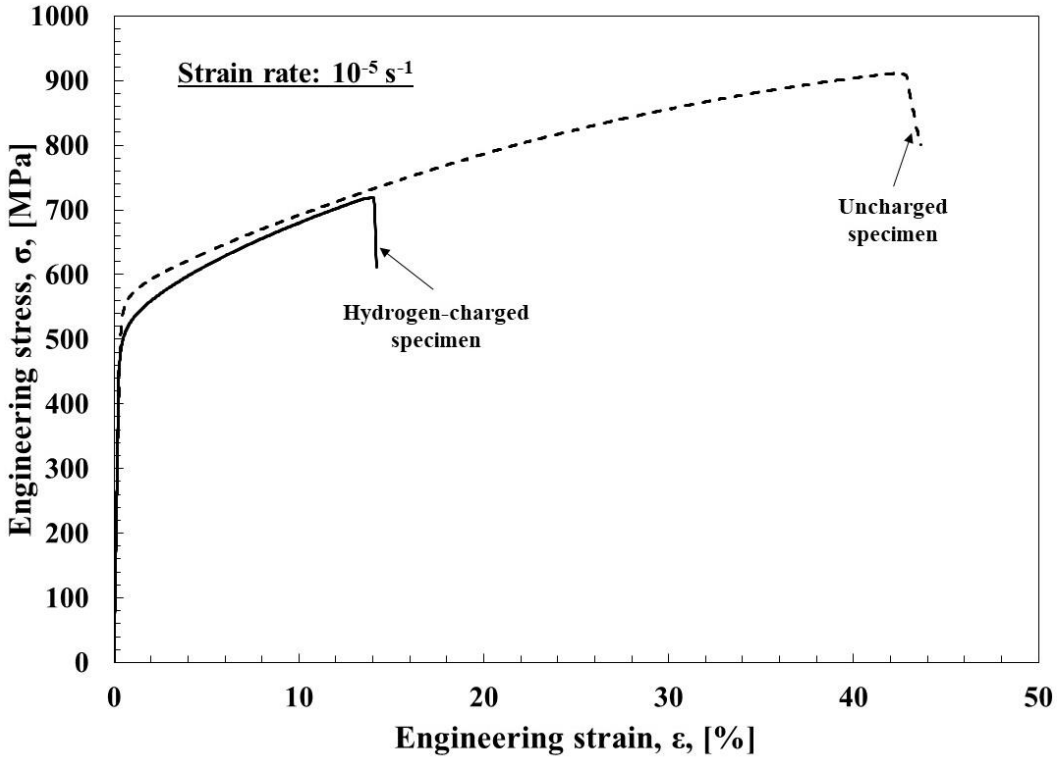

Fig. 2.6. Engineering stress–strain curves of hydrogen-charged and uncharged specimens.

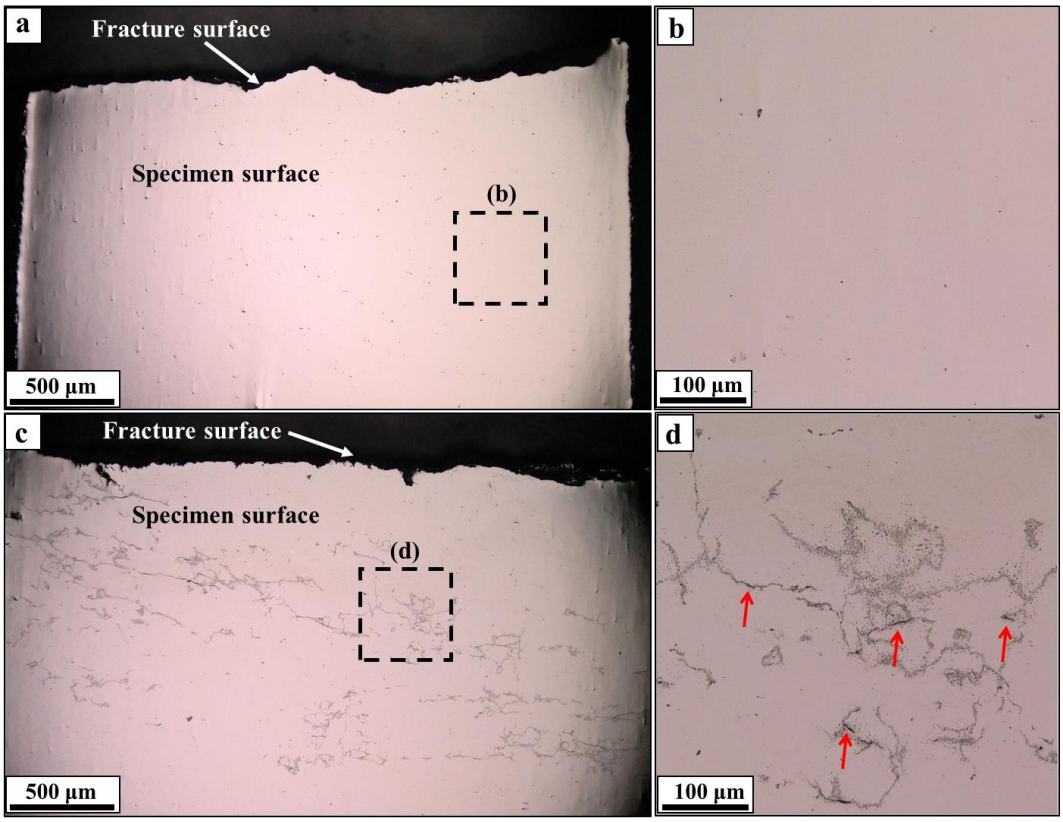

Fig. 2.7. Optical micrographs of the surfaces of the fractured specimens: (a) Uncharged specimen, (b) a magnified image of the section marked by the dashed rectangle in (a), (c) hydrogen-charged specimen, and (d) a magnified image of the section marked by the dashed rectangle in (c); red arrows indicate the sub-cracks in the hydrogen-charged specimen.

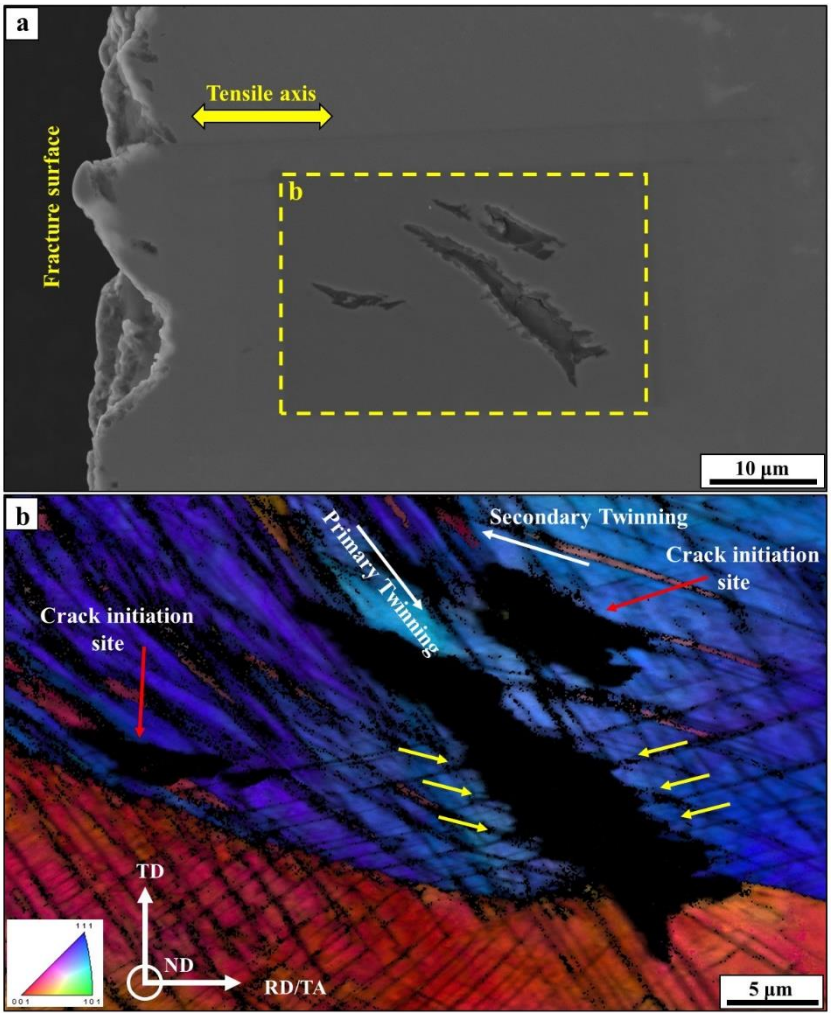

Fig. 2.8. (a) SEM image and (b) corresponding RD-IPF map of a sub-crack on the surface of the hydrogen-charged specimen in the vicinity of the fracture surface, the RD-IPF map is superimposed by the image quality (IQ) contrast.

Fig. 2.9. RD-IPF map of hydrogen-assisted intergranular cracking. The RD-IPF map is superimposed with the IQ contrast.

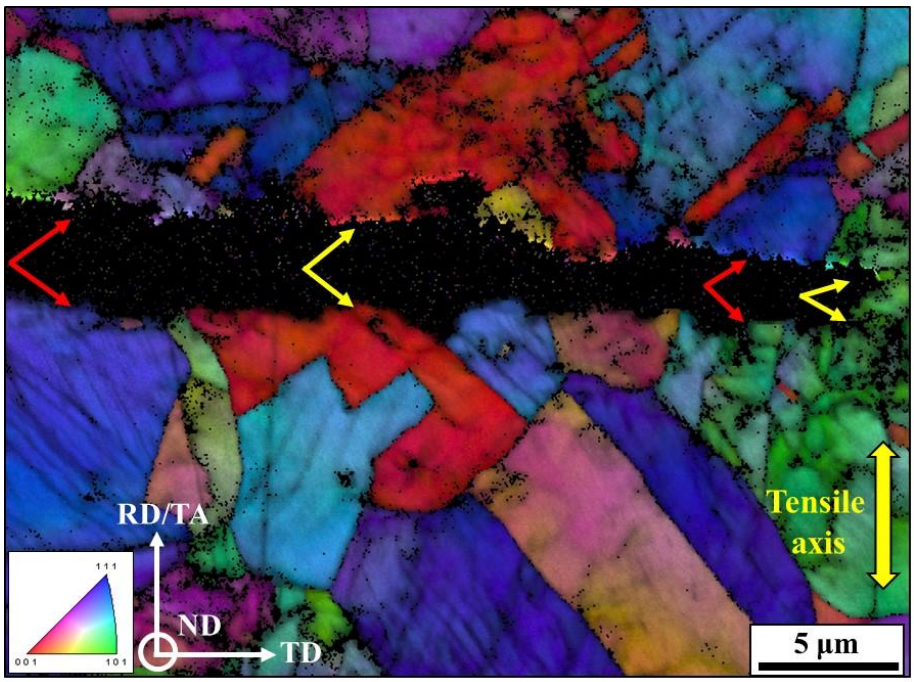

Fig. 2.10. RD-IPF map of a single crack through several grains on the surface of the hydrogen-charged specimen. The RD-IPF map is superimposed with the IQ contrast; red and yellow arrows mark intergranular and transgranular propagation events, respectively

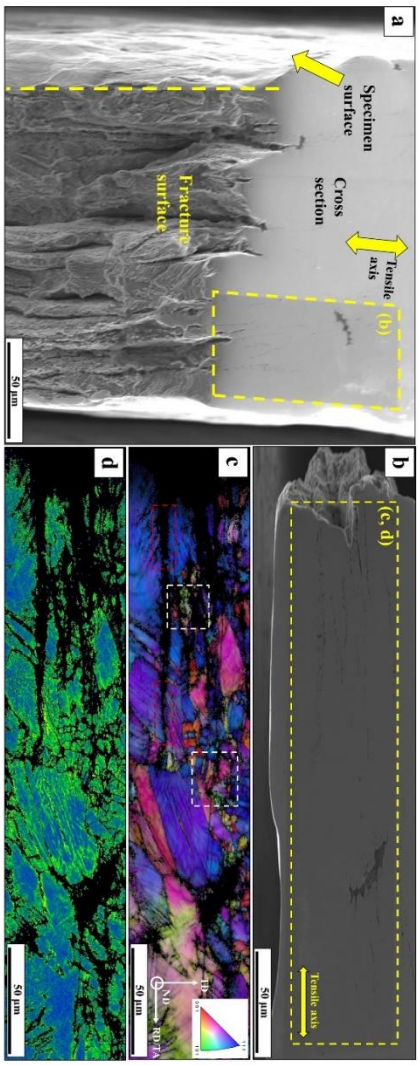

Fig. 2.11. SEM images from a hydrogen-charged specimen: (a) the intersection of the cross section with the fracture and specimen surfaces, (b) the cross section showing the presence of a void density along the tensile direction, (c) the corresponding RD-IPF orientation map of the cross section superimposed with the IQ contrast and (d) the corresponding KAM map.

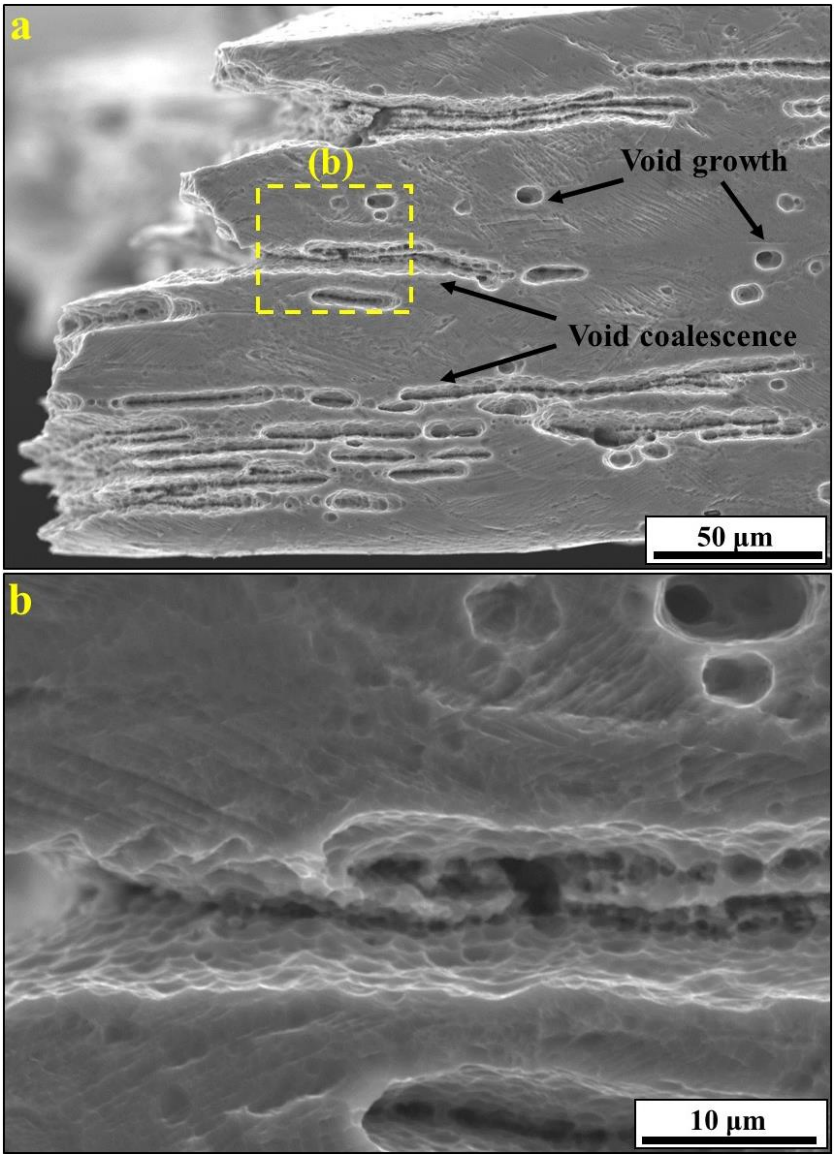

Fig. 2.12. SEM images of (a) the microstructure of the cross section of a hydrogen-charged specimen, which was etched with 3% nital. and (b) higher magnification detail of the marked region in (a)

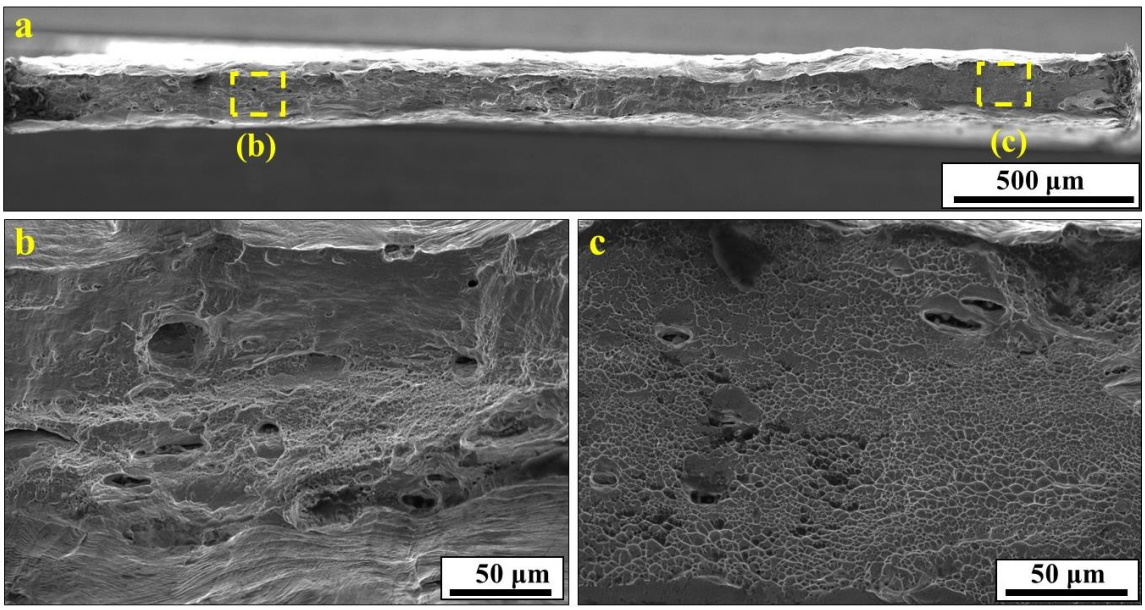

Fig. 2.13. SEM images showing (a) an overview of the entire fracture surface of an uncharged specimen with (b), and (c) showing high magnification details of the areas highlighted in (a).

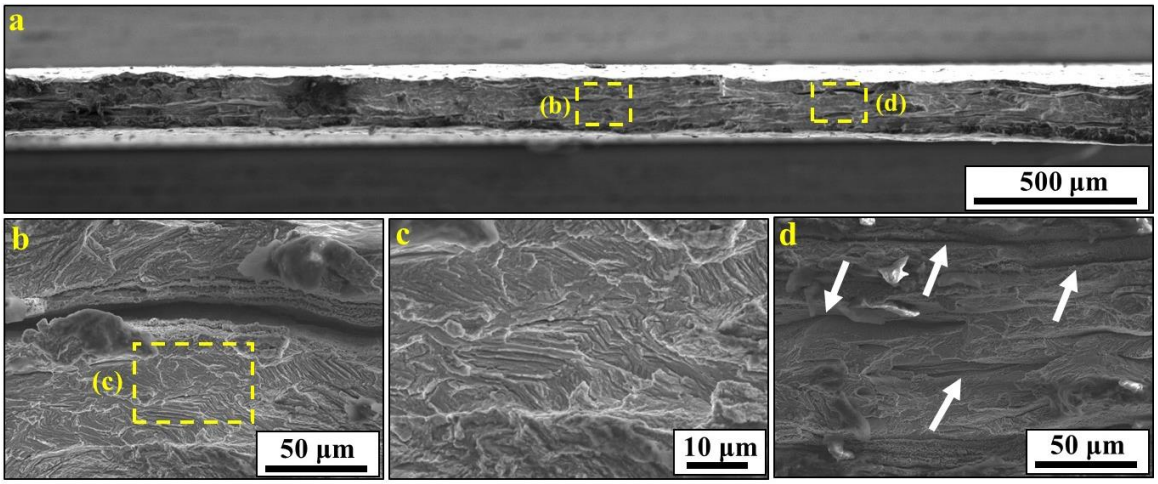

Fig. 2.14. (a) SEM images of the entire fracture surface of a hydrogen-charged specimen; (b) and (c) show quasi-cleavage features on the fracture surface at increasingly higher magnification and (d) demonstrates delamination crack features on the fracture surface by white arrows in the area marked in (a).

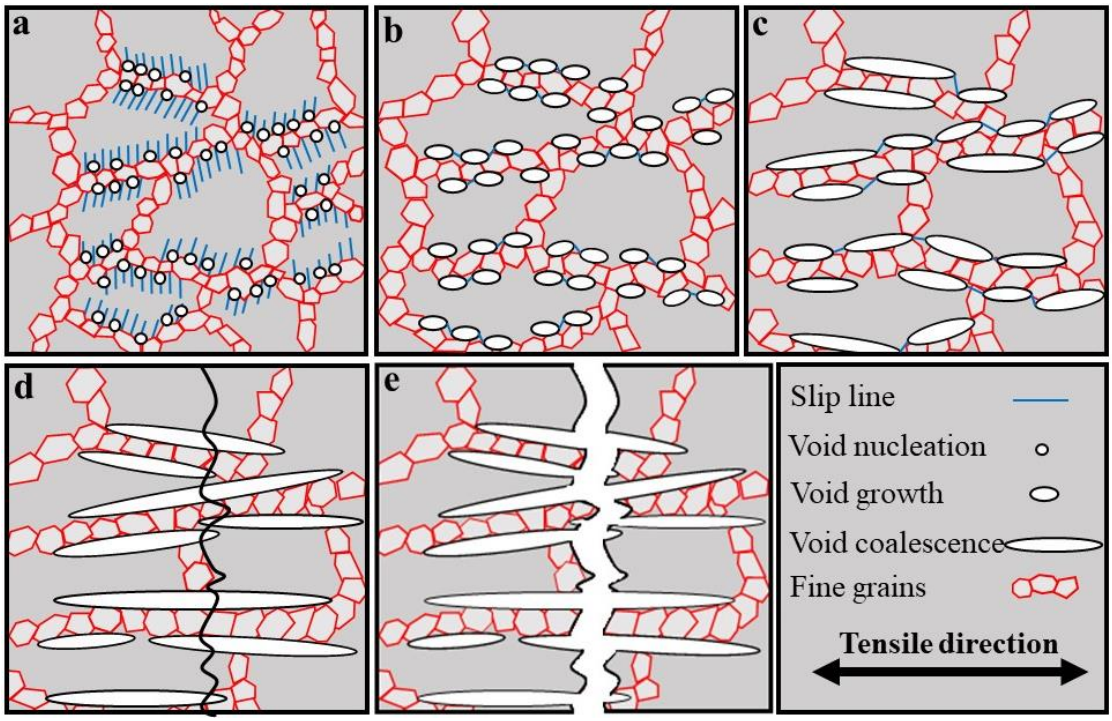

Fig. 2.15. Schematics demonstrating void nucleation, growth, and coalescence along the tensile direction, followed by final failure resulting from delamination cracking for hydrogen-charged TWIP steel with bimodal grain size.

CHAPTER 3. Hydrogen-assisted crack propagation in a pre-strained twinning-induced plasticity steel: from initiation at a small defect to failure

3.1 Introduction

As well recognized, stable austenitic steels show superior hydrogen embrittlement resistance [1-3]. Even when hydrogen-induced mechanical degradation appears, the failure occurs after significant plastic deformation [4, 5]. More specifically, even if crack initiation occurs in an early deformation stage, most of the cracks blunt and stop growing once when the crack size [6-8], i.e., microstructural damage arrest. Therefore, a risk of hydrogen-induced fracture in solution-treated austenitic steels is quite low compared to martensitic steels.

Nevertheless, hydrogen embrittlement problems in austenitic steels have been concerned as an important issue. This is perhaps because of pre-strain effects. In fact, plastic strain effect in highly deformable steels plays an important role on failure even without hydrogen. In particular, formation and growth of crack/void stem from accumulations of lattice defects such as vacancy [9, 10], dislocation [11, 12], and twin [13, 14] that reduce stress accommodation capability and create a microstructural crack growth path. Then, the plasticity-induced damage can co-act with hydrogen effects [15]. Since the plasticity-induced damage has been introduced during forming process of structural components particularly in room temperature, we must recognize that some of the plastically deformed austenitic steel components contain a potential risk associated with deterioration of small crack arrest property. In addition, cold/warm pre-deformation has been performed in austenitic steel to increase yield strength, which is another route that introduces plasticity-induced damage. Therefore, to understand hydrogen embrittlement resistance of very ductile material such as austenitic steels, we must note an effect of pre-plastic deformation on hydrogen-assisted crack propagation.

High-Mn twinning-induced plasticity (TWIP) steels are typical examples of austenitic steels that show high strength but also show hydrogen embrittlement after a significant plastic deformation [16, 17]. Moreover, this type of steels shows hydrogen-induced delayed failure when the structural components are severely plastically deformed [18, 19]. With this background, we here attempt to examine hydrogen-assisted crack propagation behavior of a plastically pre-deformed TWIP steel in terms of crack propagation rate and associated

microstructure evolution. Moreover, to investigate effects of stress concentration factor, two different artificial defect sizes were prepared. Hence, the purpose of the present study is to understand the behavior of hydrogen-assisted crack propagation in a TWIP steel by presence of micro-defect as a stress concentration under hydrogen charging.

3.2 Experimental procedure

In this chapter, received material is a warm-rolled Fe-15Mn-2.5Si-2.5Al-0.7C (wt.%) fully austenitic TWIP steel [20], same as previous chapter. The microstructure of the as-received condition is a bimodal grain size microstructure which shown in Figs. 2.1 and 2.2. The tensile specimens with gauge dimensions of 4 mm in width, 0.3 mm in thickness and 10 mm in length were cut by electrical discharge machining (EDM). The thickness of the specimens was reduced by mechanical grinding after EDM (Fig. 2.3a).

As mentioned in the introduction part, hydrogen-assisted crack propagation occurs only after significant plastic deformation. To investigate crack propagation after the plastic deformation, the specimens were first pre-deformed by 30% tensile strain at an initial strain rate of 10^{-5} s^{-1}. The surface of the specimens was mechanically polished with a mirror finish condition. Then, two types of artificial small stress concentration source were introduced by micro-drilling technique in a central part of the gauge part. A micro drill hole (1DH) with a diameter of 300 μm for both hydrogen-charged and uncharged specimens and three-drill holes (3DH) following each other in the same centerline perpendicular to the tensile direction with a diameter of 300 μm for each hole for another hydrogen-charged specimen. The final configuration of the specimens before the crack propagation observation is illustrated in Fig. 3.1.

Tensile tests with the pre-strain and micro-drill hole were conducted with and without hydrogen charging at a cross-head speed of 10^{-4} mm/s at temperature of 295 K. The crack propagation was observed by in situ optical microscopy. Hydrogen was electrochemically introduced in a 3% NaCl aqueous solution containing 3 g/L of NH_4SCN at a current density of 30 A/m^2 under the tensile tests. A platinum wire was employed as a counter-electrode. We have successfully observed the crack growth under loading for the case with in situ hydrogen charging. The in situ crack growth observation was carried out with an optical microscope with a focal length of 10 cm. Optical images were taken at each 30 s up to the end of the test.

Fracture surfaces were observed by scanning electron microscopy (SEM) at an accelerating voltage of 15 kV. In addition, the SEM was used for secondary electron imaging and EBSD measurements to observe cracks and microstructure near fracture surfaces of the hydrogen-charged specimens. The specimens for the microstructure observations were mechanically polished using a colloidal silica with a particle size of 60 nm. The EBSD measurements were conducted at an acceleration voltage of 20 kV with a beam step size of 100 nm.

3.3 Results

3.3.1 Hydrogen effects on mechanical response

Figure 3.2 shows engineering stress–displacement diagrams for the 30% pre-strained specimens. The engineering stress was defined as:

$$\sigma_e = \frac{P}{A_0} \tag{1}$$

where P and A_0 are applied load and initial cross-sectional area, respectively. The uncharged 1DH specimen showed failure at a displacement of 0.47 mm (dashed line). The hydrogen charging caused a loss of ~15% of the overall displacement (1DH: black solid line). Accordingly, the ultimate tensile strength (UTS) was also decreased from 1140 MPa to 1020 MPa by hydrogen charging. The increase in drill hole size, namely 3DH specimen, showed further earlier fracture compared with the hydrogen-charged 3DH specimen (red line).

3.3.2 Crack propagation behavior in the hydrogen-charged specimen

Figure 3.3 shows a set of optical images taken by the in situ optical microscopy under tensile testing in the hydrogen-charged 1DH specimen. After plastic zone evolution near the drill hole, cracks were initiated from both sides of the micro-hole (Fig. 3.3(b)), and gradually grew perpendicular to the tensile axis until fracture (Figs. 3.3(c-f)). The crack length measured from the in situ images was plotted against time and engineering stress plotted against crack length as shown in Fig. 3.4a and 3.4b, respectively. Here, the crack length was defined as projected crack length including the initial drill hole/s size. The crack propagation can be divided to two stages of low and high crack propagation rate. After crack initiation, rate of crack propagation sharply increased until failure, but it progresses with gradual decrease in engineering stress, which indicates that fracture mode is not completely brittle and looks like quasi-brittle fracture.

Figure 3.5 shows true net sectional stress vs total crack length in hydrogen-charged specimens. The true net sectional stress was defined as:

$$\sigma_F = \frac{P}{A_f} \quad (2)$$

where P and A_f are applied load and local cross-sectional area, respectively. Black and red lines indicate results of 1DH and 3DH specimens, respectively. This stress is reduced gradually after maximum value in 3DH specimen, while, it is an almost plateau by increasing the crack length in 1DH specimen. The results illustare that apparent stress level in 1DH specimen is higher than that in 3DH specimen when compared at the same crack length. The difference in the stress level between 1DH and 3DH specimens increased after the maximun value of 3DH sapecimen, which corresponds to the second stage in Fig. 3.4.

Figure 3.6a shows overall microstructure distribution of hydrogen-charged 1DH specimen after failure. Owing to the presence of the micro-hole (stress concentration source), heterogeneous distribution of deformation microstructures such as twins was observed, as clearly seen in Figs. 3.6b and 3.6c. Specifically, the twin density at the region far from the micro-hole along the tensile direction is lower than that in the vicinity of the fracture surface. It should be noted that there were only a few micro-cracks on the specimen surface after fracture unlike a case of the smooth TWIP steel plate where numerous subcracks were observed after fracture with hydrogen [20].

Figure 3.7 shows an SEM image and the corresponding RD-IPF map near the fracture surface of 1DH specimen. Figure 3.7a exhibits a few sub-cracks initiated from the micro-hole. Additionally, the RD-IPF map in Fig. 3.7b illustrates that a sub-crack formed from the micro-hole, propagated in the grain interior, and finally was terminated at the grain boundary. In addition, the plate-like microstructure with different orientation from the matrix or with low image quality in Fig. 7.b indicates formation of deformation twins within grain interior. 3DH specimen with hydrogen also showed transgranular crack propagation and formation of deformation twins as shown in the set of Fig. 3.8.

Figure 3.9 shows another example of an SEM image near the fracture surface of hydrogen-charged 3DH specimen. This image demonstrates subcrack initiation in front of the subcrack tip. Figure 3.10 exhibits a set of SEM and EBSD images taken around the fracture surface in 1DH and 3DH specimens. RD-IPF maps shown in Figs. 3.10a_2 and b_2 display a considerable amount of lattice distortion associated with plastic deformation involving an effect of deformation twins [21, 22]. However, lattice distortion distribution,

which is mainly attributed to the presence of geometrically necessary dislocations, did not show a significant difference between 1DH and 3DH specimens with hydrogen, as depicted by the Kernel average misorientation (KAM) [23, 24] and grain reference orientation deviation (GROD) maps (Figs. 3.10a_3 and b_3 and Fig. 3.10a_4 and b_4, respectively.). This is perhaps due to an effect of the large plastic pre-strain.

3.3.3 Fractographic analysis

Figure 3.11 displays the fracture surface of 1DH specimen without hydrogen charging. The uncharged specimen exhibits typical ductile fracture surface which is covered by fine dimples and partially includes coarse ones (Fig. 3.11b). In addition, the fracture surface shows some secondary fracture along the rolling direction as indicated by arrows in a magnified image in Fig. 3.11c. This splitting phenomenon, sometimes referred to as delamination, is commonly observed in hot rolled high strength steels [25, 26] or hydrogen-charged specimen with the same TWIP steel [20]. In this case, the appearance of delamination might be caused by the presence of stress triaxiality at the micro drill hole.

Figures 3.12 and 3.13 show the fracture surfaces of hydrogen-charged 1DH and 3DH specimens. The entire and magnified images of fracture surfaces exhibit quasi-cleavage feature containing many step-like ridge [27, 28] (marked by white arrows in Figs. 3.12b and 3.13b). In addition, higher magnification SEM micrograph (Fig. 3.12c and 3.13c) reveals that uncountable dimples are distributed along quasi-cleavage feature. This can be explained by the hydrostatic stress condition that stress level is very high and plastic deformation due to the twin planes.

3.4 Discussion

First note that the introduction of the through hole altered the failure behavior. Specifically, in the smooth specimen of hydrogen-charged bimodal TWIP steel, the failure occurs via intergranular crack initiation on the specimen surface and in the specimen interior and subsequent coalescence of the cracks [20]. In contrast, the present experiment demonstrated that the crack initiated from the drill hole, and propagated perpendicular to the tensile direction as shown in Fig. 3.3, which did not contain intergranular feature as shown in Figs. 3.12 and 3.13.

In terms of crack propagation, the growth progressed with increasing displacement step by step, namely, stable crack propagation occurred in the hydrogen-assisted failure. The crack was extended within the plastic zone in front of the notch and head of an advancing crack tip in the hydrogen-charged specimen (Fig. 3.3) which is one of the primary factors that causes stable crack growth in sufficiently ductile materials [29].

Results in Fig. 3.4 indicate that crack goes through three stages of behavior under displacement control monotonic loading until failure: (1) a period of no crack growth, (2) a period of stable crack growth with low rate and (3) stable crack growth with high rate. The hydrogen-assisted crack growth and the effect of different notch sizes in the two stages of cracking are explained in the following sections.

3.4.1 First stage of crack growth

In the early crack growth regime (Fig. 3.4), which is referred to as first stage, the crack in 3DH specimen grew more rapidly than that in 1DH specimen (3DH: 0.5 μm/s and 1DH: 0.4 μm/s). The initial defect size dependence is reasonable, because the crack with the longer initial defect causes higher stress concentration at the crack tip. The stress accommodation at the crack tip causes large plastic straining, which results in a crack initiation in front of the main crack when the plastic strain reaches a critical value for cracking event as observed in Fig. 3.9. The cracking event preferentially occurred in grain interior, irrespective of the drill hole size, as shown in Figs. 3.7b and 3.8b. More specifically, the transgranular cracking in TWIP steels, have been reported to occur along twin boundaries or coalescence of cracks that are formed at twin-twin intersections [14, 20, 30]. Coalescence of the cracks causes crack growth, which results in quasi-cleavage fracture surface as shown in Figs. 3.12 and 3.13. In this context, with the conventional knowledge [31-34], the plastic strain plays four roles on the crack growth: (1) work hardening for increasing local stress that causes the twin boundary cracking, (2) increasing twin density to increase cracking site density, (3) defect formation on twin boundaries [35, 36], and (4) hydrogen transport to twin boundaries [37, 38]. The high twin density and highly deformed twin plates were actually observed in Figs. 3.6 and 3.7b. In addition, quasi-cleavage fracture surface with step-like ridges, which has been recognized to correspond to twin cracking, was observed as shown in Figs. 3.12(b) and 3.13(b). These four factors are the reasons why the stress-accommodation-induced plastic straining at the crack tip is important and why the crack did not propagate to failure

immediately in the first stage. Obviously, the increases in yield strength and the initial twin density by pre-straining accelerates the transgranular crack growth, which thereby enhances the effect of drill hole size effects in the first stage. After this apparent stress/strain-controlled, the initial defect size dependence of the crack growth behavior changed significantly in the second stage, as discussed in the next section.

3.4.2 Second crack growth stage

In contrast to the first stage, the second stage crack growth in 1DH specimen was almost comparable to that in 3DH one. Here we must note two considerations in the second stage. First, the fractographic feature did not significantly change with increasing crack length as depicted in Figs. 3.12(c) and 3.13(c). Hence, cracking mechanism did not change by increasing crack length. Second, the apparent stress level in 1DH is always significantly higher than that in 3DH specimen when compared at an identical crack length as shown in Fig. 3.5. For instance, the true net sectional stress of 1DH specimen was approximately 1.5 times as high as that of 3DH one at the total crack length of 1.4 mm. These facts indicate that the initial defect size dependence of the crack growth cannot be explained by only apparent stress level at the crack tip unlike the first stage crack growth.

To explain the crack growth behavior in the second stage, we would need to consider “extrinsic factor”. Conventionally, ductile crack growth has been discussed with multiple factors that are classified into two groups: Intrinsic factor and extrinsic factor [39, 40]. Intrinsic factor means resistance to crack tip deformation that was mainly discussed for the first stage. On the other hand, the extrinsic factor is crack-tip shielding mechanisms, which act primarily behind the crack tip to retard crack growth. By increasing the advancing crack length, extrinsic factor effects become more significant. The difference between apparent stress in an identical crack length with same crack growth rate can be explained simultaneously by the intrinsic and extrinsic factors. This reason is assumed in the plastic zones on crack flanks act behind the crack tip primarily experienced at the crack tip to effectively reduce the crack-driving force. Trace of this effect must appear in dislocation microstructure on the fracture surface. However, any significant difference in microstructural feature was not observed between the fractured 1DH and 3DH specimens with hydrogen as shown in Fig. 3.10, because the large amount of pre-strain smeared out the trace of the extrinsic factor. Therefore, finding a microstructure characterization-based

method to clarify significance of the extrinsic factor in highly pre-strained materials will be required in future.

It is also noteworthy that the factor affecting the hydrogen-assisted cracking are not specific features of the bimodal microstructure. The transgranular crack growth path in the first stage was grain interior microstructure such as twins, which has been observed in various solution-treated TWIP steels charged with hydrogen [4, 16, 41]. On one hand, the extrinsic factor, which was assumed to occur in the second stage, is dependent on macroscopic mechanical parameters such as yield strength and work hardening rate. Furthermore, hydrogen kinetic effects also can affect both the first and second stages. However, these factors can be analyzed even without considering specialty of the bimodal feature. In other words, the present results are regarded as a general feature of hydrogen-assisted crack propagation in very ductile, slightly hydrogen susceptible steels, i.e. TWIP steels.

3.5 Conclusions

In the present work, the crack propagation behavior of the pre-deformed TWIP steel under electrochemical hydrogen charging was investigated. Hydrogen-assisted crack growth occurred via a quasi-cleavage feature, and the crack growth rate increased with increasing drill hole size when the crack length was small. The stress accommodation at the crack tip caused large plastic straining, resulting in work hardening and increasing twin density. These plasticity-related factors cause a crack formation in front of the main crack tip. The crack initiation and subsequent coalescence are the crack growth process, accordingly, the hydrogen-assisted crack growth mechanism is discontinuous, which involves step-like ridges and local formation of dimples on the fracture surface. A significant pre-plastic deformation accelerates a formation of the plasticity-induced precursor of the crack, which is considered to assist transgranular crack propagation.

3.6 References

[1] Kasahara S, Nakata K, Shimanuki S, Ikeda S, Kanno M. Structural member having superior resistance to neutron irradiation embrittlement, austenitic steel for use in same, and use thereof. Google Patents; 1996.

[2] Whiteman M, Troiano A. Hydrogen embrittlement of austenitic stainless steel. Corrosion. 1965;21:53-6.

[3] Oda Y, Noguchi H. Observation of hydrogen effects on fatigue crack growth behaviour in an 18Cr-8Ni austenitic stainless steel. International Journal of Fracture. 2005;132:99-113.

[4] Koyama M, Akiyama E, Tsuzaki K, Raabe D. Hydrogen-assisted failure in a twinning-induced plasticity steel studied under in situ hydrogen charging by electron channeling contrast imaging. Acta Materialia. 2013;61:4607-18.

[5] Michler T, Naumann J. Hydrogen embrittlement of Cr-Mn-N-austenitic stainless steels. International Journal of Hydrogen Energy. 2010;35:1485-92.

[6] Zhou Q, Qian L, Tan J, Meng J, Zhang F. Inconsistent effects of mechanical stability of retained austenite on ductility and toughness of transformation-induced plasticity steels. Materials Science and Engineering: A. 2013;578:370-6.

[7] Koyama M, Tasan CC, Akiyama E, Tsuzaki K, Raabe D. Hydrogen-assisted decohesion and localized plasticity in dual-phase steel. Acta Materialia. 2014;70:174-87.

[8] Tuğluca IB, Koyama M, Bal B, Canadinc D, Akiyama E, Tsuzaki K. High-concentration carbon assists plasticity-driven hydrogen embrittlement in a Fe-high Mn steel with a relatively high stacking fault energy. Materials Science and Engineering: A. 2018;717:78-84.

[9] Furukimi O, Kiattisaksri C, Takeda Y, Aramaki M, Oue S, Munetoh S, et al. Void nucleation behavior of single-crystal high-purity iron specimens subjected to tensile deformation. Materials Science and Engineering: A. 2017;701:221-5.

[10] Yu J, Kim J. Effects of residual S on Kirkendall void formation at Cu/Sn–3.5 Ag solder joints. Acta Materialia. 2008;56:5514-23.

[11] Baik S-I, Ahn T-Y, Hong W-P, Jung Y-S, Lee Y-K, Kim Y-W. In situ observations of transgranular crack propagation in high-manganese steel. Scripta Materialia. 2015;100:32-5.

[12] Wan D, Alvaro A, Olden V, Barnoush A. Hydrogen-enhanced fatigue crack growth behaviors in a ferritic Fe-3wt%Si steel studied by fractography and dislocation structure analysis. International Journal of Hydrogen Energy. 2019;44:5030-42.

[13] Farkas D, Van Petegem S, Derlet PM, Van Swygenhoven H. Dislocation activity and nano-void formation near crack tips in nanocrystalline Ni. Acta Materialia. 2005;53:3115-23.

[14] Koyama M, Akiyama E, Sawaguchi T, Raabe D, Tsuzaki K. Hydrogen-induced cracking at grain and twin boundaries in an Fe–Mn–C austenitic steel. Scripta Materialia. 2012;66:459-62.

[15] Tuğluca IB, Koyama M, Shimomura Y, Bal B, Canadinc D, Akiyama E, et al. Lowering Strain Rate Simultaneously Enhances Carbon- and Hydrogen-Induced Mechanical Degradation in an Fe-33Mn-1.1C Steel. Metallurgical and Materials Transactions A. 2019;50:1137-41.

[16] Bal B, Koyama M, Gerstein G, Maier H, Tsuzaki K. Effect of strain rate on hydrogen embrittlement susceptibility of twinning-induced plasticity steel pre-charged with high-pressure hydrogen gas. international journal of hydrogen energy. 2016;41:15362-72.

[17] Bai Y, Momotani Y, Chen MC, Shibata A, Tsuji N. Effect of grain refinement on hydrogen embrittlement behaviors of high-Mn TWIP steel. Materials Science and Engineering: A. 2016;651:935-44.

[18] De Cooman B, Chin K-g, Kim J. High Mn TWIP steels for automotive applications. New trends and developments in automotive system engineering: IntechOpen; 2011.

[19] Chin K-G, Kang C-Y, Shin SY, Hong S, Lee S, Kim HS, et al. Effects of Al addition on deformation and fracture mechanisms in two high manganese TWIP steels. Materials Science and Engineering: A. 2011;528:2922-8.

[20] Mohammadi A, Koyama M, Gerstein G, Maier HJ, Noguchi H. Hydrogen-assisted failure in a bimodal twinning-induced plasticity steel: Delamination events and damage evolution. International Journal of Hydrogen Energy. 2018;43:2492-502.

[21] Gutierrez-Urrutia I, Raabe D. Grain size effect on strain hardening in twinning-induced plasticity steels. Scripta Materialia. 2012;66:992-6.

[22] Barbier D, Gey N, Bozzolo N, Allain S, Humbert M. EBSD for analysing the twinning microstructure in fine-grained TWIP steels and its influence on work hardening. Journal of microscopy. 2009;235:67-78.

[23] Khedr M, Wei L, Na M, Yu L, Xuejun J. Evolution of Fracture Mode in Nano-twinned Fe-1.1 C-12.5 Mn Steel. JOM. 2019:1-11.

[24] Zhong Y, Yin F, Sakaguchi T, Nagai K, Yang K. Dislocation structure evolution and characterization in the compression deformed Mn–Cu alloy. Acta Materialia. 2007;55:2747-56.

[25] Kim S, Choi S-H, Kim S-H, Seo S-J, Suh I-S. Influence of Micro-Texture on Delamination of Hot-Rolled High Strength Low Alloyed Steel Sheets. HSLA Steels 2015, Microalloying 2015 & Offshore Engineering Steels 2015: Springer; 2016. p. 267-71.

[26] Kang J, Li C-n, Yuan G, Wang G-d. Improvement of strength and toughness for hot rolled low-carbon bainitic steel via grain refinement and crystallographic texture. Materials Letters. 2016;175:157-60.

[27] Kwon YJ, Won JW, Park SH, Lee JH, Lim KR, Na YS, et al. Ultrahigh-strength CoCrFeMnNi high-entropy alloy wire rod with excellent resistance to hydrogen embrittlement. Materials Science and Engineering: A. 2018;732:105-11.

[28] Park G, Jeong S, Kang H, Lee C. Improvement of circumferential ductility by reducing discontinuities in a high-Mn TWIP steel weldment. Materials Characterization. 2018;139:293-302.

[29] Rice JR. Elastic-plastic models for stable crack growth. in Mechanics and Mechanisms of Crack Growth (Proc 1973 Conf at: Citeseer; 1975.

[30] Koyama M, Akiyama E, Lee Y-K, Raabe D, Tsuzaki K. Overview of hydrogen embrittlement in high-Mn steels. international journal of hydrogen energy. 2017;42:12706-23.

[31] Lu K, Lu L, Suresh S. Strengthening materials by engineering coherent internal boundaries at the nanoscale. science. 2009;324:349-52.

[32] Lu L, Shen Y, Chen X, Qian L, Lu K. Ultrahigh strength and high electrical conductivity in copper. Science. 2004;304:422-6.

[33] Lu L, Chen X, Huang X, Lu K. Revealing the maximum strength in nanotwinned copper. Science. 2009;323:607-10.

[34] Blochwitz C, Tirschler W. Twin boundaries as crack nucleation sites. Crystal Research and Technology: Journal of Experimental and Industrial Crystallography. 2005;40:32-41.

[35] Demkowicz MJ, Anderoglu O, Zhang X, Misra A. The influence of∑ 3 twin boundaries on the formation of radiation-induced defect clusters in nanotwinned Cu. Journal of Materials Research. 2011;26:1666-75.

[36] King A, Smith D. On the mechanisms of point-defect absorption by grain and twin boundaries. Philosophical Magazine A. 1980;42:495-512.

[37] Koyama M, Springer H, Merzlikin SV, Tsuzaki K, Akiyama E, Raabe D. Hydrogen embrittlement associated with strain localization in a precipitation-hardened Fe–Mn–Al–C light weight austenitic steel. International Journal of Hydrogen Energy. 2014;39:4634-46.

[38] West AJ, Louthan MR. Dislocation transport and hydrogen embrittlement. Metallurgical Transactions A. 1979;10:1675-82.

[39] Chen C-S, Wawrzynek PA, Ingraffea AR. Elastic-plastic crack growth simulation and residual strength prediction of thin plates with single and multiple cracks. Fatigue and Fracture Mechanics: 29th Volume: ASTM International; 1999.

[40] Newman J. An elastic-plastic finite element analysis of crack initiation, stable crack growth, and instability. Fracture Mechanics: Fifteenth Symposium: ASTM International; 1984.

[41] Dieudonné T, Marchetti L, Wery M, Chêne J, Allely C, Cugy P, et al. Role of copper and aluminum additions on the hydrogen embrittlement susceptibility of austenitic Fe–Mn–C TWIP steels. Corrosion Science. 2014;82:218-26.

3.7 Figures

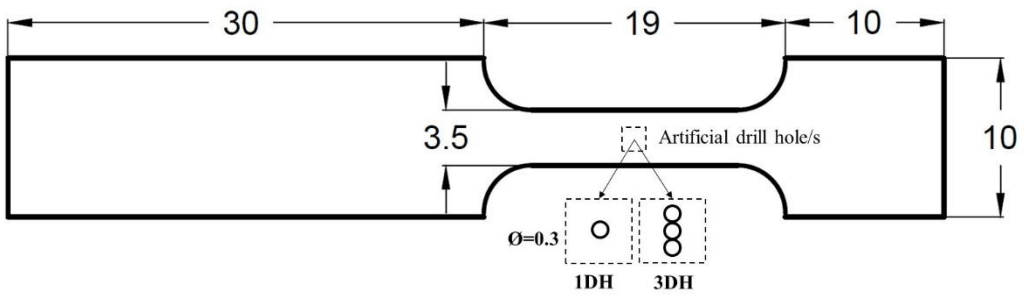

Fig. 3.1. Tensile specimen geometry (in mm). The thickness is 0.25 mm.

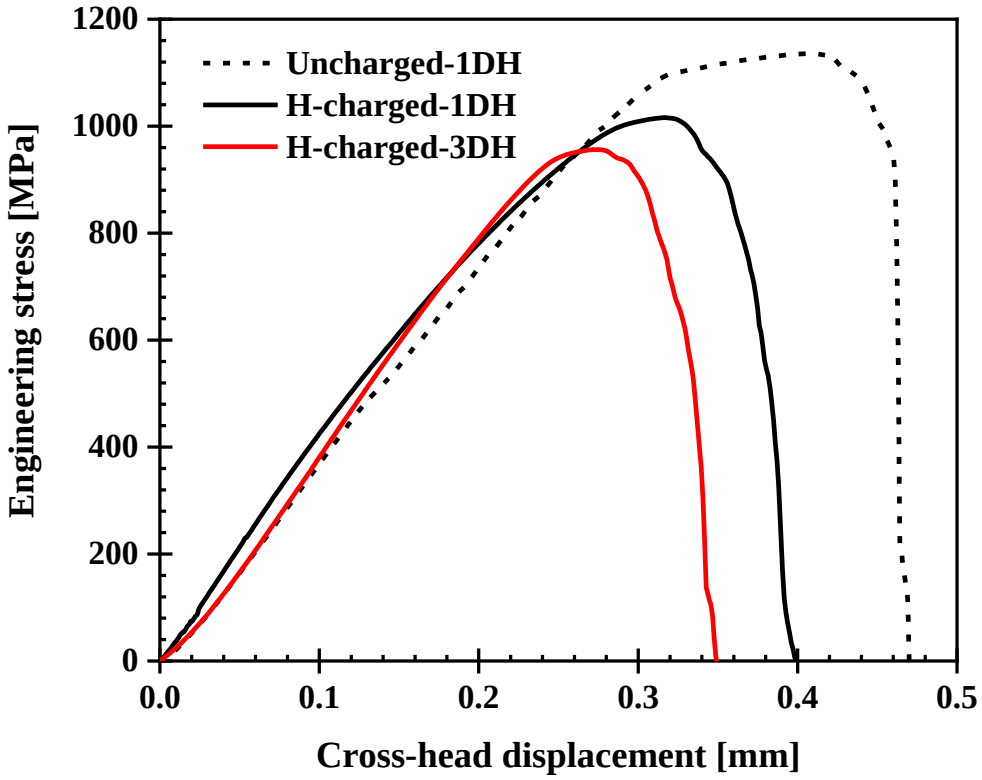

Fig. 3.2. Engineering stress-displacement curves.

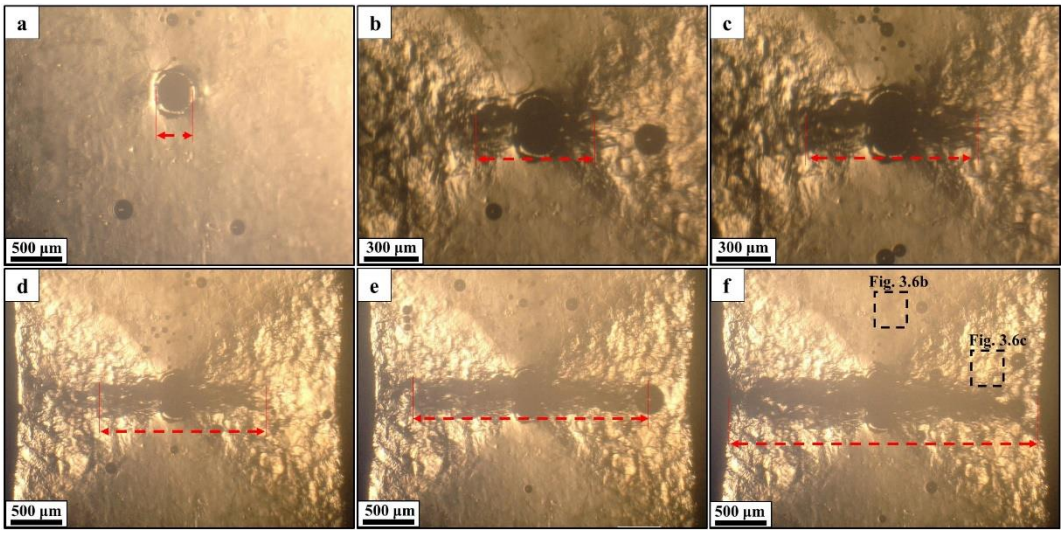

Fig. 3.3. A set of optical images of crack propagation in the hydrogen-charged 1DH specimen taken at (a) before tensile test with 300 μm as a drill hole diameter, (b) 520 μm crack length in 3000 s at 0.3 mm displacement, (c) 850 μm crack length in 3400 s at 0.34 mm displacement, (d) 1420 μm crack length in 3550 s at 0.355 mm displacement, (e) 2400 μm crack length in 3650 s at 0.365 and (f) facture point at 0.4 mm displacement.

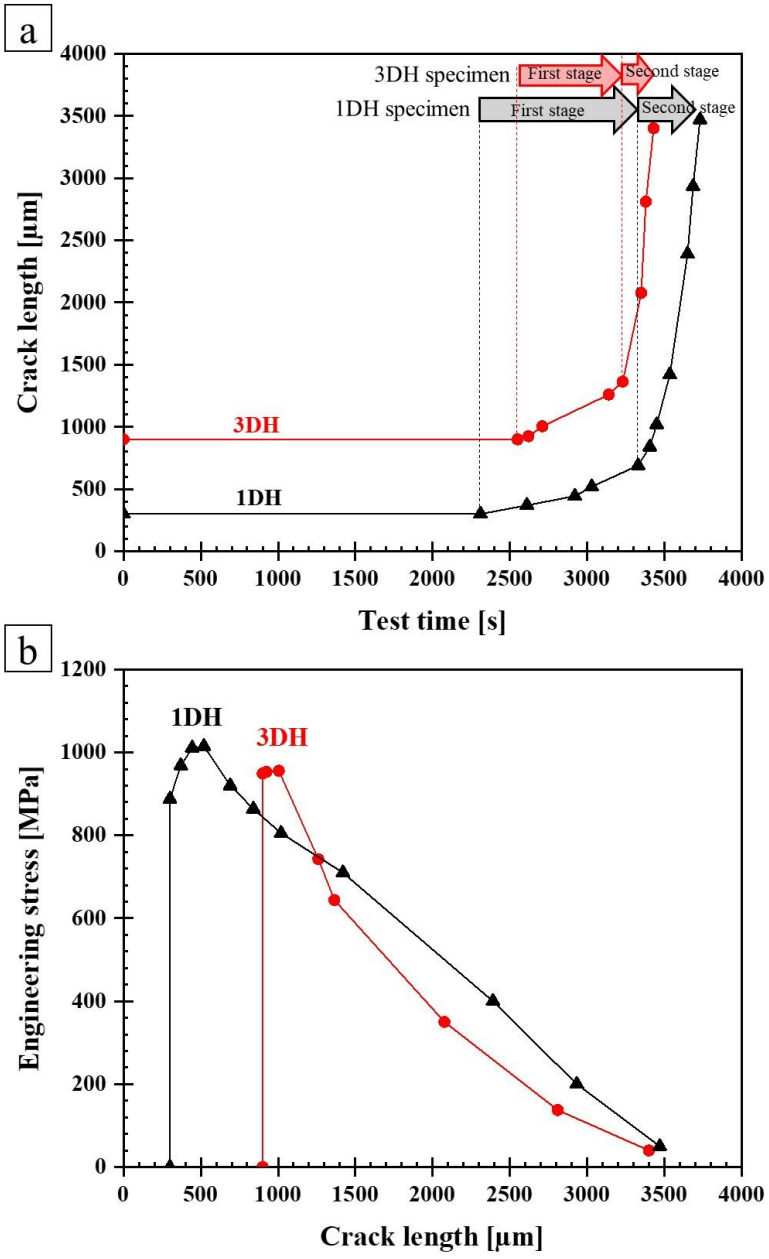

Fig. 3.4. (a) Crack length plotted against test time (b) engineering stress plotted against crack length in the hydrogen charged specimens.

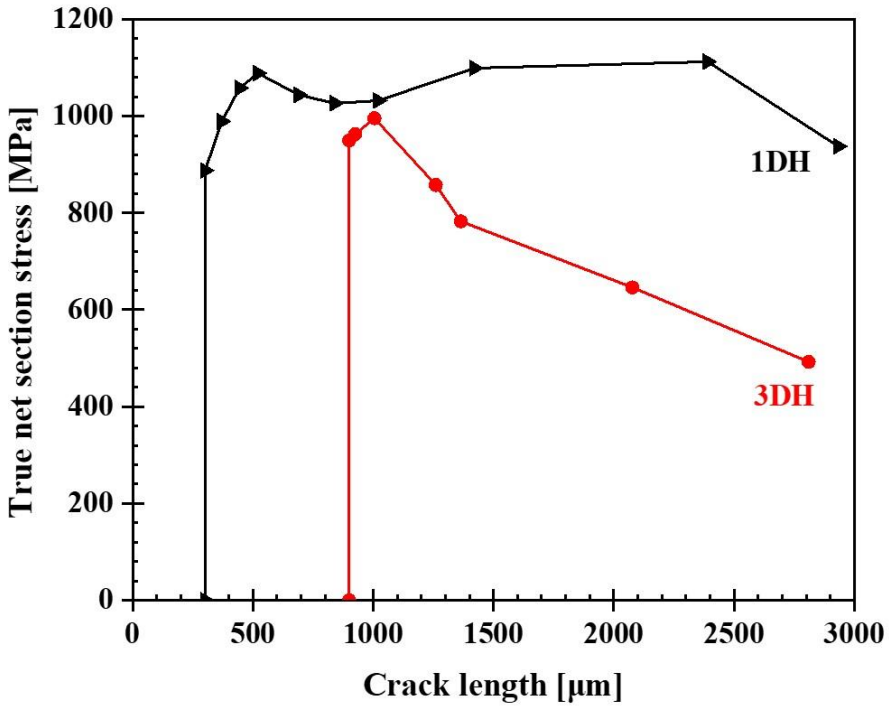

Fig. 3.5. True net sectional stress-total crack length curves in hydrogen charged specimen.

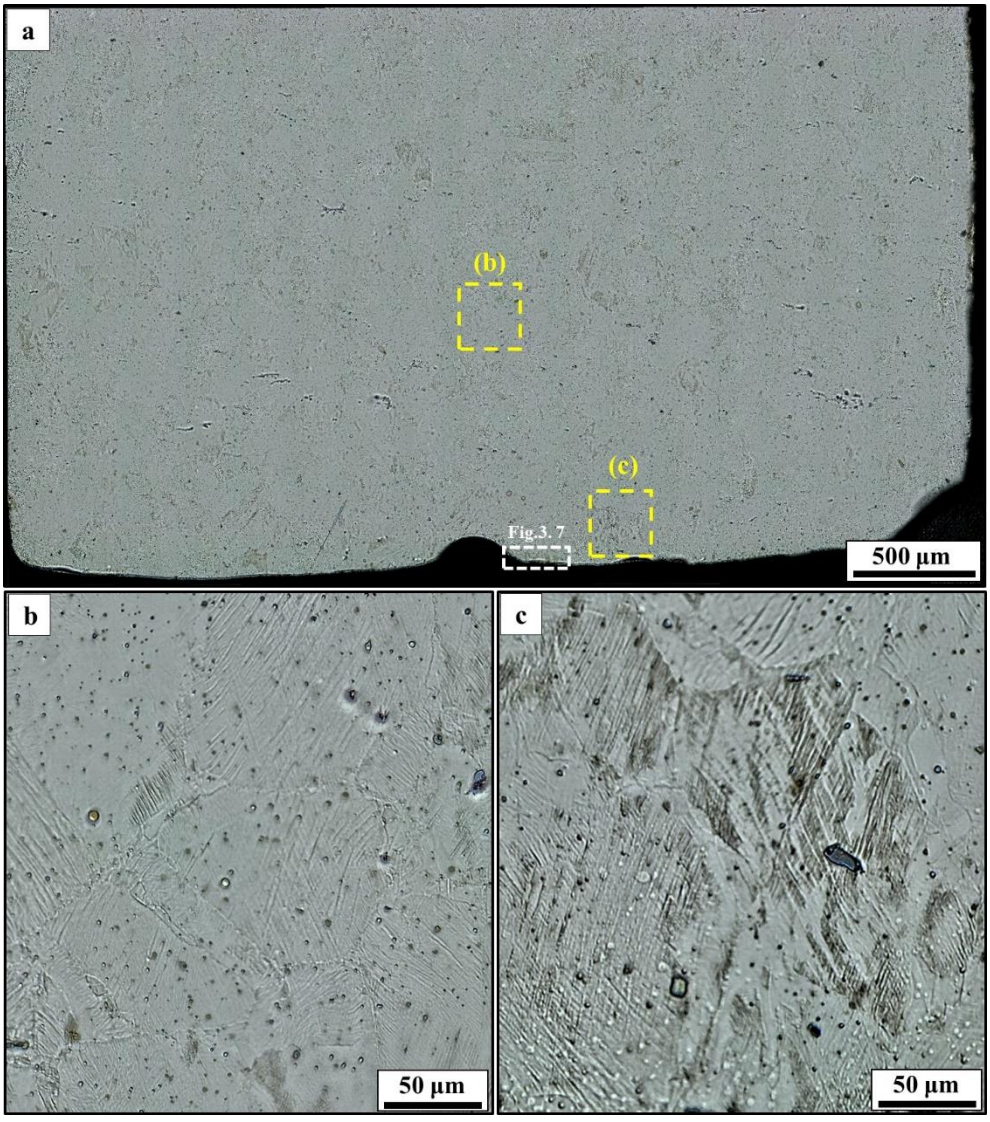

Fig. 3.6. (a) Overall view of the microstructure of hydrogen-charged 1DH specimen after failure; (b) light dense of twining far from micro-hole along tensile direction; (c) high density of twins in the vicinity of the fracture surface. The positions of (b) and (c) correspond to the locations outlined in Fig. 3.3f.

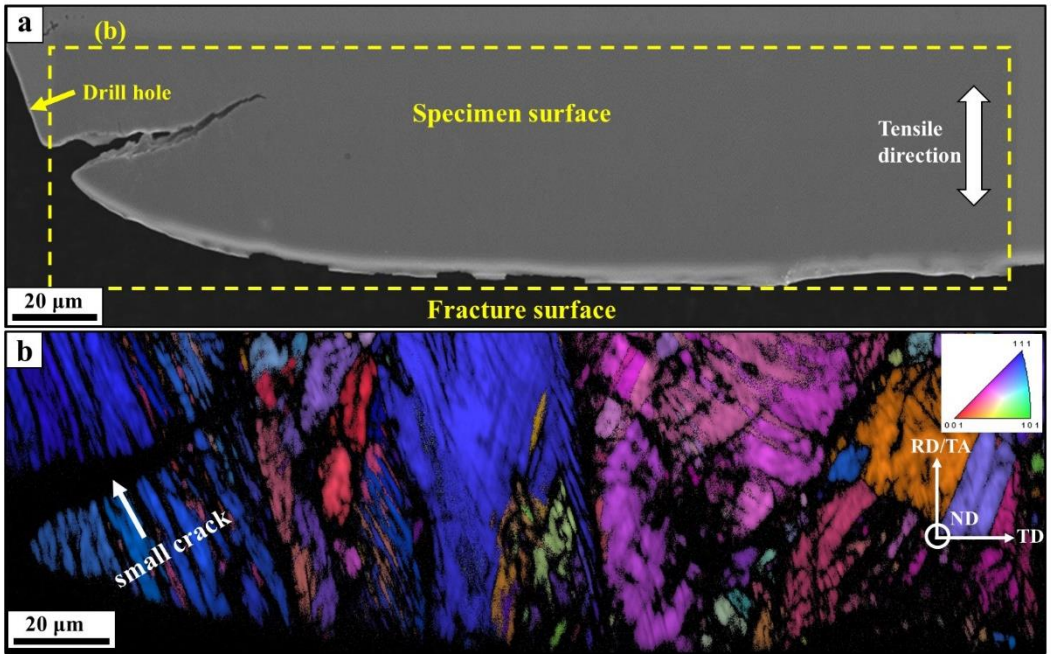

Fig. 3.7. (a) SEM image and (b) corresponding RD-IPF map of surface at the one side of the micro-hole at the vicinity of the fracture surface of hydrogen-charged 1DH specimen after tensile test. The RD-IPF map is superimposed with the IQ contrast.

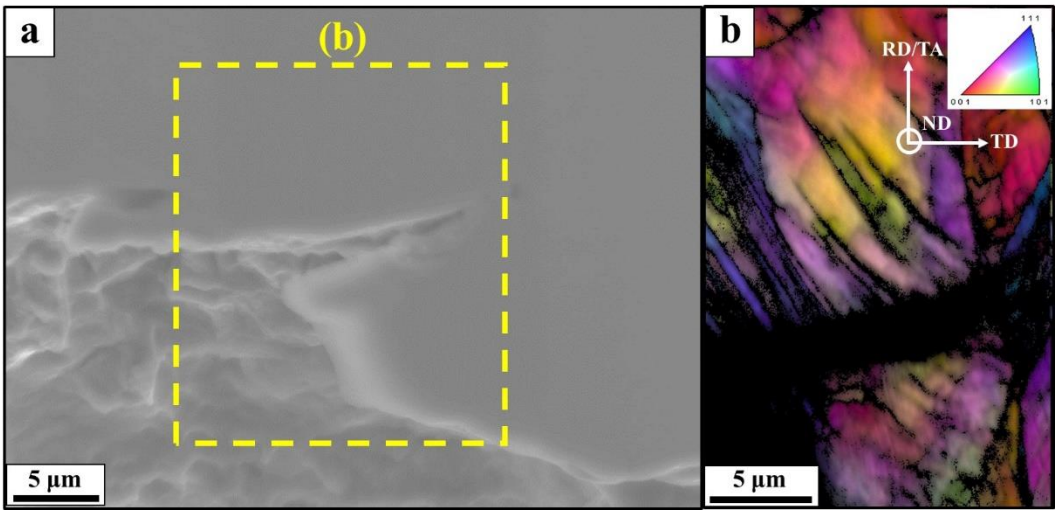

Fig. 3.8. (a) SEM image and (b) corresponding RD-IPF map of the surface crack at the vicinity of the fracture surface in 3DH specimen. The RD-IPF map is superimposed with the IQ contrast.

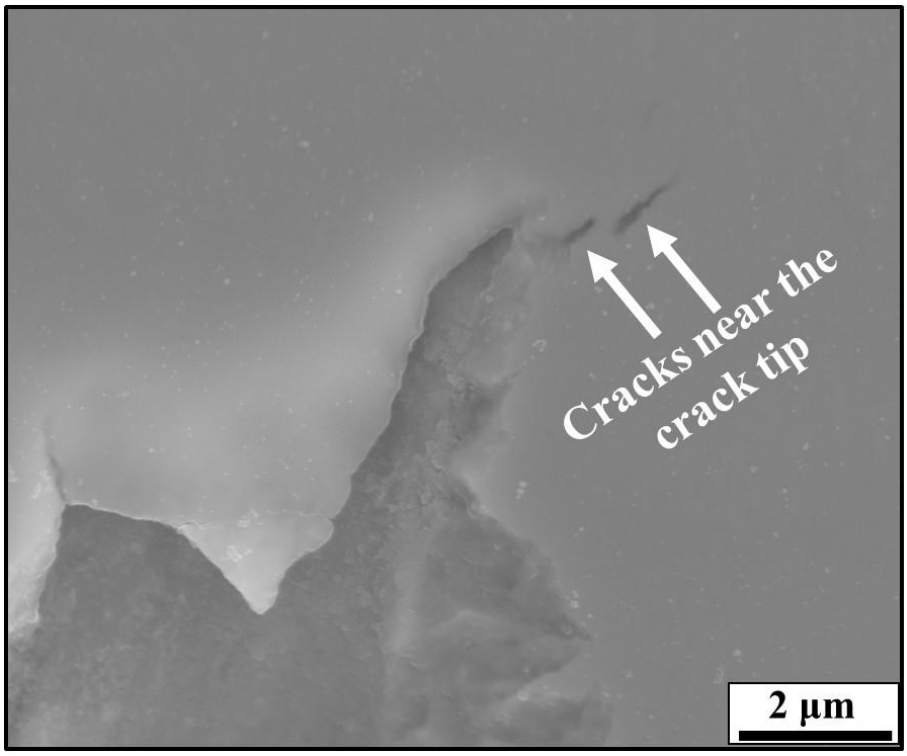

Fig. 3.9. An SEM image showing cracks at a crack tip near the fracture surface.

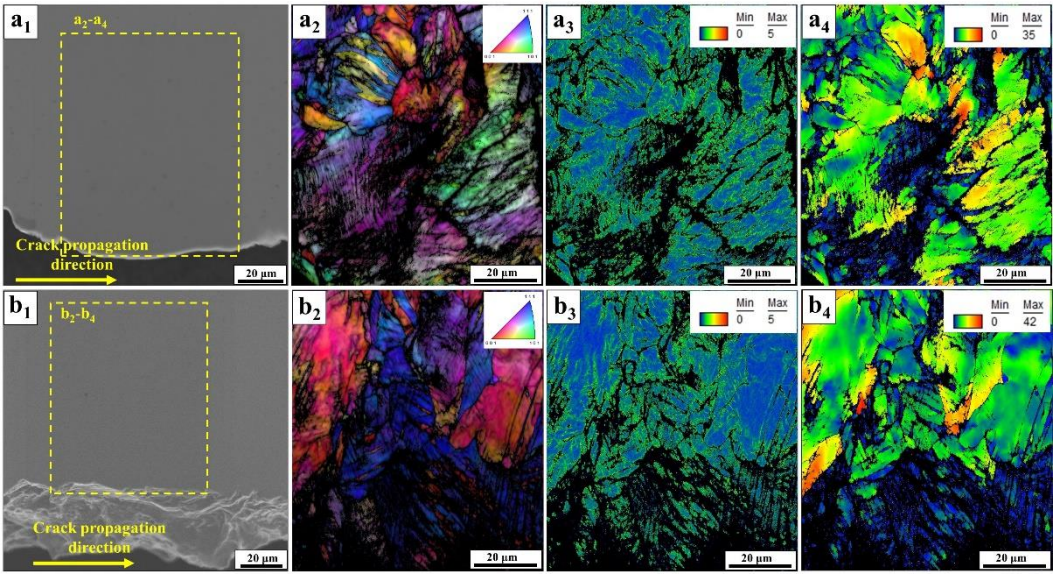

Fig. 3.10. A set of SEM-EBSD results obtained in the hydrogen-charged (a) 1DH and (b) 3DH specimens. (x_1), (x_2), (x_3), and (x_4) exhibit SEM image, RD-IPF map, KAM map, and GROD map, respectively.

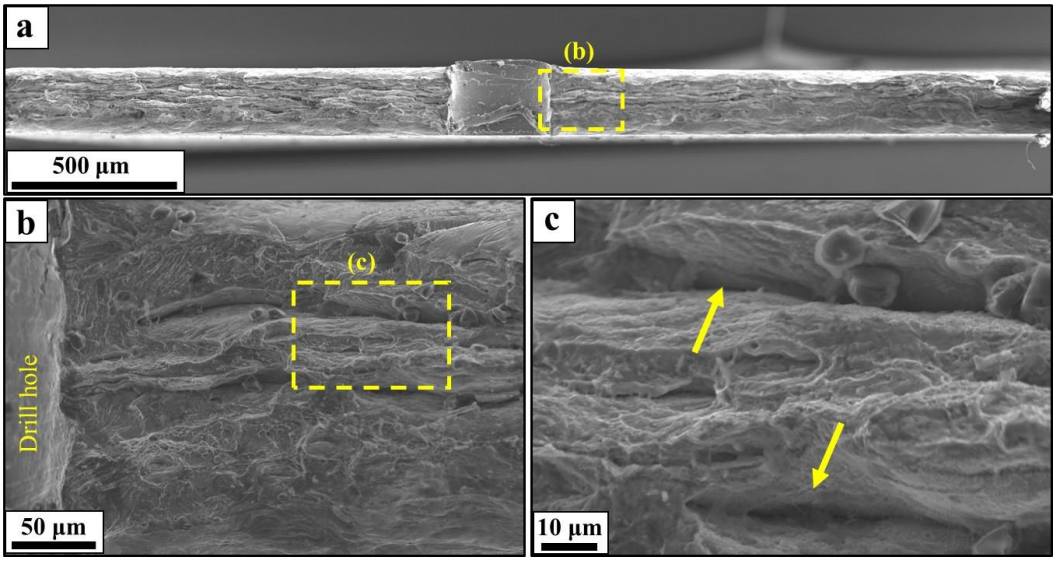

Fig. 3.11. (a) The entire fracture surface of the uncharged 1DH specimen. High magnification details of the areas highlighted in (a) are presented in (b) and (c).

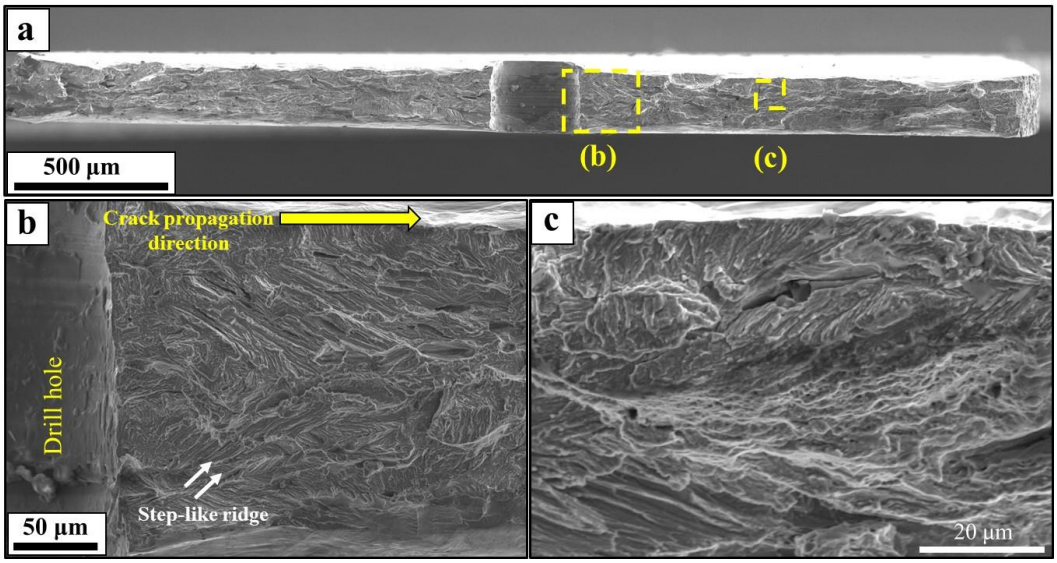

Fig. 3.12. (a) The entire fracture surface of the hydrogen-charged 1DH specimen. High magnification details of the areas highlighted in (a) are presented in (b) and (c).

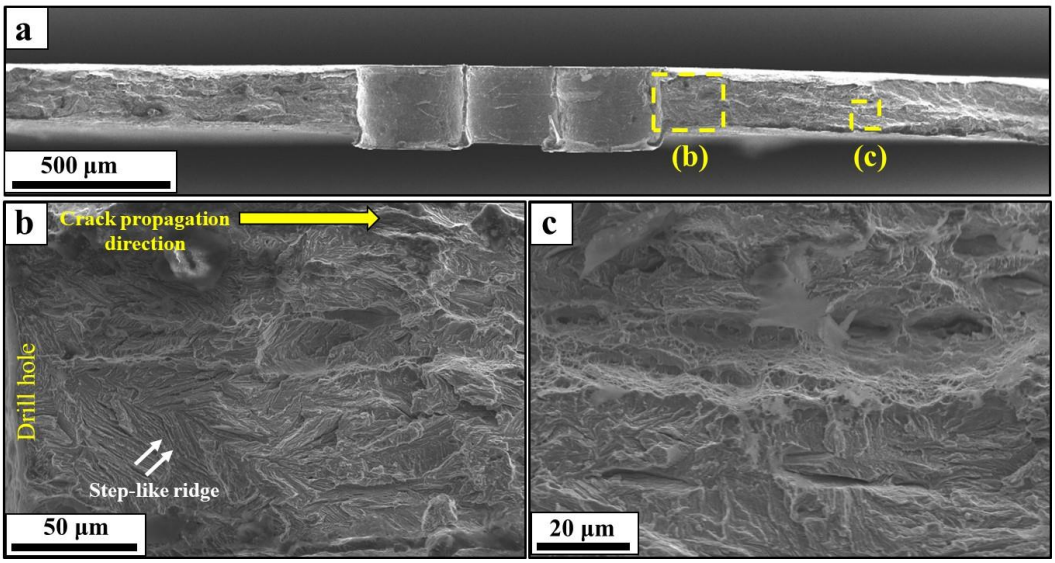

Fig. 3.13. (a) The entire fracture surface of the hydrogen-charged 3DH specimen. High magnification details of the areas highlighted in (a) are presented in (b) and (c).

CHAPTER 4. Precrack length dependency on hydrogen embrittlement of TWIP steel

4.1 Introduction

Most structure members always contain the geometric discontinuities, such as notch or crack-like defects from the manufacturing and machining as well as servicing processes. The main difficulty in designing against fracture in materials particularly in high-strength steels is that the presence of notches or cracks can modify the local stresses. Since crack or notch causes locally triaxial stresses ahead of it, increasing the stress concentration makes hydrogen more aggressive as an embrittling agent [1, 2]. It is reported that there is a systematic loss in fracture stress in hydrogen upon increasing the notch severity [1, 2]. Thus, it is important to select hydrogen-resistant materials, such as *fcc* austenitic steels. These alloys generally retain significant ductility when exposed to hydrogen, owing to the low diffusivity of hydrogen [3]. High-Mn TWIP steels are typical examples of high strength austenitic steels that showed higher resistance to hydrogen embrittlement compare to low carbon steels, martensite steels, dual-phase steels [4-7]. It is well known that hydrogen-assisted cracking processes depend markedly on kinematic variables such as the strain rate [8-11]. However, the applied strain rate is not the most suitable variable in notched or cracked specimens. To obtain the hydrogen-assisted cracking of these specimens we have to consider the effect of the local strain rate at the crack or notch tip, because at that point the hydrogen concentration is localized, and the crack or notch tip strain rate controls the hydrogen-assisted cracking process [12, 13]. In other words, cracking is time dependent and consequently local kinematic variables more precisely, the local strain rate at the crack or notch tip should play a vital role.

Introduction of crack to the specimen can induce the local strain rate at the crack tip under tensile test. However, to the best of my knowledge, there is no previous study on the influence of crack length on hydrogen-assisted cracking of TWIP steel. In order to understand the importance of local strain rate at the crack tip on hydrogen-assisted cracking of TWIP steel, slow strain rate tensile tests were conducted through the electrochemical hydrogen charging for specimens with different precrack lengths introduced under the fatigue service.

4.2 Material and investigation method

4.2.1 Material and test procedure

The material used in this study was Fe-23Mn-0.5C steels (mass%). The chemical compositions of the present steel are listed in details in Table 4.1. Fig. 4.1 demonstrates the initial microstructure of fully austenite TWIP steel. The micrograph in Fig. 4.1a was obtained by mechanical polishing with colloidal silica and chemical etching with a solution of 3% nital (nitric acid in ethanol), followed by cleaning with ethanol. In Fig. 4.1b the microstructure of this material characterized by electron backscatter diffraction (EBSD). The rolling-direction (RD)-inverse pole figure (IPF) map shows that the TWIP steel featured as a uniform grain structure. The corresponding grain distribution plotted in terms of the number and area fraction using EBSD indicated the uniform grain size distribution, as shown in Fig. 4.2. The average grain size, including annealing twin boundaries is measured as 33 μm. The ingots were prepared by vacuum induction melting, and were then forged and groove-rolled at a temperature of 1273 K. Next, the hot rolled bars were solution treated at 1273 K for 1 h and were subsequently water-quenched to suppress the uncontrolled formation of second phases and segregation. The specimens were cut by electrical discharge machining (EDM). The thicknesses were reduced by mechanical grinding. Then, the surface of the specimens was mechanically polished with a mirror finish condition. The final dimensions of the tensile specimens were 10 mm in width, 0.5mm in thickness and 10 mm in gauge length as shown in Fig. 4.3.

The tensile tests were conducted for smooth and center pre-cracked specimens with and without hydrogen charging at an initial strain rate of 10^{-4} s^{-1} equal to the cross-head speed of 10^{-3} mm/s at temperature of 295 K. In case of hydrogen charging, specimens were electrochemically charged with hydrogen in a 3% NaCl aqueous solution containing 3 gL^{-1} of NH_4SCN at a current density of 10 Am^{-2} under the tensile test. The solution was continually added to cover the gauge part of the specimen during the tensile test. A platinum wire was employed as a counter-electrode. The setup the in-situ hydrogen charged specimen is same as indicated in Fig. 2.4.

4.2.2. The precrack introducing

A fatigue servo-hydraulic testing machine was employed to introduce precracks by tension-tension cyclic loading at a load ratio of 0.1 and frequency of 10 Hz. For controlling

the precrack initiation site, we used artificial high stress concentration source by introducing three drill holes following each other at the center of the gauge length perpendicular to the tensile direction. A diameter of each hole equal to 200 μm was introduced by micro drilling technique through the entire of thickness. Subsequently an initial mode I fatigue precrack was introduced ahead of the drill holes. During the fatigue process, the crack length was monitored by optical microscope. The introduced surface fatigue precrack lengths were controlled to be within 1 to 3.2 mm by 1, 1.8, 2.5 and 3.2 mm ($\pm$ 0.1 mm) in length for both hydrogen-charged and uncharged specimens. Finally, before tensile tests, all fatigued-precracks specimens were mechanically polished with a mirror finish condition to remove all surface relief and distortion that could possibly arise from the introduction of holes and fatigued-precracks.

4.2.3. Microstructure characterization

The fracture surface was observed by SEM at an accelerating voltage of 15 kV. In addition, the SEM was used for secondary electron imaging and EBSD measurements of the specimens at an acceleration voltage of 20 kV with a beam step size of 700 nm for the observation of initial microstructure. SEM and EBSD instruments employed in this study are shown in Fig. 2.5.

4.2.4. Modeling for plastic strain rate distribution

The equivalent plastic strain rate distribution in the cracked specimens were calculated by means of FEA using ANSYS Workbench 18.2. A two-dimensional model that equals to one-quarter of the geometry was analyzed due to symmetry, as shown in Fig. 4.4a. The Y-axial displacement of ligament and X-axial displacement of center axis are fixed at 0. A Y-axial displacement, U_y = 0.25 mm, is applied on the top edge of the model. Element type of PLANE183(8-node) was adopted for meshing. Refinement of meshing were arranged in the region near the crack tip, as shown in Fig. 4.4b, and the minimum element size is 0.05 mm. The element numbers for the specimens with pre-crack length of L= 1, 1.8, 2.5 and 3.2 were 3104, 3086, 3064 and 3042, respectively. The The strain hardening model is described by a power-law relation in the form of $\sigma_t = K\varepsilon_t^n$, where σ_t and ε_t are true stress and strain obtained from the tensile test mentioned above, K = 2660.05 MPa is strain hardening coefficient and n = 0.89 is the strain hardening exponent. The influence of hydrogen on the stress–strain

response was not taken into account in the present study because the tensile stress–strain curve of hydrogen charged smooth specimens did not show any clear difference from that of the uncharged specimen before tensile strength.

4.3 Results

4.3.1 Hydrogen effects on mechanical response

Fig. 4.5 shows engineering stress-engineering strain curves in the hydrogen-charged and uncharged smooth specimens. The serrations on the curves are known to be caused by dynamic strain aging as reported in previous studies [14, 15]. The total strain and ultimate tensile strength of the uncharged specimen were 64 % and 870 MPa, respectively. A loss of approximately 50% in ductility and 20% in tensile strength is observed in the presence of hydrogen. The elastic deformation behavior and yield strength were unaffected after hydrogen charging.

Fig. 4.6 displays net section stress-elongation curves of hydrogen-charged and uncharged specimens consistence of precrack length of 1 and 1.8 mm as a definition of short precracks. The net section stress is calculated by dividing the load during tensile test per area of initial net ligament size. This figure indicates the degradation of mechanical properties of short precracks in the presence of hydrogen which deterioration of strength and ductility in specimen with 1 mm precrack is higher than one with 1.8 mm precrack.

Fig. 4.7 shows net section stress-elongation curves of hydrogen-charged and uncharged specimens with precracks of 2.5 and 3.2 mm lengths as a definition of long precracks. Unlike specimens with short precrack, results indicate negligible changes in tensile strength and ductility of hydrogen-charged and uncharged specimens. Results suggest that macroscopic mechanical properties were not affected by the hydrogen charging in long precracked-specimens.

The effect of precrack length on tensile strength and equivalent elongation examined in hydrogen-charged and uncharged specimens is illustrated in Figs. 4.8a and 4.8.b, respectively. The dependence of tensile strength upon precrack shows an obvious decrease in the tensile strength compared the smooth specimen in both hydrogen-charged and uncharged specimens. Results indicate that by increasing the precrack length the effect of hydrogen has been reduced, consequently, the loss of tensile strength and elongation is

decreased, while there is no considerable effect of hydrogen degradation on strength and ductility of specimens with long precrack.

4.3.2 Fractographic analysis

Fig. 4.9 displays the fracture surfaces of hydrogen-charged and uncharged smooth specimens. Observation of fracture surface of uncharged specimen demonstrates a typical ductile fracture surface composed of numerous fine dimples in all areas as shown in overall image of fracture surface in Fig. 4.9a and also in magnified images of Figs. 4.9a_1 and 4.9a_2 of the parts highlighted in Fig. 4.9a. In contrast, a clear region of intergranular combined with partially quasi-cleavage features is observed on the fracture surface of the hydrogen-charged specimen as shown in overall image of charged specimen in Fig. 4.9b and magnified in a Fig. 4.9b_1. The remain part of the fracture surface shows considerable dimples as shown in a magnified image in Fig. 4.9b_2.

Fig. 4.10a and 4.10b show the overview of typical features of the fracture surfaces of uncharged specimens with 1 mm and 3.2 mm precrack as an examples of short and long precrack, respectively. The rest of figures are magnified images corresponding to the highlighted locations indicated in the overviews. The fracture surfaces of both uncharged specimens are characterized by a combination of quasi-cleavage feature regarding to the cyclic loading introduced by fatigued-precrack [16] and follows ductile features with dimples (Figs. 4.10a_1, a_2, b_1 and b_2).

Fig. 4.11 demonstrates the fracture surfaces of hydrogen-charged specimens with 1, 1.8 and 3.2 mm precrack. In case of 1 and 1.8 mm precracked specimens, the fracture surface exhibits a shallow intergranular cracking zone with secondary crack along prior austenite grain boundaries after quasi-cleavage features of precrack. Quasi-cleavage-like features are also observed in the brittle region, as shown in Figs. 4.11a_1, a_2, b_1 and b_2. This brittle region surrounded by dimples and the rest of fracture surface shows ductile feature due to the microvoid coalescence as indicated in Figs. 4.11a_3 and b_3. In contrast, the charged specimens with 3.2 mm precrack shows no brittle feature on the fracture surface, as shown on an overview image of fracture surface in Fig. 4.11c. The fracture surface shows typically ductile with fully dimples same as uncharged one after quasi-cleavage features of precrack region (Figs. 4.11c_1-

c_3). This is to say, there is no effect of hydrogen charging on fracture feature of long-precracked specimens.

Fig. 4.12 shows the surface of uncharged and hydrogen-charged specimens with 1 and 3.2 mm precrack lengths at the vicinity of the fracture surface. There is no observable surface damage of fractured uncharged specimens as shown in Figs. 4.12a and b for 1 and 3.2 mm precracked specimens, respectively, and the magnified images of 4.12a_1 and b_1. In contrast, considerable surface damages due to hydrogen charging can be observed beside the fracture surfaces of both specimens (Figs. 4.12c and d). However, the fraction area of these surface cracks is higher in 1 mm precrack than 3.2 precracked charged specimens as shown clearly in magnified images in Figs. 4.12c_1 and d_1, respectively.

Fig. 4.13 displays the brittle-fracture region length for smooth and precracked specimens under electrochemical hydrogen charging measured from fracture surfaces. This area corresponds to the maximum length of hydrogen affected zone which can be observed on the fracture surface as a brittle area. The area fractions of the intergranular fracture decreased and replaced to the ductile fracture by increasing the precrack length. While, this brittle features diminished completely in the specimens including precrack more than 2 mm (as shown by black arrows) indicated no effect of hydrogen on failure.

4.3.3 Plastic strain rate distribution

Fig. 4.14 displays the distribution of plastic strain rate particularly in the vicinity of the crack tip of specimen with 3.2 mm precrack. This parameter is in the maximum value at the crack tip and has a reduction tendency to the far from crack tip.

Fig. 4.15 shows the calculation results of the distribution of the maximum plastic strain rate for the specimens with various precrack lengths. The strain rate presented here is an average of equivalent plastic strain rate during the 500 s of experiment correspond to the 0.5 mm displacement. Since the stress intensity factor is higher in longer precrack length the plastic strain rate has an increase tendency from 1 to 3.2 mm precrack. This tendency slightly decreases up to the convergence of curves together at approximately 2 mm in front of the crack tip.

4.4 Discussion

Degradation in strength and elongation was occurred in the smooth and short precracked (less than 2 mm) specimens in the presence of hydrogen (Figs. 4.5 and 4.6). The hydrogen-induced intergranular and quasi-cleavage features were observed at these specimens (Figs. 4.9b_1, 4.11a_1, a_2 and 4.11b_1, b_2), as both intergranular and quasi-cleavage are common features of hydrogen embrittlement of TWIP steels [6, 17-19]. Specifically, intergranular cracking has been reported to stem from high micro-stress concentration at grain boundaries interacting with deformation twins [17] and at the grain boundary triple junction [17, 20]. In contrast, the hydrogen-assisted quasi-cleavage in TWIP steels has been reported to arise from twin boundary cracking within the interior of the grains [17, 19, 21]. In case of smooth specimen, hydrogen-assisted failure in TWIP steel has been intensively investigated [6, 7, 21-23]. In short-precracked specimens, the brittle cracking area perceived a head of the precrack tip, particularly localized at the internal section of the fracture surface (Figs. 4.11a_1, a_2, 4.11b_1 and b_2), which is surrounded by dimples, indicating a hydrogen-assisted cracking affected by the high stress triaxiality in the center of the tensile specimen. Additionally, the time for hydrogen to diffuse to the crack tip, contribute to brittle fracture and enhance crack propagation may be longer than that for crack propagation induced by the condition of constrain effect, load and strain rate in these specimens, and this may be the reason that ductile cracking occurred in the rest part of fracture surface (Figs. 4.11a_3, b_3). Some evolved hydrogen diffused in to the steel and enriched around the notch or crack tip because of the local stress and strain gradient [24]. As a specimen is stressed, an elastic stress field with a singularity soon develops, then the elastic singular stress immediately is relaxed as a result of plastic deformation within the notch region, where dislocation sourced in the steel have been activated and both gradient of plastic strain and dislocation density are rather high. Since dislocations are strong hydrogen traps, the local hydrogen concentration is higher in the area with the high dislocation density [24, 25] . Thus, at the crack tip where the plastic strain reaches its maximum value, the interaction between hydrogen and dislocation is significant [6]. Noteworthy that this hydrogen interaction with moving dislocations is correlated to the strain rate [10, 26].

By contrast, specimens by precrack length larger than 2 mm shows different

behavior in the presence of hydrogen. They exhibited negligible loss of tensile strength and ductility in electrochemical hydrogen charging and were considered to be immune from hydrogen embrittlement. In other words, although the stress state is more severe hydrogen could not diffuse sufficiently to the crack tip. Thus, another reason/s are necessary to explain the resistance to hydrogen embrittlement with an increase in the precrack length. This was correlated to the hydrogen diffusion distance which decreases with higher testing speed, as described in [27].

As mentioned above, hydrogen diffusion at the crack or notch tip is correlated to the interaction between hydrogen and dislocation movement which is related to the strain rate. In austenitic steels including TWIP steels the hydrogen diffusivity is a key parameter, which is strongly correlated to the strain rate dependence of the susceptibility for hydrogen embrittlement [18]. The primary reason why the hydrogen embrittlement was more pronounced at the lower strain rate can be attributed to the fact that sufficiently low strain rates allow the hydrogen to interact with moving dislocations [18, 26, 28], which in turn promotes hydrogen embrittlement. Note that cracking is time dependent and consequently local kinematic variables, more precisely the local strain rate at the crack or notch tip, should play a vital role [13]. Although the applied strain rate for all specimens with different precrack lengths is same, various precrack lengths induce different local strain rate at the crack tip; thus, the higher the strain rate at the crack tip, the shorter the time for the hydrogen diffusion. Particularly, in slow strain rate tensile test with precracked or notched specimens, the local strain rate at the crack or notch tip is the variable that controls the hydrogen-induced cracking [13].

Noteworthy, the fully austenitic TWIP steel exhibit low hydrogen diffusivity at room temperature with an approximately hydrogen diffusion coefficient of 10^{-12} cm^2/s [29-32]. Table. 4.2 shows the migration distance of hydrogen in terms of $\sqrt{Dt}$ (where D and t are the hydrogen diffusion coefficient and time of experiment, respectively) for each cracked specimen. Results indicates that the migration distance of hydrogen is too small to associate to the crack propagation. Therefore, hydrogen penetration depth is limited to the surface at the vicinity of the fracture surface where stress concentration is high, leading to surface cracking. Particularly due to the lower diffusion time in 3.2 mm precracked specimen, the near-surface damages are less

compare to the 1 mm one (Figs. 4.12c and 4.12d).

Hydrogen embrittlement of the steel is correlated by local stress and local hydrogen concentration and only occurs when the combination of local stress and local hydrogen concentration is satisfied [11, 25, 33]. As a same context, Wang el. al [11] reported that the relationship between diffusible hydrogen and fracture stress is approximated to the power law in ferritic high strength steels. In addition, Koyama el. al [6] investigated that hydrogen embrittlement of TWIP steel could also be approximated to the power law. In general, it can be explained as the following equation:

$$\sigma_F^* = A{H_D^*}^{-B} \quad (1)$$

Where σ_F^* and H_D^* are local fracture stress and local hydrogen concentration, respectively. A and B are constants and $0<B<1$. According to the power law, the current condition of hydrogen embrittlement due to the relationship between local stress and hydrogen concentration of precracked specimens can be explained schematically in Fig. 4.16. In cracked specimens with 1 and 1.8 mm precracks the critical condition of stress and hydrogen concentration is satisfied and results in a brittle fracture front of the crack tip. In long precracks specimens, although the local stress state is more severe than short precrack one due to the lack of hydrogen diffusion could not reach to the critical condition. Therefore, the fracture is ductile failure.

Particularly, in slow strain rate tensile test with precracked or notched specimens, local strain rate at the crack or notch tip is the variable that controls the hydrogen-induced cracking. FEM results of local strain rate in the ligament path indicted that by increasing the precrack length the local strain rate particularly at the crack tip increases (Fig. 4.15). Increasing in the crack tip strain rate means increasing the dislocation motion and reducing the interaction of hydrogen with dislocation motion, thus, the number of dislocations which are actually carrying hydrogen decreases. Subsequently, diffusion of hydrogen to the crack tip reduces due to lower hydrogen transport on dislocations and hydrogen concentration at the crack tip cannot reach to the critical value to promote hydrogen-assisted cracking. This procedure also can be observed by comparing the fracture surfaces of short precracked specimens (Fig. 4.13). The hydrogen-affected area in 1.8 mm precracked specimen is lower than 1 mm one which clarified the effect of increasing local strain rate, while, there is a higher stress concentration in 1.8 mm precracked specimen.

Finally, by creating a precrack and a higher stress concentration leading to rapid failure, the low diffusivity limited the hydrogen introduced by the charging operation to near surface region. Therefore, hydrogen penetration depth is limited to small portion of crack front at short precracks and the surface at the vicinity of the fracture surface, while in long precrack where stress condition is more severe since the hydrogen has less time to enter and diffuse towards the inner parts of the sample the shallow depth of hydrogen penetration occurs on the surface beside the fracture surface and the ductile fracture occurs as a final failure mode.

4.5 Conclusions

Hydrogen-assisted cracking of TWIP steel in a wide range of precrack geometries tested under electrochemical hydrogen charging at slow strain rate tensile test of 10^{-4} s^{-1}. In case of short precracked specimens less than 2 mm, hydrogen deteriorates the tensile strength and ductility of the specimen compare to the uncharged one. In contrast, long precrack specimens or more than 2 mm which induced higher local strain rate at the crack tip shows no significant of degradation of mechanical properties in the presence of hydrogen. These results confirm the significant role of the local strain rate at the crack tip in hydrogen embrittlement specially at the low strain rate tensile test.

4.6 References

[1] Hardie D, Liu Se. The effect of stress concentration on hydrogen embrittlement of a low alloy steel. Corrosion Science. 1996;38:721-33.

[2] Liu S, Zhu Z, Ke W, Hardie D. Notch severity effect on hydrogen embrittlement of type 4340 steel. Journal of Materials Science and Technology. 1996;12:51-6.

[3] Michler T, Naumann J. Hydrogen embrittlement of Cr-Mn-N-austenitic stainless steels. International Journal of Hydrogen Energy. 2010;35:1485-92.

[4] So KH, Kim JS, Chun YS, Park K-T, Lee Y-K, Lee CS. Hydrogen delayed fracture properties and internal hydrogen behavior of a Fe–18Mn–1.5 Al–0.6 C TWIP steel. ISIJ international. 2009;49:1952-9.

[5] Ronevich JA, Speer JG, Matlock DK. Hydrogen embrittlement of commercially produced advanced high strength sheet steels. SAE International Journal of Materials and Manufacturing. 2010;3:255-67.

[6] Koyama M, Akiyama E, Tsuzaki K. Effect of hydrogen content on the embrittlement in a Fe–Mn–C twinning-induced plasticity steel. Corrosion Science. 2012;59:277-81.

[7] Koyama M, Akiyama E, Sawaguchi T, Raabe D, Tsuzaki K. Hydrogen-induced cracking at grain and twin boundaries in an Fe–Mn–C austenitic steel. Scripta Materialia. 2012;66:459-62.

[8] Krom AH, Koers RW, Bakker A. Hydrogen transport near a blunting crack tip. Journal of the Mechanics and Physics of Solids. 1999;47:971-92.

[9] Momotani Y, Shibata A, Terada D, Tsuji N. Effect of strain rate on hydrogen embrittlement in low-carbon martensitic steel. International Journal of Hydrogen Energy. 2017;42:3371-9.

[10] Tien J, Thompson AW, Bernstein I, Richards RJ. Hydrogen transport by dislocations. Metallurgical Transactions A. 1976;7:821-9.

[11] Wang M, Akiyama E, Tsuzaki K. Effect of hydrogen on the fracture behavior of high strength steel during slow strain rate test. Corrosion science. 2007;49:4081-97.

[12] Toribio J, Elices M. The role of local strain rate in the hydrogen embrittlement of round-notched samples. Corrosion science. 1992;33:1387-95.

[13] Toribio J. The role of crack tip strain rate in hydrogen assisted cracking. Corrosion science. 1997;39:1687-97.

[14] Chen L, Kim H-S, Kim S-K. Localized deformation due to Portevin–LeChatelier effect in 18Mn–0.6 C TWIP austenitic steel. ISIJ international. 2007;47:1804-12.

[15] Allain S, Cugy P, Scott C, Chateau J-P, Rusinek A, Deschamps A. The influence of plastic instabilities on the mechanical properties of a high-manganese austenitic FeMnC steel. International Journal of materials research. 2008;99:734-8.

[16] Habib K, Koyama M, Noguchi H. Impact of Mn–C couples on fatigue crack growth in austenitic steels: Is the attractive atomic interaction negative or positive? International Journal of Fatigue. 2017;99:1-12.

[17] Koyama M, Akiyama E, Tsuzaki K, Raabe D. Hydrogen-assisted failure in a twinning-induced plasticity steel studied under in situ hydrogen charging by electron channeling contrast imaging. Acta Materialia. 2013;61:4607-18.

[18] Bal B, Koyama M, Gerstein G, Maier H, Tsuzaki K. Effect of strain rate on hydrogen embrittlement susceptibility of twinning-induced plasticity steel pre-charged with high-pressure hydrogen gas. international journal of hydrogen energy. 2016;41:15362-72.

[19] Mohammadi A, Koyama M, Gerstein G, Maier HJ, Noguchi H. Hydrogen-assisted failure in a bimodal twinning-induced plasticity steel: Delamination events and damage evolution. International Journal of Hydrogen Energy. 2018;43:2492-502.

[20] Koyama M, Springer H, Merzlikin SV, Tsuzaki K, Akiyama E, Raabe D. Hydrogen embrittlement associated with strain localization in a precipitation-hardened Fe–Mn–Al–C light weight austenitic steel. international journal of hydrogen energy. 2014;39:4634-46.

[21] Koyama M, Akiyama E, Lee Y-K, Raabe D, Tsuzaki K. Overview of hydrogen embrittlement in high-Mn steels. international journal of hydrogen energy. 2017;42:12706-23.

[22] Koyama M, Springer H, Merzlikin SV, Tsuzaki K, Akiyama E, Raabe D. Hydrogen embrittlement associated with strain localization in a precipitation-hardened Fe-Mn-Al-C light weight austenitic steel. International Journal of Hydrogen Energy. 2014;39:4634-46.

[23] Koyama M, Akiyama E, Tsuzaki K. Hydrogen embrittlement in Al-added twinning-induced plasticity steels evaluated by tensile tests during hydrogen charging. ISIJ international. 2012;52:2283-7.

[24] Qiao L, Luo J, Mao X. Hydrogen evolution and enrichment around stress corrosion crack tips of pipeline steels in dilute bicarbonate solution. Corrosion. 1998;54:115-20.

[25] Wang M, Akiyama E, Tsuzaki K. Effect of hydrogen and stress concentration on the notch tensile strength of AISI 4135 steel. Materials Science and Engineering: A. 2005;398:37-46.

[26] Birnbaum HK, Sofronis P. Hydrogen-enhanced localized plasticity—a mechanism for hydrogen-related fracture. Materials Science and Engineering: A. 1994;176:191-202.

[27] Depover T, Wallaert E, Verbeken K. Fractographic analysis of the role of hydrogen diffusion on the hydrogen embrittlement susceptibility of DP steel. Materials Science and Engineering: A. 2016;649:201-8.

[28] Robertson I. The effect of hydrogen on dislocation dynamics. Engineering Fracture Mechanics. 1999;64:649-73.

[29] De Cooman BC. Materials design: the key to modern steel products: GRIPS media; 2007.

[30] Perng T-P, Altstetter C. Hydrogen effects in austenitic stainless steels. Materials Science and Engineering: A. 1990;129:99-107.

[31] Tsong-Pyng P, Altstetter C. Effects of deformation on hydrogen permeation in austenitic stainless steels. Acta Metallurgica. 1986;34:1771-81.

[32] Ronevich J, Kim S, Speer J, Matlock D. Hydrogen effects on cathodically charged twinning-induced plasticity steel. Scripta Materialia. 2012;66:956-9.

[33] Lufrano J, Sofronis P. Enhanced hydrogen concentrations ahead of rounded notches and cracks—competition between plastic strain and hydrostatic stress. Acta materialia. 1998;46:1519-26.

4.7 Tables and Figures

Table. 4.1. Chemical composition of the investigated TWIP steel

Steel	Ni	Mn	Cr	Si	C	P	S	Fe
Fe-23Mn-0.5C	0.003	22.6	<0.001	0.027	0.51	<0.001	0.0072	Bal.

Table 4.2. Calculation of the migration distance of hydrogen by hydrogen diffusion coefficient during the tensile test for each precrack length

Precrack length [mm]	Maximum elongation[mm]	Time [s]	$\sqrt{Dt}$ [μm]
1	2.416	2416	0.49152823
1.8	2	2000	0.4472136
2.5	1.85	1850	0.43011626
3.2	1.53	1530	0.39115214

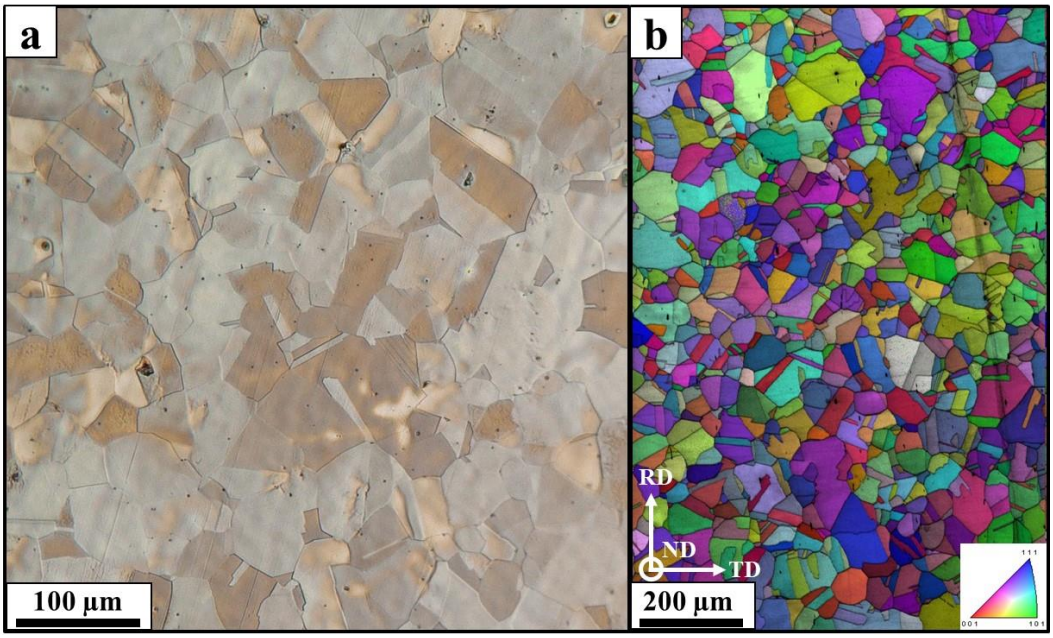

Fig. 4.1. (a) Optical image of the etched specimen (b) RD-IPF, of micrograph of the initial microstructure of TWIP steel.

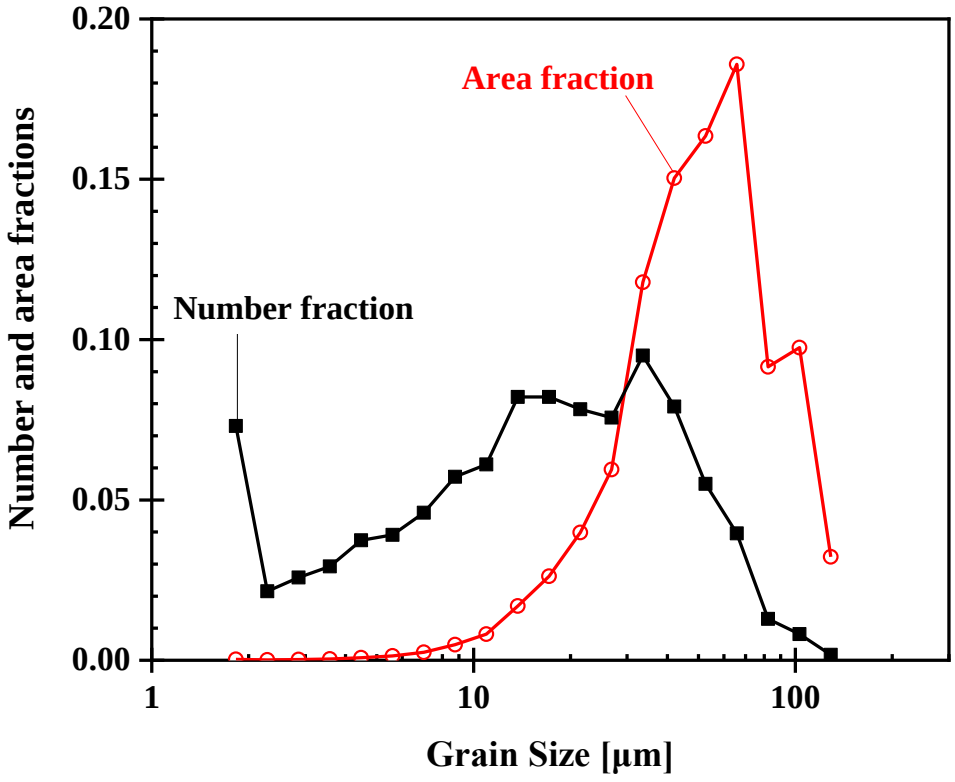

Fig. 4.2. Number and area fraction of grain size distribution of investigated TWIP steel.

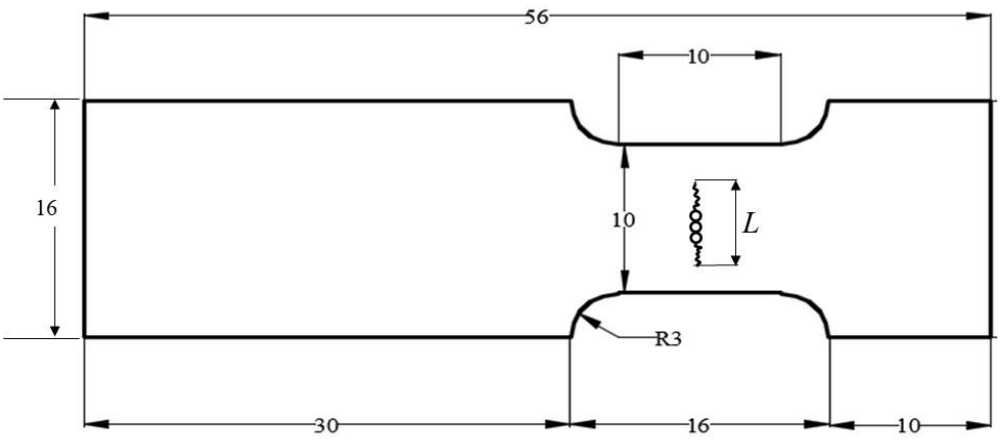

Fig. 4.3. Tensile specimen geometry (in mm). The thickness is 0.5 mm and L corresponds to the precrack length.

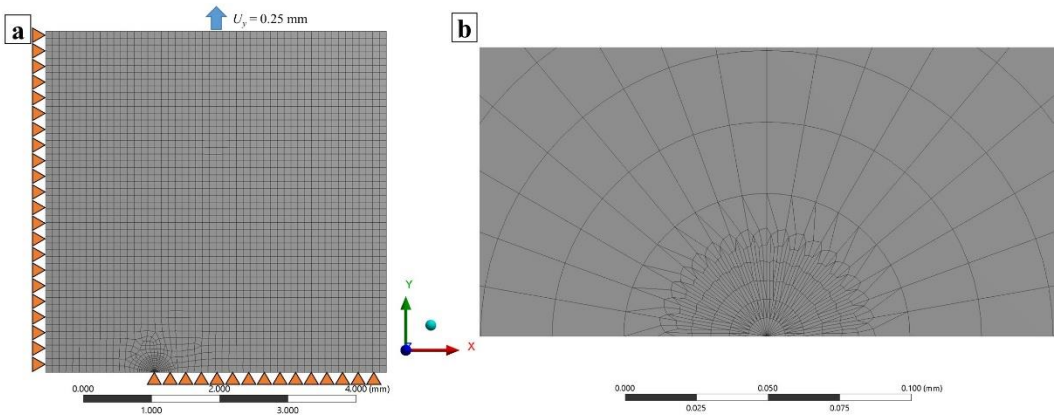

Fig. 4.4. (a) Model simplification for calculation of strain rate distribution, (b) magnified of meshed zone in the vicinity of the crack tip for the specimen with 3.2 mm precrack.

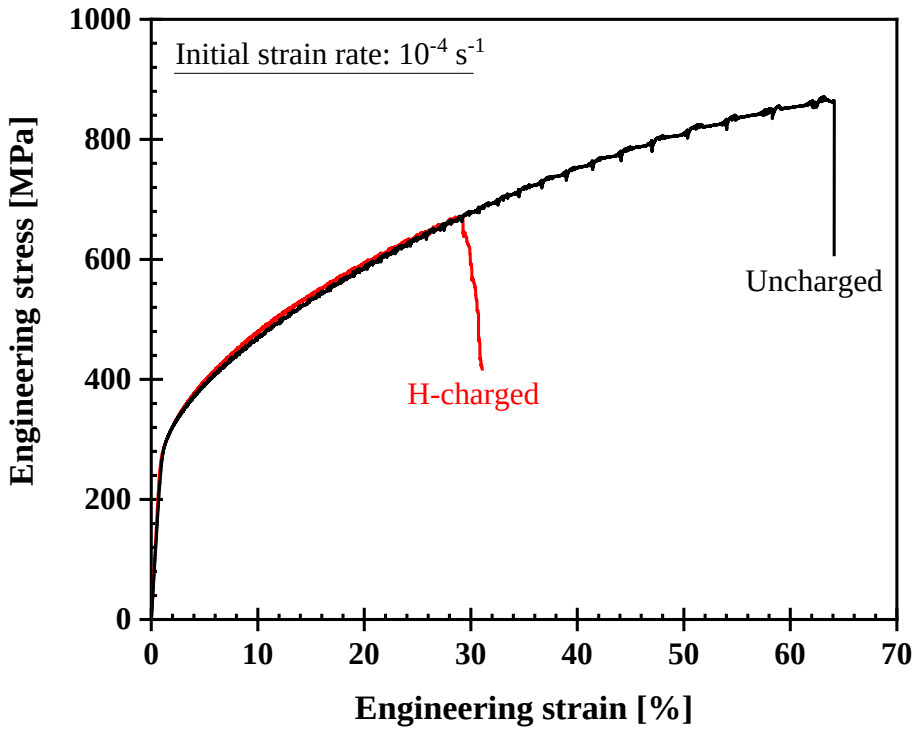

Fig. 4.5. Engineering stress–engineering strain curve for uncharged and hydrogen-charged of smooth specimens.

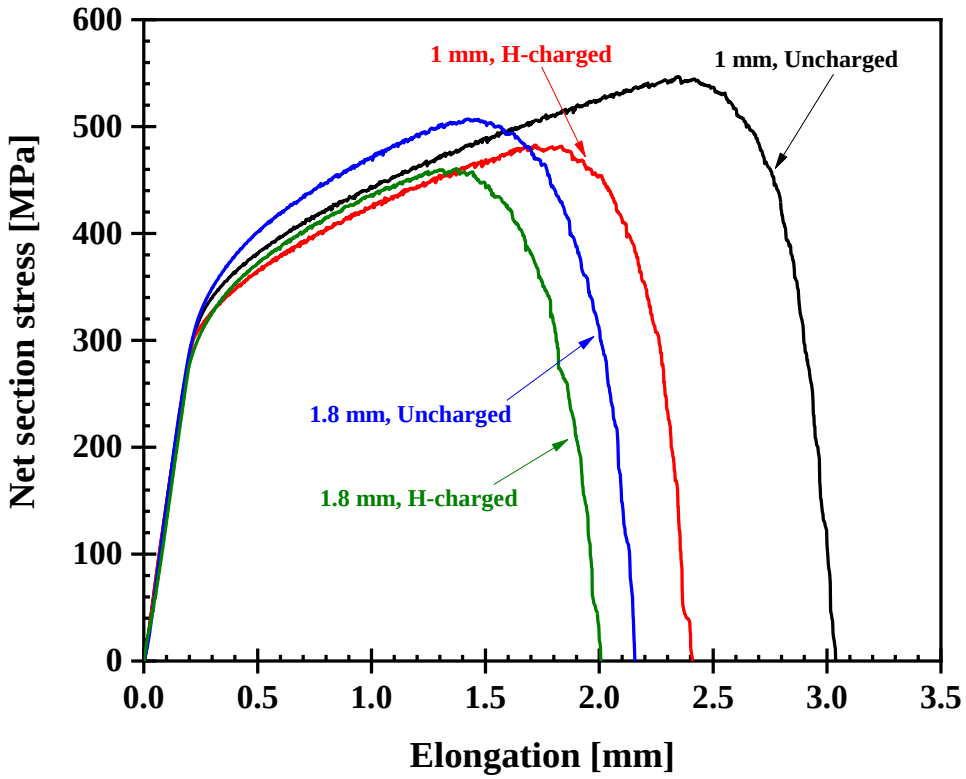

Fig. 4.6. Net section stress-elongation curves for uncharged and hydrogen-charged specimens consistence of precrack length of 1 and 1.8 mm.

.

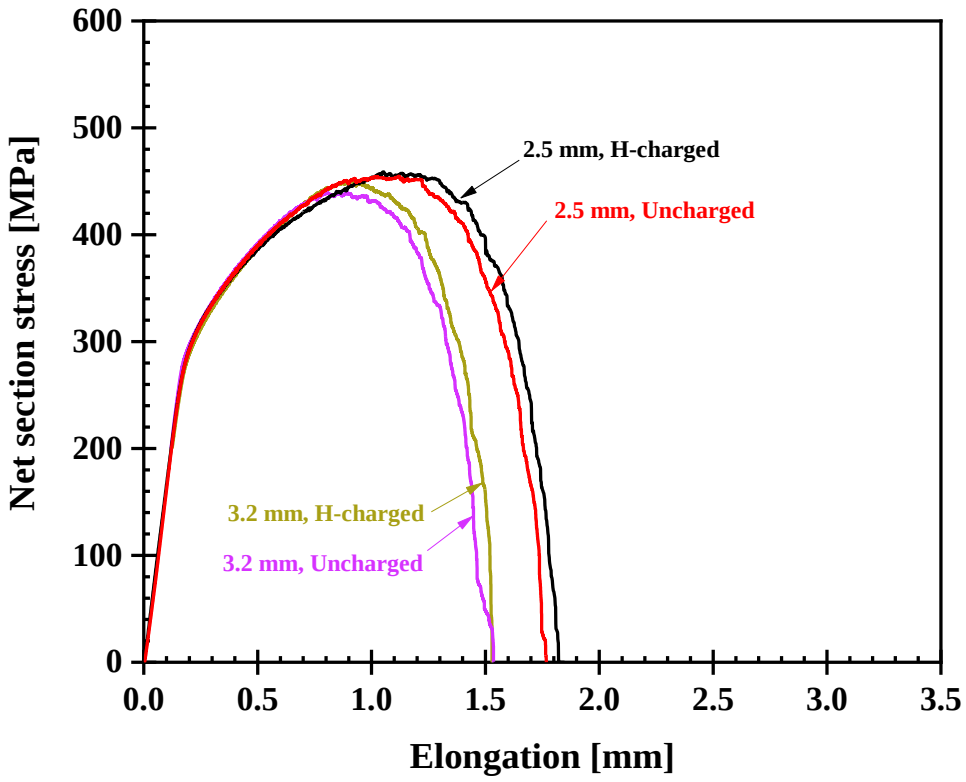

Fig. 4.7. Net section stress-elongation curves for uncharged and hydrogen-charged specimens consistence of precrack length of 2.5 and 3.2 mm.

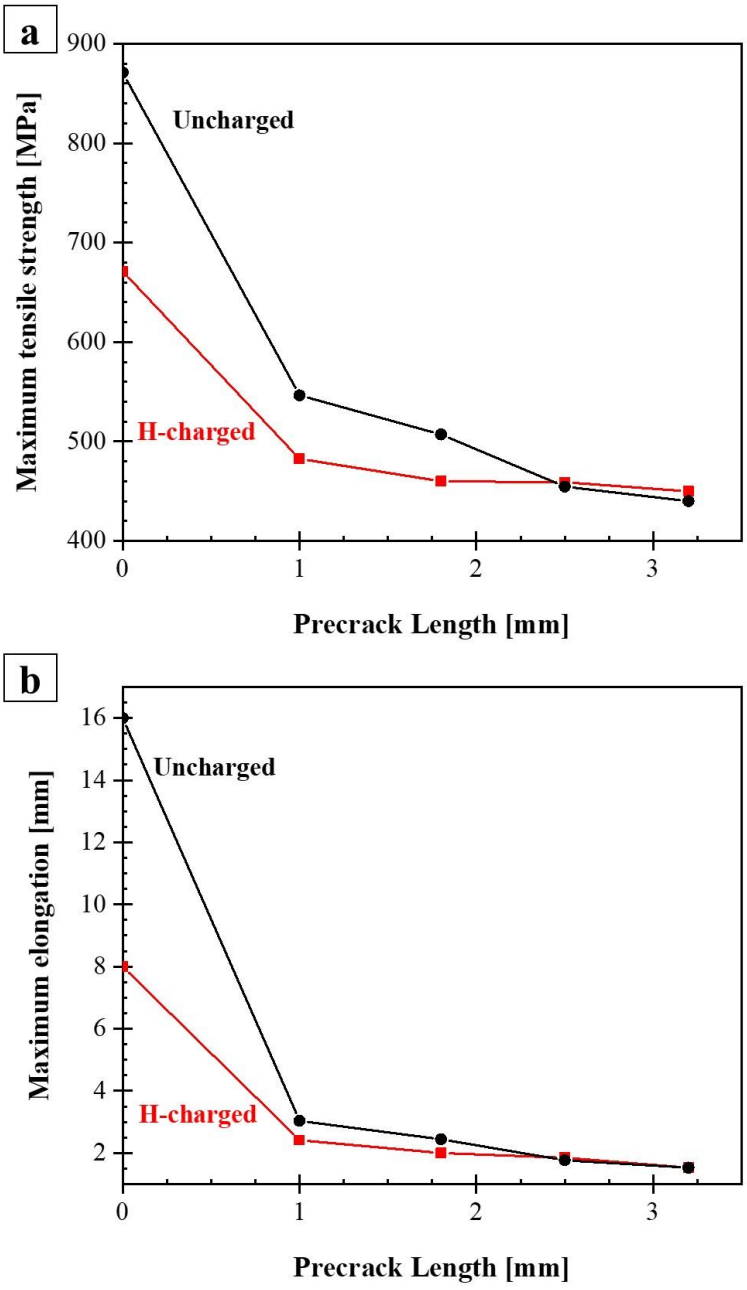

Fig. 4.8. Comparison between maximum (a) tensile strength and (b) elongation of uncharged and hydrogen-charged specimens in different precrack lengths of 1, 1.8, 2.5 and 3.2 mm including smooth specimens.

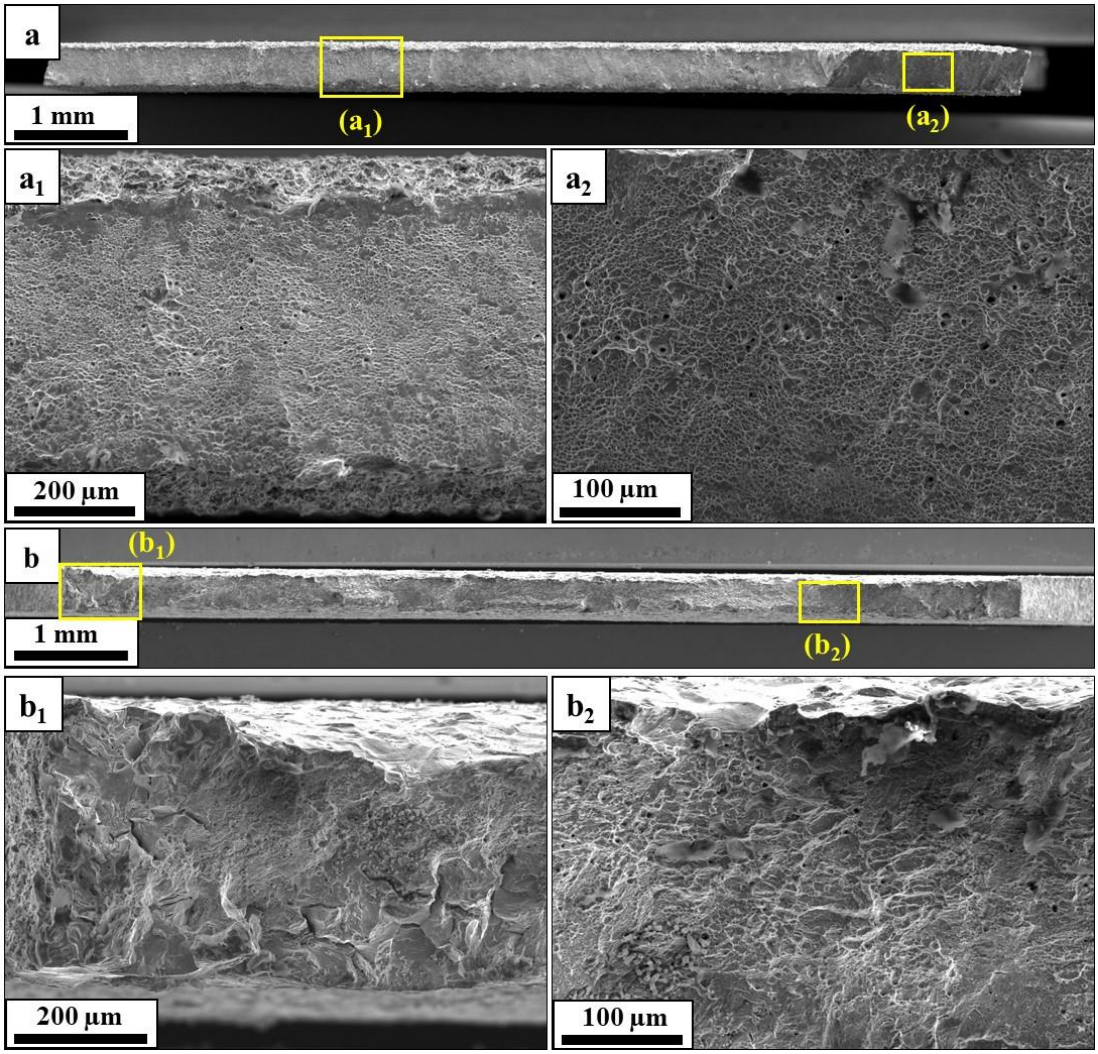

Fig. 4.9. (a) and (b) overall images of fracture surfaces of uncharged and hydrogen-charged smooth specimens, respectively. (a_1) and (a_2) magnified images correspond to the highlight regions in (a) show ductile feature as a void coalescence in entire fracture surface. (b_1) and (b_2) magnified images correspond to the highlight area in (b). (b_1) displays the brittle area combination of intergranular and quasi-cleavage and (b_2) shows rest of the fracture surface covered by dimples as a ductile feature.

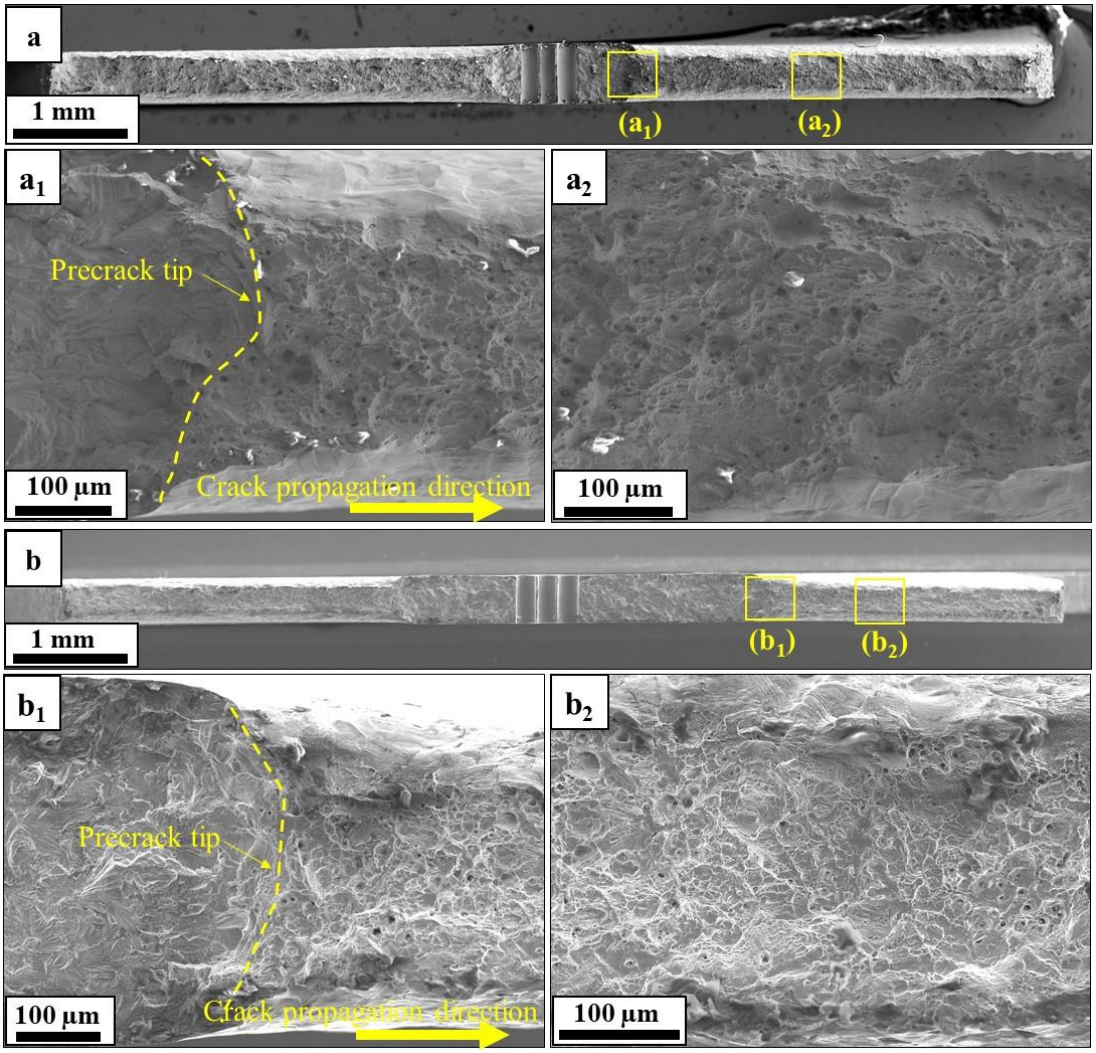

Fig. 4.10. (a) and (b) overall images of fracture surfaces of uncharged specimen with 1 and 3.2 mm precracks, respectively. (a_1) and (b_1) are the magnified images highlighted in (a) and (b) respectively, correspond to the precrack tip fracture surface which followed by dimples after quasi-cleavage feature of fatigued-precracks as shown in (a_2) and (b_2). The yellow dashed lines indicate the precrack tip.

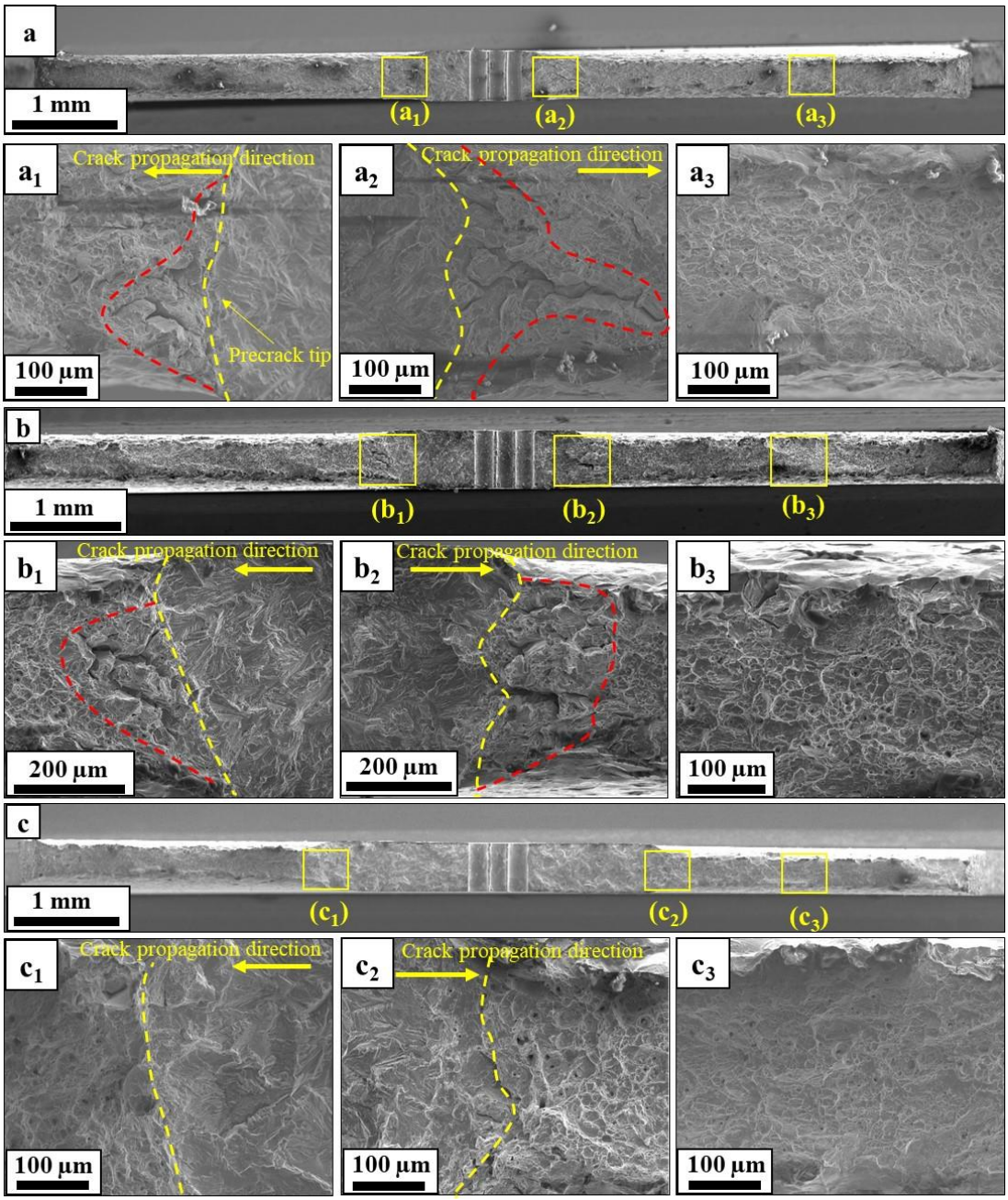

Fig. 4.11. (a), (b) and (c) overall images of fracture surfaces of hydrogen-charged specimen with 1, 1.8 and 3.2 mm precracks, respectively. X_1 and X_2 show the both sides of the fracture surfaces including precrack tips. For 1 and 1.8 mm precracks the fracture surfaces in front of the crack tip display the combination of intergranular and quasi-cleavage features, while, 3.2 mm precracked specimen show ductile feature as a void coalescence similar to the uncharged specimens. The remain parts of the fracture surface covered by dimples as shown in Figs. (a_3), (b_3) and (c_3). The yellow and red dashed-lines indicate the precrack tip and enclosed the brittle zone, respectively.

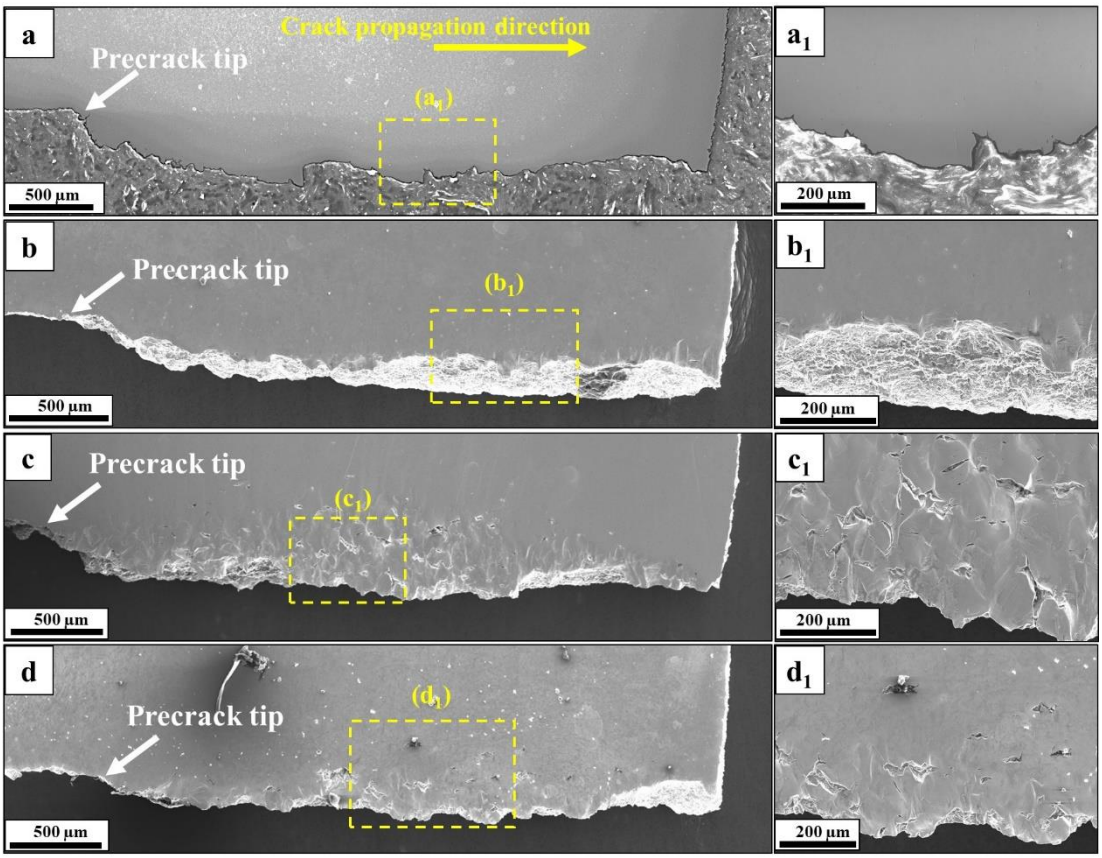

Fig. 4.12. Showing specimen surfaces in the vicinity of the fracture surfaces. (a) and (b) for 1 and 3.2 mm precracked uncharged specimens, respectively. Magnified images of (a_1) and (b_1) correspond to the highlight area in (a) and (b) show no surface crack appeared beside the fracture surface. (c) and (d) for 1 and 3.2 precracked hydrogen-charged specimens, respectively, display the surface damage near the fracture surface in the presence of hydrogen. Comparison between (c_1) and (d_1), the magnified images in (c) and (d), indicate that the hydrogen effect of 1 mm precrack is stronger in formation of surface cracks than 3.2 mm.

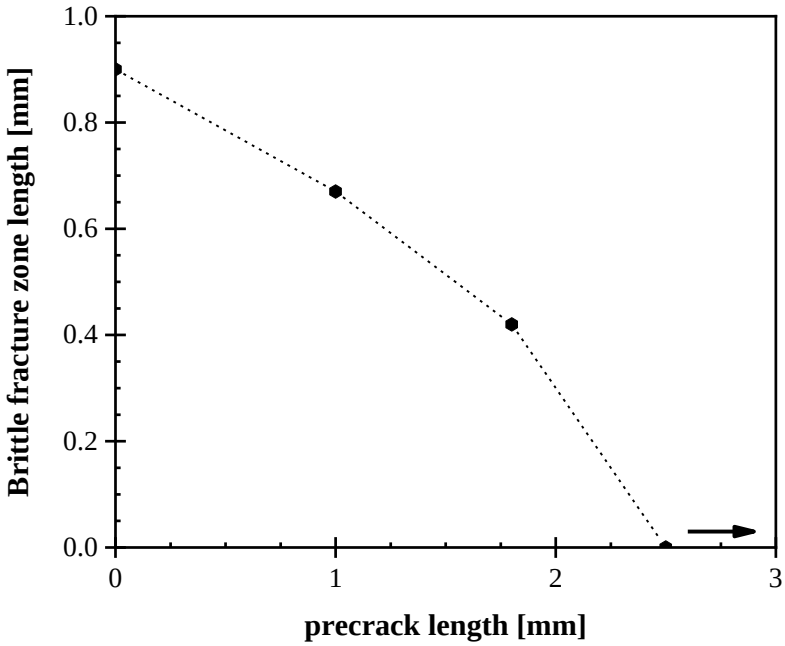

Fig. 4.13. Maximum brittle fracture zone size after tensile test in specimens with different crack lengths.

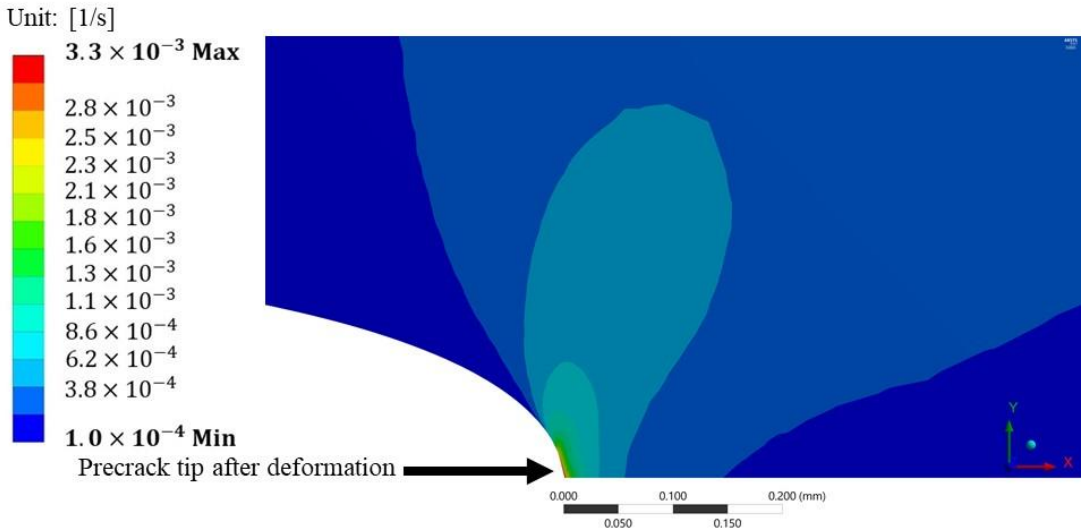

Fig. 4.14. Average equivalent plastic strain rate distribution at the vicinity of the precrack tip of specimen with 3.2 mm precrack calculated by FEA.

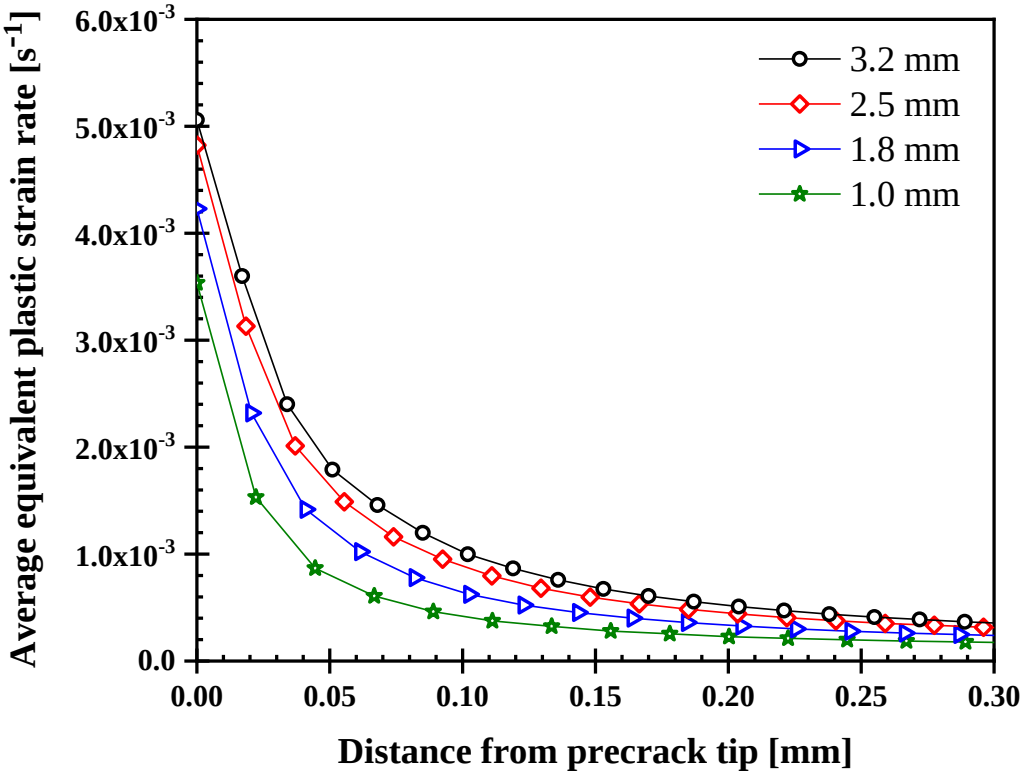

Fig. 4.15. FEA calculation results on the distribution of average equivalent plastic strain rate of cracked specimens.

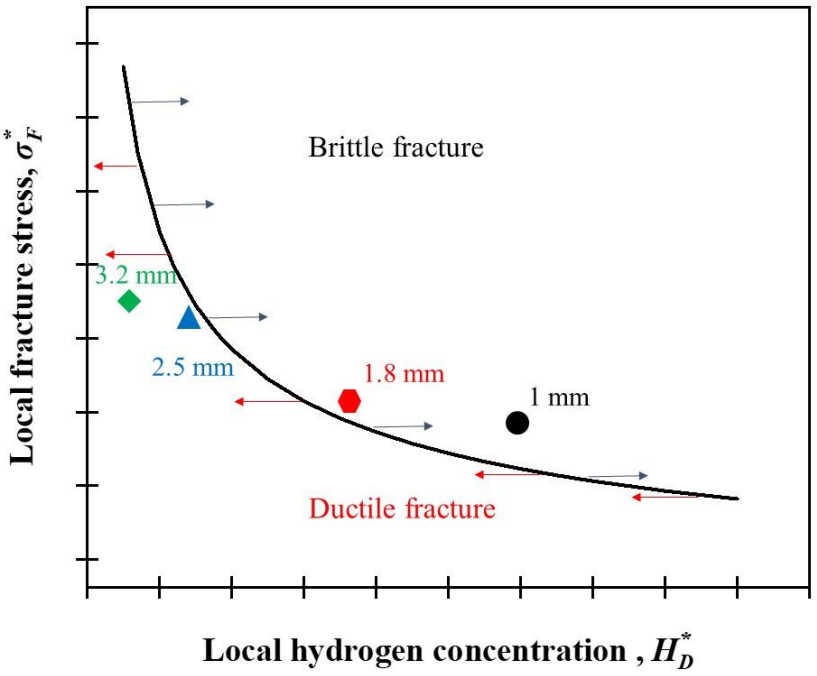

Fig. 4.16. the schematic of relationship between local fracture stress and local hydrogen concentration at the crack tip.

CHAPTER 5. Effect of strain rate on the hydrogen-assisted cracking in cracked-specimen of TWIP steel

5.1 Introduction

It is well-known that hydrogen embrittlement behavior depends on not only microstructure but also deformation conditions. Hydrogen-assisted cracking processes depend markedly on kinematic variables such as the strain rate. The effect of decreasing strain-rate and decreasing potential on ductility can be generally explained on the respective bases of a greater time being available during testing for hydrogen to enter the steel, and of more hydrogen being available for entry into the steel [1-3]. In common with higher strength steels, the observed hydrogen embrittlement is strain-rate dependent; the loss of ductility increases as the strain rate decreases.

Strain rate dependence of hydrogen embrittlement demonstrates that the transportation of hydrogen to crack front is necessary and understanding the kinetics of hydrogen embrittlement is important. Thus, subjecting the notched or cracked tensile specimens to slow strain rate tensile tests under hydrogen-charging condition is the most severe condition to study the effects of hydrogen on the tensile behavior of the materials [4].

In austenitic steels including TWIP steels the hydrogen diffusivity is a key parameter, which is strongly correlated to the strain rate dependence of the susceptibility for hydrogen embrittlement [5]. Therefore, the strain rate dependence of hydrogen embrittlement behavior in the TWIP steels is a crucial issue.

In this chapter, I study the behavior of cracked specimens of TWIP steel to understand the effect of various applied strain rates on the hydrogen-assisted cracking under the electrochemical hydrogen charging condition.

5.2 Material and investigation method

The material in this chapter is same as used in the 4th chapter, Fe-23Mn-0.5C steels (mass%) fully austenitic TWIP steel with the average grain size of 35 μm. The procedure of preparing specimens is also same as the procedure in the previous chapter. In this chapter, specimens are same as previous chapter. The difference is just fatigued-precrack lengths.

The introduced surface fatigued-precrack lengths were limited to 1.5 and 3 mm as an examples of short and long precracks defined in the 4th chapter. The final configuration of

the specimens is shown in Fig. 4.3. Finally, before tensile tests, all fatigued-precracks specimens were mechanically polished with a mirror finish condition to remove all surface relief and distortion that could possibly arise from the introduction of holes and fatigued-precracks.

The tensile tests were conducted for specimens with and without hydrogen charging at slow strain rates, namely at an initial strain rates of 10^{-4} and 10^{-5} s^{-1} for specimens with 1.8 mm precrack length as an example of short precrack and specimens with 3.2 mm precrack length as an example of long precrack, defined in the 4th chapter, at ambient temperature.

In case of hydrogen charging, specimens were electrochemically charged with hydrogen in a 3% NaCl aqueous solution containing 3 gL^{-1} of NH_4SCN at a current density of 10 Am^{-2} under the tensile test. The solution was continually added to cover the gauge part of the specimen during the tensile test. A platinum wire was employed as a counter-electrode. The setup the in-situ hydrogen charged specimen is same as indicated in Fig. 2.4. The fracture surface was observed by SEM at an accelerating voltage of 15 kV.

5.3 Results

5.3.1 Hydrogen effects on mechanical response

Fig. 5.1 shows the net section stress-elongation curves with the corresponding tensile properties of the specimen with 1.8 mm precrack of Fe-23Mn-0.5C TWIP steels with and without hydrogen charging at room temperature and different strain rates. The specimens tested without hydrogen-charging did not show a pronounced strain rate dependence for maximum notched strength and elongation at failure. The hydrogen charging clearly deteriorates the elongation at failure, with the effect being more pronounced at the lower strain rate of 10^{-5} s^{-1}. The strain rate of The decrease in the tensile properties of TWIP steel upon hydrogen charging was also observed previously [6, 7]. Reduction in elongation and maximum notched strength is proximally 42% and 17%, respectively. Fig. 5.2 also shows the net section stress-elongation curves of the specimen with 3.2 mm precrack with and without hydrogen charging at different strain rates. Uncharged specimens did not show any dependency of strain rate. In addition, as explained in the chapter 4, there is no degradation in strength and ductility in the specimen with 3.2 mm precrack in the strain rate of 10^{-4} s^{-1}. In contrast, a degradation of tensile strength and elongation in the presence of hydrogen in the strain rate of 10^{-5} s^{-1} observed. Reduction in elongation and maximum notched strength is proximally 21% and 10%, respectively.

Fig. 5.3 shows the mechanical properties for each cracked specimen at different strain rate of 10^{-4} and 10^{-5} s^{-1}. Fig. 5.3a and 5.3b display the maximum tensile strength and elongation of short and long precracked specimens in two strain rates of 10^{-4} and 10^{-5} s^{-1}, respectively. In case of the uncharged specimens, there is no effect of strain rate reduction. By contrast, for hydrogen-charged specimens both specimens show dependency to the reduction of strain rate.

Fig. 5.4 illustrates the behavior of maximum tensile strength and elongation of cracked specimens at strain rate of 10^{-5} s^{-1} for both hydrogen-charged and uncharged specimens. In addition, this results compared with the results of cracked specimens in strain rate of 10^{-4} s^{-1} as shown in 4.8.

5.3.2 Crack propagation behavior in the hydrogen-charged specimen

Fig. 5.5 displays the surface damage near the fracture surfaces of hydrogen-charged specimens at the slow strain rate of 10^{-5} s^{-1}. Figs. 5.5a and 5.5c are the overview of the half of the width of the samples with precrack length of 1.8 and 3.2 mm, respectively. A considerable number of subcracks formed approximately perpendicular to the tensile axes were observed beside the fracture surfaces as shown Figs. Figs. 5.4b and 5.4d as a magnified images of highlighted area in Figs. 5.5a and 5.5c, respectively.

Fig. 5.6 shows an SEM image and the corresponding RD-IPF map one surface crack in the vicinity of the fracture surface. The RD-IPF map displays the significant number of deformation twins and a number of these deformation twins were observed to impinge on the grain boundaries around the main intergranular crack. Cracking mode is the intergranular crack and also transgranular sub cracks indicted by white arrows in Fig. 5.6b.

5.3.3 Fractographic analysis

Fig. 5.7 shows the fracture surface of uncharged specimens at strain rate of 10^{-5} s^{-1}. Figs. 5.7a and 5.7b show the overview of fracture surface of specimens with 1.8 and 3.2 mm precrack, respectively. The rest of figures are magnified images corresponding to the highlighted locations in the overviews. The fracture surfaces of both uncharged specimens are characterized by a combination of quasi-cleavage feature regarding to the cyclic loading introduced by fatigued-precrack [8] and following ductile features with dimples (Figs. 5.7a_1, a_2, b_1 and b_2).

Fig. 5.8 demonstrates the fracture surfaces of hydrogen-charged specimen with 1.8 mm

precrack in different strain rate of 10^{-4} and 10^{-5} s^{-1}. In the strain rate of 10^{-4} s^{-1}, the fracture surface exhibits a shallow intergranular cracking zone with secondary crack along prior austenite grain boundaries after quasi-cleavage features of precrack. Quasi-cleavage-like features are also observed in the brittle region, as shown in Figs. 5.8a_1, a_2. This brittle region surrounded by dimples and the rest of fracture surface shows ductile feature due to the microvoid coalescence as indicated in Fig. 5.8a_3. In contrast, the charged specimen at strain rate of 10^{-5} s^{-1} shows the brittle feature of intergranular particularly and partially quasi-cleavage features in approximately all part of the fracture surface as shown in the overview and magnified images of 5.8b-b_2.

Fig. 5.9 shows the fracture surfaces of hydrogen-charged specimen with 3.2 mm precrack in different strain rate of 10^{-4} and 10^{-5} s^{-1}. As explained in the 4th chapter, in the strain rate of 10^{-4} s^{-1}, the fracture surface exhibits the combination of quasi-cleavage due to the fatigue and follows by ductile feature which indicate that there is no effect of hydrogen on the specimen with 3.2 mm precrack at the strain rate of 10^{-4} s^{-1}. By contrast, the charged specimen at strain rate of 10^{-5} s^{-1} shows no the brittle feature of intergranular particularly and partially quasi-cleavage features in approximately all parts of the fracture surface as shown in the overview and magnified images of 5.9b-b_2.

Fig. 5.10 shows the magnified portion of the fracture surface of hydrogen charged 1.8 mm precracked specimen conducted at the strain rate of 10^{-5} s^{-1}. This image displays the intergranular cracking consistent of multiple slip traces which indicates by white arrows. In addition, transgranular fracture feature is also exist on the fracture surface as shown in the region highlighted by the red dotted lines.

5.4 Discussion

To explain the effect of strain rate on hydrogen embrittlement of metals, previous investigations [9, 10] have suggested that the rate of hydrogen diffusion to microcracks or voids is the controlling process. As the strain rate is increased there is less time per unit strain for hydrogen to reach microcracks or voids, subsequently, the ductility increases with increasing strain rate. In other words, by reducing the strain rate hydrogen have sufficient time to diffusive to the metal and occur brittle failure. The results of cracked specimens are also in agreement with the previous studies of the strain rate dependency on hydrogen embrittlement of smooth specimens [11, 12]. By reduction the strain rate from 10^{-4} to 10^{-5} s^{-1} the tensile strength and elongation of both specimens with 1.8 and 3.2 mm precracks

decreased markedly (Fig. 5.3). For instance, in this study, there is no hydrogen embrittlement in the specimen with 3.2 precrack length and small reduction in tensile strength and ductility of specimen with 1.8 mm precrack at the strain rate of 10^{-4} s^{-1}, while by reducing the strain rate to 10^{-5} s^{-1}, hydrogen deteriorated the tensile strength and ductility of both specimens significantly at room temperature (Figs. 5.2 and 5.3). The fractographic features have not shown significantly changes in both 1.8 and 3.2 mm precracked specimens at lower strain rate of 10^{-5} s^{-1} compare to the strain rate of 10^{-5} s^{-1} as depicted in Figs. 5.7 and 5.8.

The major site of hydrogen-assisted cracking is the grain boundaries. The crack nucleation sites for the intergranular fracture are the grain boundary triple junction and grain boundaries that are intercepted by progressing deformation twins as shown in Figs. 5.6b and 5.10. Grain boundary triple junction cracking was observed also in the smooth specimen of TWIP steel [13]. The mechanism was explained in terms of plastic strain localization due to the formation of deformation bands around grain boundary triple junctions [14]. This effect was assumed to promote hydrogen localization around grain boundary triple junctions, assisting brittle cracking through a reduction in the cohesive energy at grain boundaries [15].The fracture appearance, can be explained by the influence of hydrogen on dislocation slip. It is knowing that twins are efficient obstacles for dislocation glide [16, 17]. Thus, dislocation pile up at twin or grain boundaries due to enhanced planar slip results in high stresses at such obstacles due to shielding effects [18] leading to twin or grain boundary separation [19, 20] with visible slip traces and thus to a macroscopically reduced ductility. An enhanced mobility of such dislocations should lead to faster twin formation and dislocation pile up at the already formed twins resulting in premature failure. The primary reason why the hydrogen embrittlement was more pronounced at the lower strain rate can be attributed to the fact that sufficiently low strain rates allow the hydrogen to interact with moving dislocations, which in turn promotes hydrogen embrittlement [21, 22]. Hydrogen is carried to the grain and twin boundary crack sites via dislocations and the effectiveness of dislocations is enhanced in concentrating hydrogen at those points on the grain and twin boundaries where the stress is also at maximum concentration [13, 23].Unlike to the previous chapter, crack length does not play the vital role in hydrogen-assisted cracking at the strain rate of 10^{-5} s^{-1}. Based on the similarities in fracture appearance, it can be assumed that hydrogen effects on dislocation slip play a predominant role in hydrogen assisted cracking due to the reduction in strain rate.

Accordingly, the cracked tensile strength is dependent on the strain rate because the

hydrogen accumulation was controlled by the available time for hydrogen diffusion to the crack initiation site and the time was evidently dependent on the strain rate.

Finally, the strain rate dependence of the tensile strength of the present steel indicated the important role of the hydrogen accumulation in the fracture process specially in the cracked specimen even in the slow strain rate tensile test.

5.5 Conclusions

Decreasing the strain rate provides sufficient time for hydrogen diffusion. Consequently, increasing the hydrogen concentration decreases the tensile strength and elongation, as well as, change the fracture surface from ductile to brittle of intergranular combine the transgranular feature of cracked specimens.

5.6 References

[1] Depover T, Elmahdy A, Vercruysse F, Verleysen P, Verbeken K. Effect of strain rate on the hydrogen embrittlement of a DP steel. EPJ Web of Conferences: EDP Sciences; 2018. p. 03015.

[2] Momotani Y, Shibata A, Terada D, Tsuji N. Effect of strain rate on hydrogen embrittlement in low-carbon martensitic steel. International Journal of Hydrogen Energy. 2017;42:3371-9.

[3] Koyama M, Akiyama E, Tsuzaki K. Hydrogen-induced delayed fracture of a Fe–22Mn–0.6 C steel pre-strained at different strain rates. Scripta Materialia. 2012;66:947-50.

[4] Toribio J, Elices M. The role of local strain rate in the hydrogen embrittlement of round-notched samples. Corrosion Science. 1992;33:1387-95.

[5] Bal B, Koyama M, Gerstein G, Maier H, Tsuzaki K. Effect of strain rate on hydrogen embrittlement susceptibility of twinning-induced plasticity steel pre-charged with high-pressure hydrogen gas. international journal of hydrogen energy. 2016;41:15362-72.

[6] Koyama M, Akiyama E, Tsuzaki K. Hydrogen embrittlement in a Fe–Mn–C ternary twinning-induced plasticity steel. Corrosion Science. 2012;54:1-4.

[7] Koyama M, Akiyama E, Tsuzaki K. Effect of hydrogen content on the embrittlement in a Fe–Mn–C twinning-induced plasticity steel. Corrosion Science. 2012;59:277-81.

[8] Habib K, Koyama M, Noguchi H. Impact of Mn–C couples on fatigue crack growth in austenitic steels: Is the attractive atomic interaction negative or positive? International Journal of Fatigue. 2017;99:1-12.

[9] Barrera O, Bombac D, Chen Y, Daff TD, Galindo-Nava E, Gong P, et al. Understanding and mitigating hydrogen embrittlement of steels: a review of experimental, modelling and design progress from atomistic to continuum. Journal of Materials Science. 2018;53:6251-90.

[10] Bolzoni F, Fallahmohammadi E, Re G, Fumagalli G, Ormellese M, Lazzari L. Electrochemical investigation of hydrogen diffusion in pipeline steels. Corrosion/2013, paper. 2013.

[11] Bal B, Koyama M, Gerstein G, Maier HJ, Tsuzaki K. Effect of strain rate on hydrogen embrittlement susceptibility of twinning-induced plasticity steel pre-charged with high-pressure hydrogen gas. International Journal of Hydrogen Energy. 2016;41:15362-72.

[12] Taheri M, Albrecht J, Bernstein I, Thompson A. Strain-rate effects on hydrogen embrittlement of 7075 aluminum. Scripta Metallurgica. 1979;13:871-5.

[13] Koyama M, Akiyama E, Tsuzaki K, Raabe D. Hydrogen-assisted failure in a twinning-induced plasticity steel studied under in situ hydrogen charging by electron channeling contrast imaging. Acta Materialia. 2013;61:4607-18.

[14] Wilcox B, Smith G. Intercrystalline fracture in hydrogen-charged nickel. Acta Metallurgica. 1965;13:331-43.

[15] Koyama M, Springer H, Merzlikin SV, Tsuzaki K, Akiyama E, Raabe D. Hydrogen embrittlement associated with strain localization in a precipitation-hardened Fe–Mn–Al–C light weight austenitic steel. international journal of hydrogen energy. 2014;39:4634-46.

[16] Bouaziz O, Allain S, Scott C. Effect of grain and twin boundaries on the hardening mechanisms of twinning-induced plasticity steels. Scripta Materialia. 2008;58:484-7.

[17] Li N, Wang J, Misra A, Zhang X, Huang J, Hirth J. Twinning dislocation multiplication at a coherent twin boundary. Acta Materialia. 2011;59:5989-96.

[18] Chateau J, Delafosse D, Magnin T. Numerical simulations of hydrogen–dislocation interactions in fcc stainless steels.: part II: hydrogen effects on crack tip plasticity at a stress corrosion crack. Acta Materialia. 2002;50:1523-38.

[19] San Marchi C, Nibur K, Balch D, Somerday B, Tang X, Schiroky G, et al. Hydrogen-assisted fracture of austenitic stainless steels. Effects of Hydrogen on Materials, Proceedings of the 2008 International Hydrogen Conference (Moran WY, 2008), ASM International, Materials Park OH2009. p. 88-96.

[20] San Marchi C, Yang N, Headley T, Michael J. Hydrogen-assisted fracture of low nickel content 304 and 316L austenitic stainless steels. 18th European Conference on Fracture (ECF18), Dresden, Germany2010.

[21] Michler T, Naumann J. Hydrogen environment embrittlement of austenitic stainless steels at low temperatures. International Journal of Hydrogen Energy. 2008;33:2111-22.

[22] Birnbaum HK. Hydrogen effects on deformation — Relation between dislocation behavior and the macroscopic stress-strain behavior. Scripta Metallurgica et Materialia. 1994;31:149-53.

[23] Koyama M, Akiyama E, Sawaguchi T, Raabe D, Tsuzaki K. Hydrogen-induced cracking at grain and twin boundaries in an Fe–Mn–C austenitic steel. Scripta Materialia. 2012;66:459-62.

5.7 Figures

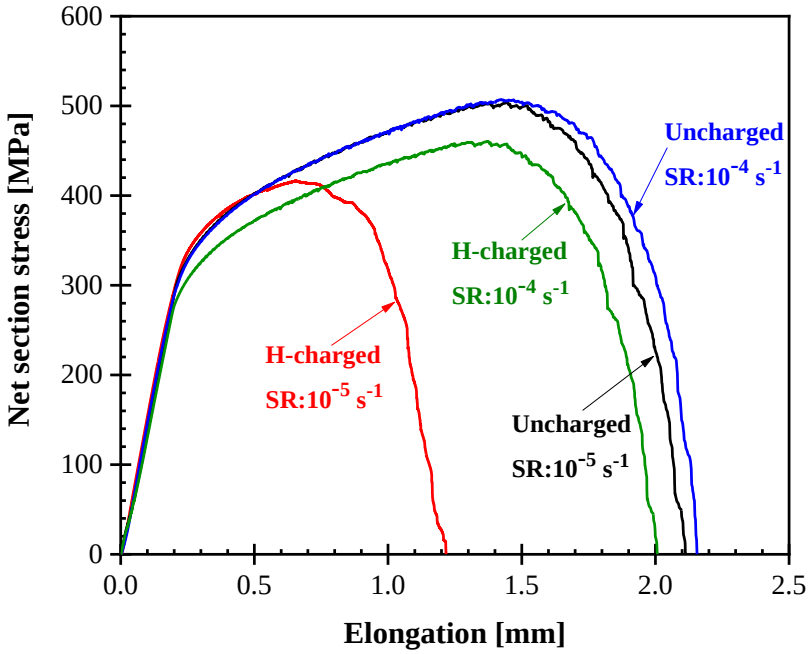

Fig. 5.1. The net section stress-elongation curves of 1.8 mm precrack specimen at strain rates of 10^{-4} and 10^{-5} s^{-1}.

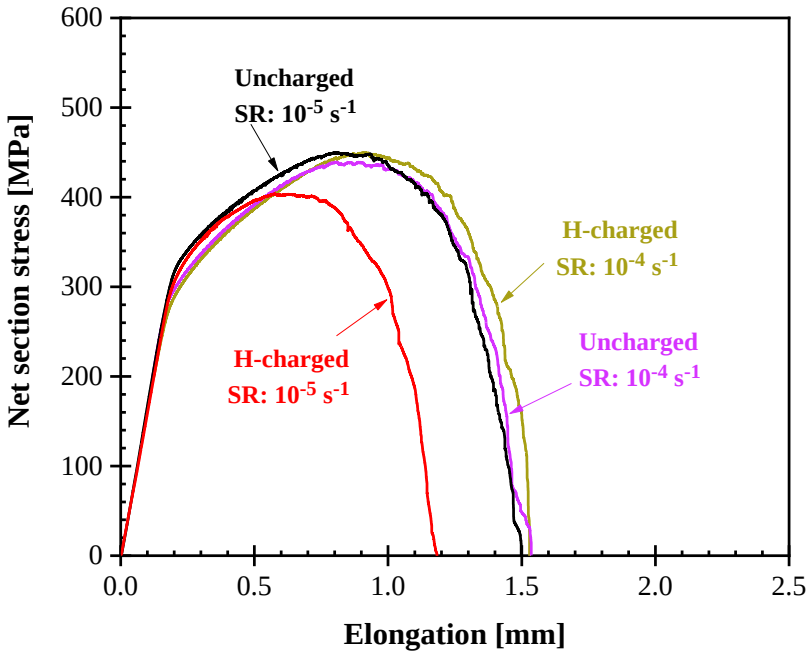

Fig. 5.2. The net section stress-elongation curves of 3.2 mm precrack specimen at strain rates of 10^{-4} and 10^{-5} s^{-1}.

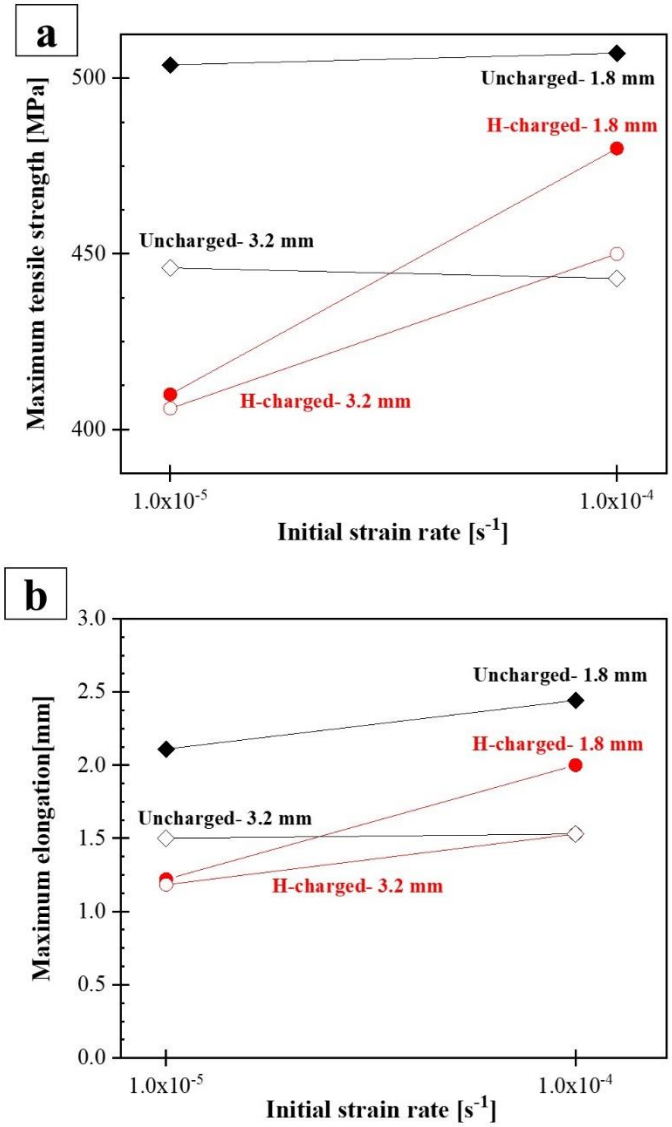

Fig. 5.3. Showing the maximum (a) tensile strength and (b) elongation in 1.8 and 3.2 mm precracks specimens at strain rate of 10^{-4} and 10^{-5} s^{-1}.

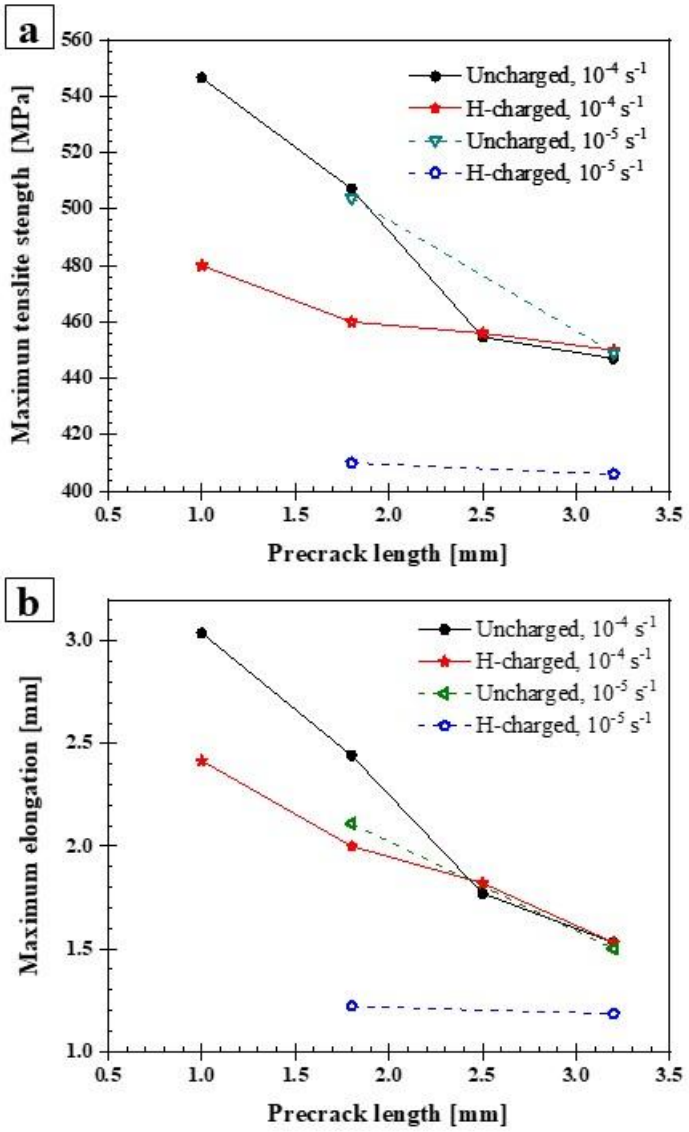

Fig. 5.4. Showing the difference between maximum (a) tensile strength and (b) elongation in the cracked specimens at the different strain rates of 10^{-5} and 10^{-4} s^{-1}.

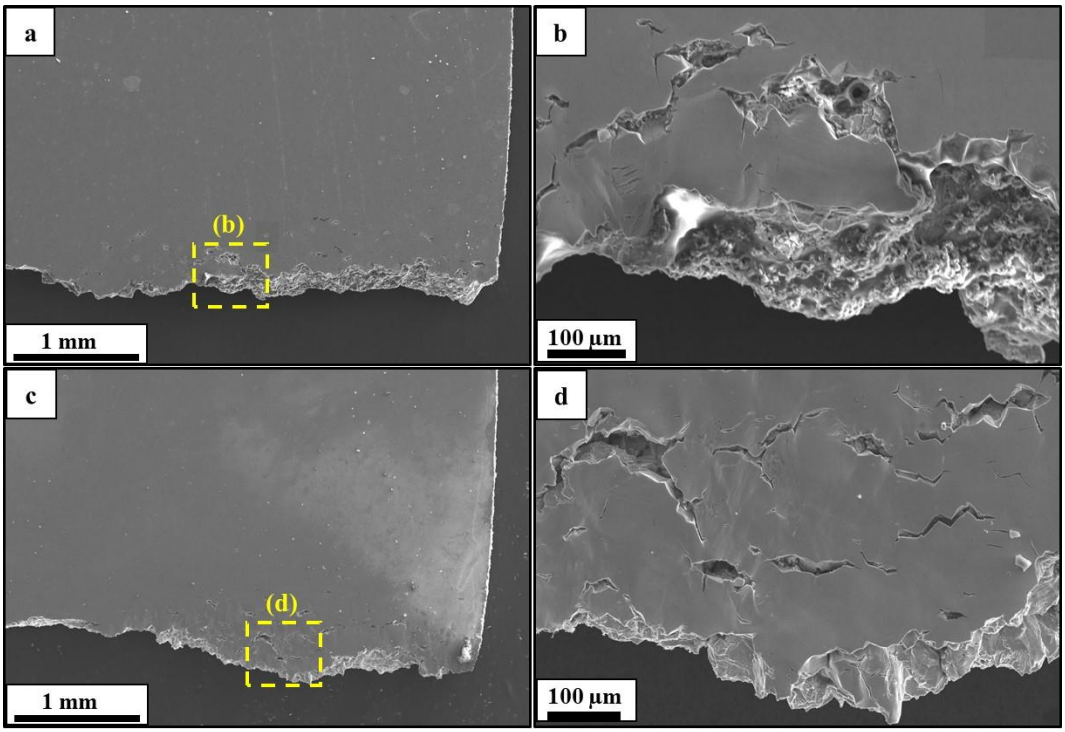

Fig. 5.5. Showing the surface cracks in the vicinity of the fracture surface of (a) 1.8 mm precracked specimen and (b) magnified image of highlighted area in (a) and (c) 3.2 mm precracked specimen and (d) magnified image of highlighted area in (c) at the strain rate of 10 -5 s-1.

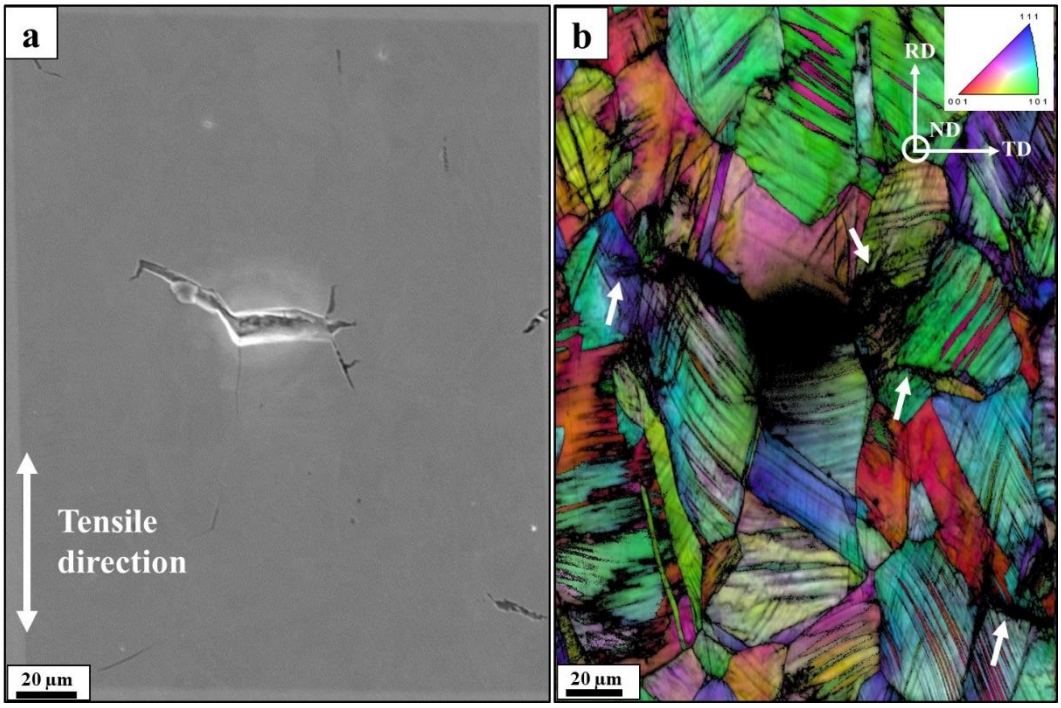

Fig. 5.6. (a) SEM image and (b) corresponding RD-IPF map of surface crack in the vicinity of the fracture surface of 1.8 mm precracked specimen at the strain rate of 10-5 s-1. The RD-IPF map is superimposed with the IQ contrast.

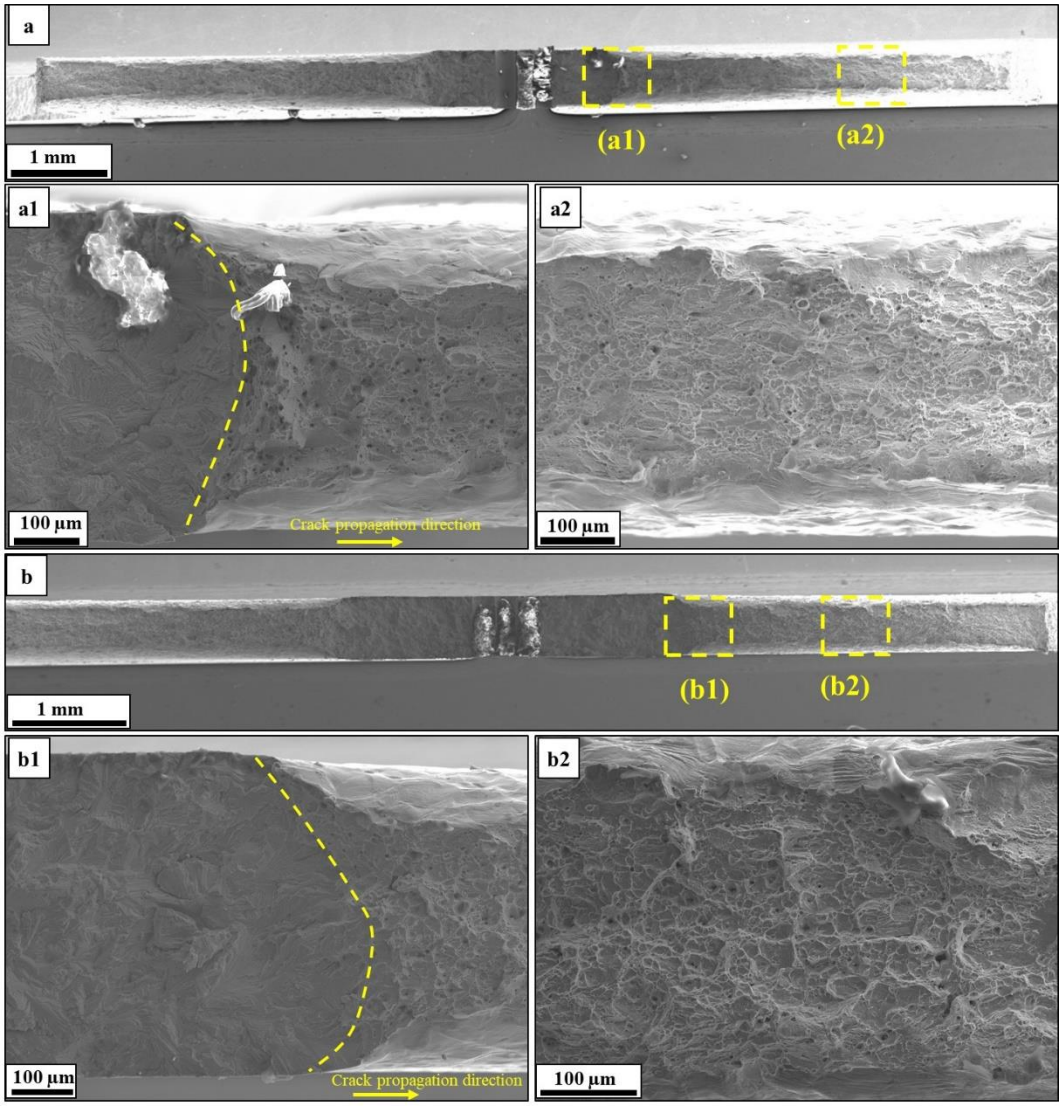

Fig. 5.7. Fracture surface of uncharged specimens of 1.8 and 3.2 mm precrack specimens at strain rate of 10^{-5} s^{-1}. (a)-(a2) 1.8 mm precracked specimen. (b)-(b2) 3.2 mm precracked specimen. Yellow dashed line indicate the fatigued-precrack tip.

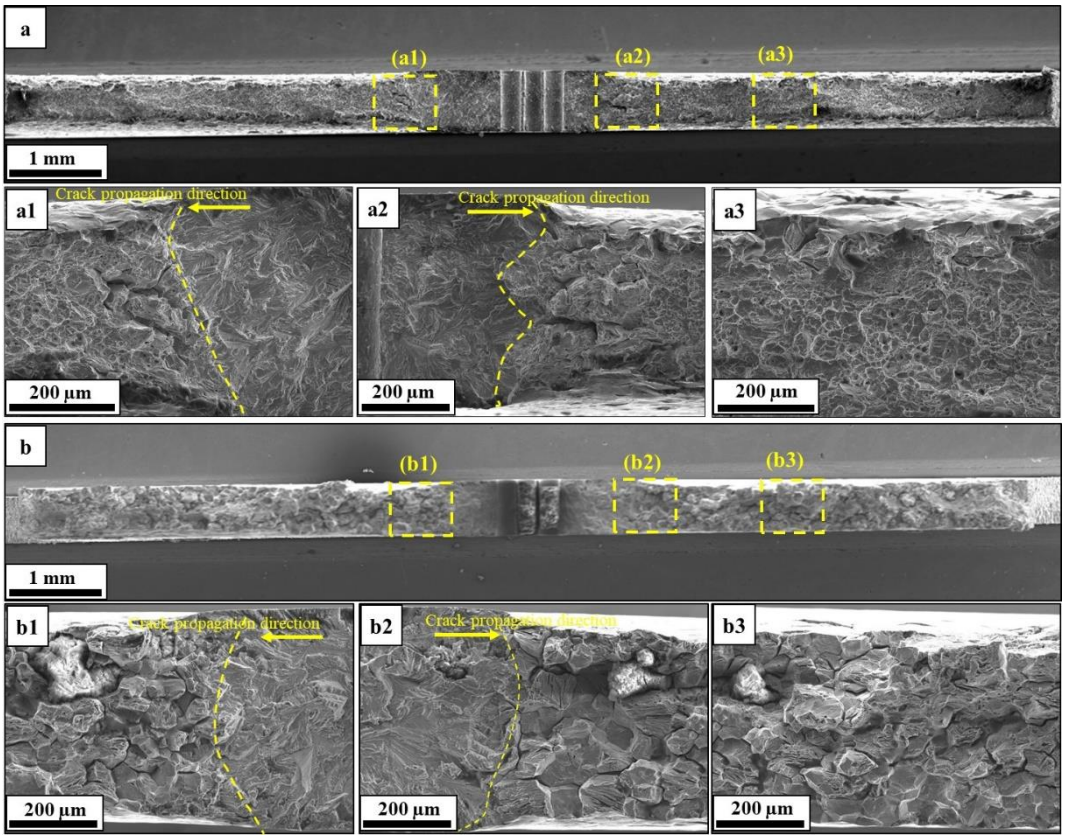

Fig. 5.8. Fracture surface of hydrogen-charged specimens of 1.8 mm precrack specimens at strain rate of (a)-(a3) 10^{-4} s^{-1}, and (b)-(b3) 10^{-5} s^{-1}. Yellow dashed line indicate the fatigued-precrack tip.

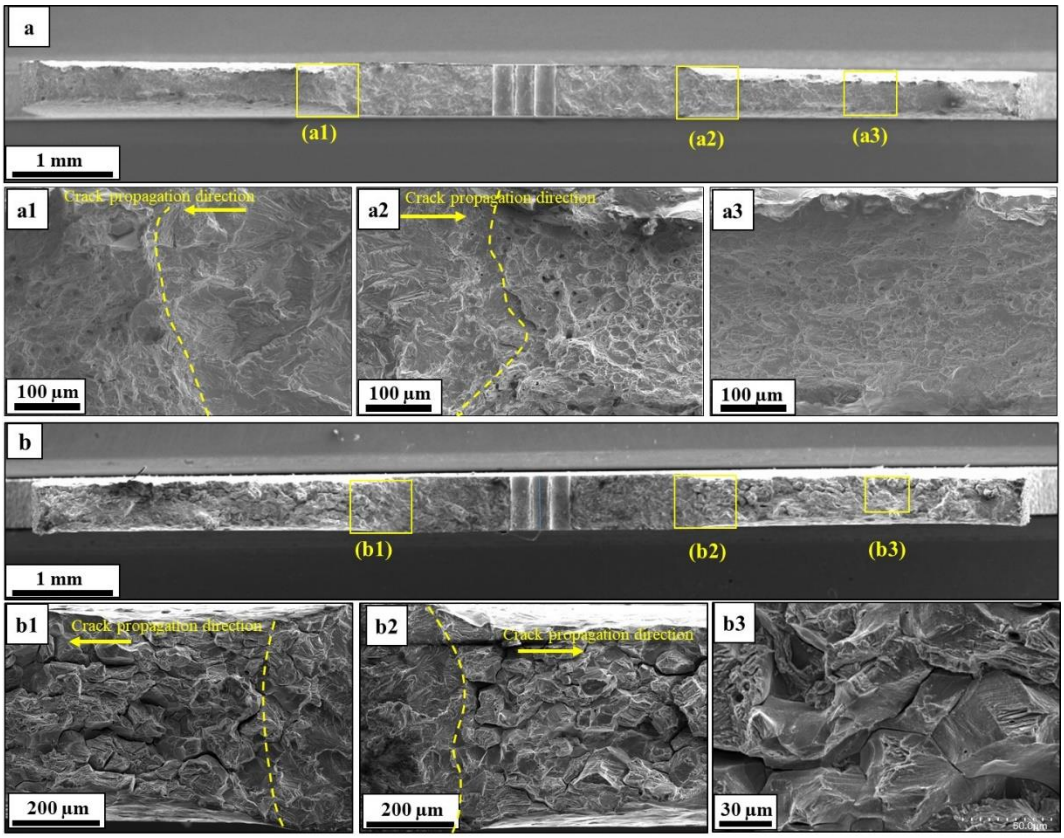

Fig. 5.9. Fracture surface of hydrogen-charged specimens of 3.2 mm precrack specimens at strain rate of (a)-(a3) 10^{-4} s^{-1}, and (b)-(b3) 10^{-5} s^{-1}. Yellow dashed line indicate the fatigued-precrack tip.

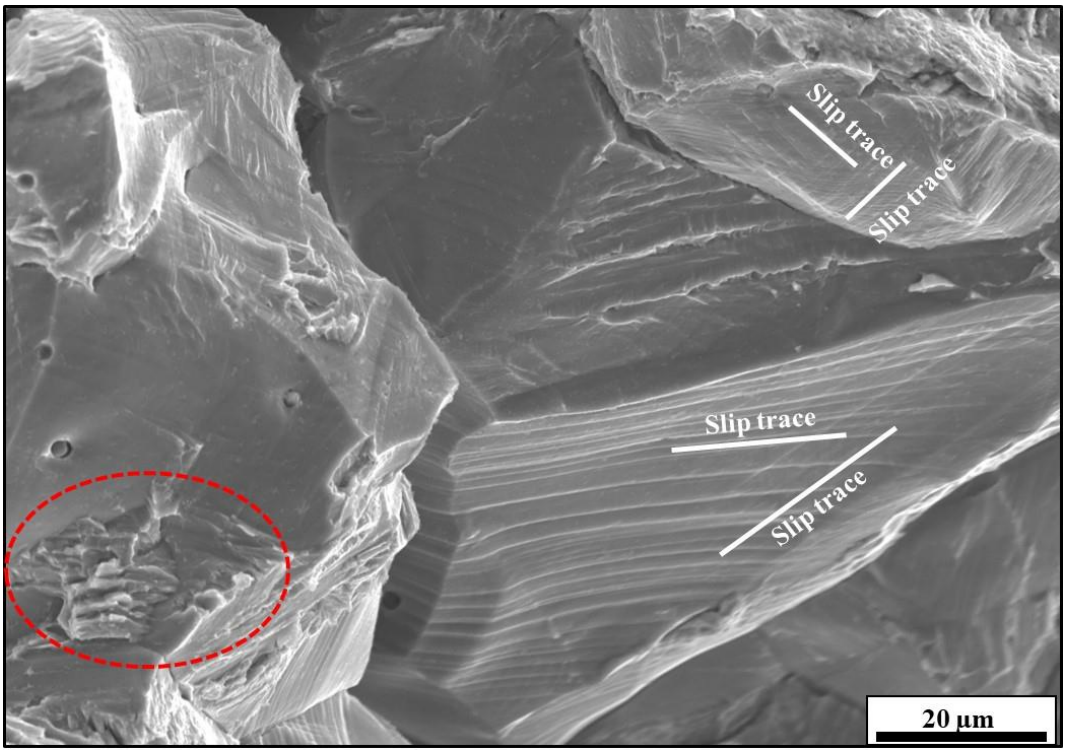

Fig. 5.10. The high magnified portion of fracture surface of 1.8 mm precracked specimen. Multiplane slip traces exist on the intergranular surface indicated by white lines. Red dotted circle shows the transgranular fracture surface.

CHAPTER 6: General Conclusions and Outlook

6.1 Conclusions

As a new alloy, bimodal-grained TWIP steel presents extraordinary mechanical properties even in the presence of the hydrogen. This attributed to the aspect of superior combination of strength and ductility due to the simultaneously strengthening ability of fine grains and deformability of coarse grains. The occurrence of embrittlement in the bimodal grains can be explained by two main factors. Firstly, crack initiation/propagation along the grain and twin boundaries and second, delamination crack growth. The micro-stress concentration and plastic strain localization at the twin–twin intersection/interception caused hydrogen assisted crack initiation and growth. Furthermore, deformation twinning played an important role in the intergranular and transgranular cracking. Intergranular cracks tended to grow along the grain boundaries between the fine and coarse grains, while, the transgranular cracks tended to propagate into the coarse grains. The delamination observed on the fracture surface of the hydrogen-charged specimen was caused by void coalescence that nucleated along the tensile axes. The coalesced micro-voids elongated at the grain boundaries between the fine and coarse grains due to the elastic misfit and in the grain interior of the coarse grains because of the associated localization of stresses and strains. The results reveal that the bimodal grain size distribution of TWIP steel plays a major role on hydrogen-assisted cracking and the evolution of delamination-related damage.

Crack propagation in the high strength high ductility steel such as TWIP steel has substantial importance. Such a large ductility in this material can change cracking behavior because of the significant plasticity at the crack tip. Therefore, studying on the hydrogen-assisted crack propagation mechanism is significantly important. Hydrogen-assisted crack propagation in the pre-deformed TWIP steel occurred via a quasi-cleavage feature, and the crack growth rate increased with increasing initial defect sizes, as a stress concentration source, when the crack length was small. The stress accommodation at the crack tip caused large plastic straining, resulting in work hardening and increasing twin density. These plasticity-related factors cause a crack formation in front of the main crack tip. The crack initiation and subsequent coalescence are the crack growth process, accordingly, the hydrogen-assisted crack growth mechanism is discontinuous, which involves step-like

ridges and local formation of dimples on the fracture surface. A significant pre-plastic deformation accelerates a formation of the plasticity-induced precursor of the crack, which is considered to assist transgranular crack propagation. Finally, the factor affecting the hydrogen-assisted cracking are not specific features of the bimodal microstructure.

In the term of hydrogen-assisted cracking, cracked specimens of TWIP steel showed considerable behavior at the slow strain rate of 10^{-4} s^{-1}. Specimens with longer precrack length show higher resistance to hydrogen embrittlement than specimens with short precrack lengths. In other words, specimens with precrack length less than 2 mm are susceptible to hydrogen embrittlement, while hydrogen did not have any effect on the mechanical properties of specimens with precrack longer than 2 mm. Results confirmed the vital role of local strain rate at the crack tip at slow strain rate in hydrogen embrittlement.

Decreasing the strain rate to 10^{-5} s^{-1} provides sufficient time for hydrogen diffusion for the cracked specimens, particularly for the longer precrakced one which did not show hydrogen embrittlement at 10^{-4} s^{-1}. Consequently, increasing the hydrogen content decreased the tensile strength and elongation, as well as changed the fracture surface from ductile to fully brittle of combination of intergranular and transgranular. Results suggested that hydrogen embrittlement of cracked specimen in TWIP steel sensitive to the strain rate specially at the very slow strain rate.

6.2 Outlook

According to the present work, it is worth further research on factors can effect on the crack propagation, particularly quantify the local strain rate at the crack tip by using FEM analysis in the dynamic condition. Finding the relationship between constraint and the local strain rate in the cracked or notched specimens can help to understand deeply on the effect of the interaction between hydrogen and dislocation movement at the crack or notch tip. In addition, extrinsic factors such as plastic wake effect associates to the crack propagation. It is highly recommended to work on the crack propagation from the mechanical view point as well as metallurgical observations.

Acknowledgement

First and foremost, I would like to express my deepest and sincerest thanks to my thesis supervisor Professor Hiroshi Noguchi, who gave me the opportunity to join and work in his prestigious Laboratory, Solid Mechanics Lab, at Kyushu university, Japan. He constantly gave me courage, taught me how to research and initiated very interesting and deep discussions to keep me on the right track. He, undoubtedly, opened new window of research vision in my studying life. By counting on his supports, I left behind the difficulties in Japan easily.

I would like to thank the thesis committee members: Professor Kaneaki Tsuzaki and Professor Hiroyuki Toda, for their valuable time, encouragement and insightful comments.

I am very much thankful to the Associate Professor Motomichi Koyama for his valuable advices and supports during my PhD. Additionally, I would like to extent my thanks to Associate Professor Shigeru Hamada for his support in our lab and Mrs. Masako Kadota, the secretary of lab. I also thank my friends in our lab, who I always was remotely consulting with.

Last but not least, I owe my greatest debt of gratitude and thanks to my parents, brother and sister. This dissertation would not have been possible without their warm love, continued patience, and endless support.

ABBAS MOHAMMADI

アバス　モハマディ

Kyushu University, Japan

九州大学、日本

“Land of the Rising Sun”

July 2019